Investigations in Matterwave Interferometry for Inertial Sensing

Matthew JOHNSON

Experimental Quantum Optics and Photonics Group
Department of Physics and SUPA

University of Strathclyde

A thesis presented in the fulfilment of the requirements for the degree of

Doctor of Philosophy

2021

Declaration of Authorship

This thesis is the result of the author's original research. It has been composed by the author and has not been previously submitted for examination which has led to the award of a degree.

Signed:

Date:

Abstract

Matthew JOHNSON

Investigations in Matterwave Interferometry for Inertial Sensing

The sensing of rotation is a keystone in navigation without external aid. Without relying on satellite navigation, for instance, it is possible to navigate by knowing one's velocity and rotation rate and then integrating over time. Such "dead reckoning" inertial navigation methods are hampered by errors in the sensing of these quantities, which are amplified by the integration process, leading to wildly inaccurate measurements of position in a matter of minutes even in some of the best commercial units. There is interest in pursuing rotation sensing from the position of quantum technology - where atomic Sagnac interferometers promise unprecedented sensitivities to rotation.

In this thesis we detail a variety of investigations supporting future implementation of atomic interferometry as a quantum technology. We detail the construction of a new vacuum chamber for generating Bose-Einstein condensates (BECs) of rubidium-87, with a primary focus on a 2D+ magneto optical trap. This 2D+ geometry allows for a high flux of atoms, important in reducing dead time in interferometers. We then present a Sagnac interferometer configuration with a BEC in freefall under gravity. Calibration of the system under freefall is discussed, in particular the calibration of the beam power as a function of the drop time, and the asymmetry in the interferometer output with respect to the angle to gravity. We finally present a study in high numerical aperture Fresnel zone plates (high NA FZPs) for generating optical ring traps. The high NA requirement allows for diffraction-limited roughness in the trapping potential, as well as the possibility to map local intensity changes at the FZP to the focal plane. We also present this method as a candidate for generating dark ring traps using blue-detuned light.

Acknowledgements

I could not have come this far in life without the help of a great many friends, colleagues and family members. To all those who have supported me over the years, I thank you all.

To my supervisor Aidan, this thesis could not have been done without you. You were an inspiration and a guide for me through this project. Your ideas and enthusiasm would always serve to aid me when I had trouble. Your support, especially in the last year with the pandemic, was lifegiving. I cannot thank you enough.

To Griff, who got me into this mess to begin with! My heartfelt thanks. A guru in the lab, I am sure I annoyed you on many occasions by coming past your office with the latest thing I had broken. Most of what I know, both technical and theoretical, you have been the one to teach me. I appreciate the depth and breadth of your knowledge. And your mighty fine bass-playing as well!

To Erling Riis, thank you for giving me the opportunity to study alongside you all at Strathclyde. I have learned so much from you all. Your insight was always valuable, and I appreciate the time you made for us, even as head of department.

To my colleagues in EQOP – what a rowdy bunch! To Carolyn, Michael, Rachel, Katie, Illian, Oliver; my heartfelt thanks for your friendship and many a great lunchtime conversation. To Andres, Costa and Andrea: the Paesano crew. Thank you for all our lunchtime adventures, conversation and general nerding out. To my officemates, Craig and Rudy, your camaraderie got me through the lows and brightened up the highs – I will never forget the laughs and the conversations we had. Billy, you and the lunch crew made me feel like I had a place at Strathclyde, so thank you for reaching out that first week. Here's all to more inevitable egg in the common room!

To Vicki, my co-conspirator and FZP shawl knit-wizard! Thank you. Your mentorship invaluable, and your friendliness and approachability helped me settle into the role of an experimentalist. You have the patience of a saint, especially to put up with my constant bombard of questions. Thank you for all that you do.

Further afield, to all the staff at Strathclyde physics I had the pleasure of working with over the years. Bob and Ewan in the workshop, Shirley, Melanie, and Kirsten in the office, Ged and Mark in electronics, Timothy and Jamie in IT, John and Ken – thank you all for keeping the ship running for all of us at Strathclyde physics.

To my brother James, thank you for being such an excellent guide to Glasgow. It was so nice to have a familiar face when starting, especially to come home to. To my best friends, Ruaridh, Ben and Sam, thank you for being on the end of a phone whenever I needed it. Here's to many more late night jackbox sessions!

To my Dad and Anne, thank you for believing in me. I have never been the most confident in myself, but you have helped keep my head above water over the years, being there for me when I needed advice or simply a familiar voice to speak with. Dad, I owe everything to you, thank you for being my dad.

To Clare. My muse, my rock, my candle in the dark. Your love and support means everything in the world to me. Simply, I could not have done this without you. Your belief in me helped me get through some of the worst of these past years, and I'm glad I now get the share the next many many happy years alongside you.

To Mum, I hope I've made you proud. Thank you for making me who I am.

Contents

Chapter 1

Introduction: Interferometry

In this introduction we will discuss the underlying principle of the atom interferometer, and why it is a candidate for investment as a quantum technology. First we will describe the principles for useful interferometry and in particular how it can be orientated for rotation sensing via the Sagnac effect. The inherit advantages of using an atomic system versus current optical devices will be discussed, and from this we will outline why interferometry with Bose-Einstein condensates should be pursued. Lastly we motivate the work done in this thesis on interferometry for rotation sensing: a preliminary study in a freefall interferometer, and further work on guided interferometry.

1.1 Rotation sensing as a Quantum Technology

It is oft said that we stand amidst the "second quantum revolution". Einstein, Bohr, Schrödinger and their contemporaries described a quantum world at the turn of the 20th century, and at the turn of the 21st we now see technology that relies on such principles being used almost everyday - from the MRI scanner to the atomic clock [1]. Another part of this second wave of interest in quantum mechanics is in the technology surrounding quantum superposition and entanglement, enabling the sectors in quantum information processing, communication and measurement [2].

The term *quantum technology* describes a multitude of techniques and systems developed with some utilisation of the quantum world, promising improved performance over their classical counterparts [3]. This includes atomic clocks [4] and other metrology devices [5, 6] to cryptographic key distribution [2] and even the dating of arctic ice [7].

The branch of quantum metrology concerns the science of measurement utilising methods of a quantum nature. Primarily in this case it is the act of quantum superposition that is used, where an object may assume multiple distinct states simultaneously. The nature of this superposition and the method of preparation can lead to the measurement of many useful quantities. The superposition of atomic energy states leads to precise measurements in frequency, which form the basis for atomic clocks, and a superposition in space constituting an atom interferometer permits the ultra-precise measurement of acceleration. These technologies are not all equal in their commercial viability however; whilst atomic frequency standards are used worldwide as benchmarks in timekeeping, atomic inteferometers are not as technologically ready, despite enjoying a 30 year history in research [2]. Atom interferometers are powerful measurement devices however, with some distinct advantages over classical interferometers using light or mechanical vibration. As such there is considerable effort in taking these experiments out of the lab and deploying them into real-world applications [8].

Rotation sensing is one such application where quantum technology could fill a gap. Knowing how far one has rotated is a key element in inertial navigation, or “dead reckoning”, where one must navigate without external aid, relying instead on recalling by how much one has travelled and in which direction. In use today, inertial measurement units (IMUs) are found in the aviation, defence and space industries. One cannot directly measure position and angle using an IMU - the measured acceleration and rotation rate must be integrated in order to ascribe position and angle. Therefore any errors in measurement are compounded by the integration - an error of acceleration on order $1 \times 10^{-5}\,\mathrm{m\,s^{-2}}$ results in a drift of position by 100 m in one hour. Atomic sensors offer an avenue to produce much more accurate sensors.

We present two investigations in this vein to aid in generating a quantum rotation sensor. First is an interferometer configuration based on a Bose-Einstein condensate (BEC) falling freely under gravity, and secondly a computational study of Fresnel Zone plates for generating ring traps in the *near-field*.

1.2 Interferometry and the Sagnac Interferometer

By an interferometer, we are describing a device that measures some quantity via an interference effect. Interference is a property of superposing waves, as seen in water, light, electrons, atoms, and in molecules. Each source of waves brings about its own particular nuances to interferometric sensing.

From as early as Fresnel and Young the interference of light waves has been used in fundamental discoveries in physics [9, 10]. The work of de Broglie and early quantum theorists then showed that matter can also be described in wave-like terms, leading to the theorems and work surrounding wave-particle duality [11]. The crux of this is the matter-wave or de Broglie wavelength,

$$\lambda_{\text{db}} = \frac{h}{p}, \tag{1.1}$$

the relationship between a particle's wavelength, λ_{db} and its momentum, p, by Planck's constant, h. The interference of matter waves has been shown for single electrons [12] with Young's-slits experiment demonstrating the quantum nature of matter. Interference has also been shown for neutrons [13], atoms [14], molecules [15] and recently for a large polypeptide [16].

To observe an interference useful for measuring external sources of phase, the wave must be *split*, allowed to travel in order to probe its surroundings, and then brought back together again and *recombined*. Geometrically, bringing the wave back together again requires some form of *reflection*. To use the analogy in optics, we require therefore atomic equivalents of a *beamsplitter* and some kind of *mirror*. One such interferometer configuration is the Mach-Zehnder interferometer, as shown in figure 1.1. An optical beam is split between two paths by a beam-splitting cube. These are then reflected before being brought together and recombined.

With a source of waves and a method to split and recombine them we have an interferometer. Interferometry is a powerful technique used to measure many different things in fine detail. The LIGO consortium famously use an optical interferometer with 4 km long arms to detect gravitational waves, relative distortions of space on the order of 1 part in 1×10^{21} [17], for which the 2017 Nobel prize in physics was won [18]. We are interested in the measurement of rotations, which generates a phase in an interferometer via the Sagnac effect.

1.2.1 Sagnac effect

Georges Sagnac published his account of the effect that rotation has on the output of a ring-shaped interferometer as early as 1913 [19, 20] where he was interested in theories of the ether [21]. Predictions that the earth's rotation would bias such a device require extremely large area interferometers, which

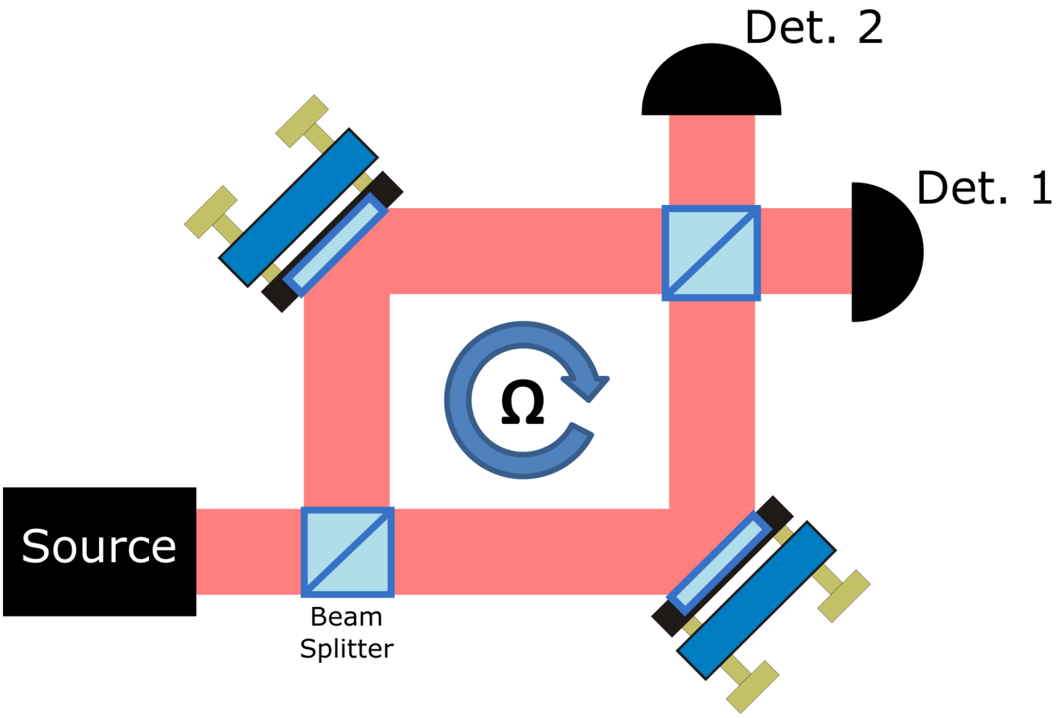

FIGURE 1.1: An optical Mach-Zehnder interferometer which is able to pick up a phase between the two detectors as the apparatus rotates, known as the Sagnac effect. As the apparatus rotates, the clockwise and anti-clockwise paths become unequal in length due to the finite speed of light. The difference in lengths is proportional to the rotation rate.

in the early 20th century were difficult to design. It took the invention of the laser to make such devices stable and large enough to make measurements at such a scale [19, 22].

Light is split and sent in counter-propagating directions around a loop, akin to that in figure 1.1. If one considers the finite speed of light, c, then it is simple to see why a phase difference is generated in a rotating loop. Light travelling around a loop in the direction of the rotation will have an effectively longer path to travel than that of light travelling in the counter-rotating direction. This difference in time to detector means that there will be a difference in phase, ϕ, between the two.

This argument can be extended to massive particles as well. Consider a loop of length L, which for simplicity we shall consider a ring, $L = 2\pi R$, where R is the radius. A particle with velocity, v, will travel a complete revolution distance $L = vt$ in a time, t. If the ring rotates with a rate Ω then time taken to traverse the loop can be expressed as

$$t_{\pm} = \frac{2\pi R \pm R\Omega t_{\pm}}{v}, \tag{1.2}$$

where $t_{\pm}$ denotes the traversal time for the co- and counter- rotating terms respectively. The time difference can be reduced to the expression,

$$\Delta t = t_{-} - t_{+} = \frac{4\pi R^2 \Omega}{v^2 - (\Omega R)^2} \approx \frac{4\pi R^2 \Omega}{v^2}, \tag{1.3}$$

where we have used the approximation that $\Omega r \ll v$. The difference in phase, ϕ, is given by $\Delta\phi = \frac{v}{\lambda_0}\Delta t$, where λ_0 is the particle wavelength, hence,

$$\Delta\phi = \frac{4\pi R^2 \Omega}{\lambda_0 v}. \tag{1.4}$$

This expression is specific to ring-type geometries, but the Sagnac effect applies to any *looped* interferometer by the relationship

$$\Delta\phi = \frac{2E}{\hbar c}\vec{A} \cdot \vec{\Omega}, \tag{1.5}$$

where the energy of the particle, E, is included and the phase is the projection of the axis of rotation onto the loop area. Indeed this generalisation from $\hbar\omega$ to particle energy applies to wave-like particles too. The energy of *massive* particles varies with $E = mc^2$, where m denotes the particle mass and c the speed of light. Heavy atoms, compared to lighter nucleons or electrons, are therefore advantageous to use, due to this scaling. The Sagnac effect with massive particles was first shown for electron pairs in 1965 [23], neutrons in 1979 [24] and for atoms in 1991 by Riehle et al [25].

1.2.2 Optical rotation sensing

Modern optical sensors for rotation include the Laser-Ring Gyroscope and the Fibre-Ring Gyroscopes. The laser-ring gyro is an active optical device, where the laser source itself is modulated according to the rotation, and the fibre-ring gyroscope is a passive device, using laser light to generate an interferometric geometry. Reviews of these sensors can be found at the following references [26–29].

The laser-ring gyro makes use of a ring-shaped laser cavity, of which the rotation rate affects a change in the cavity length, resulting in a frequency difference in the clockwise and anticlockwise rotating modes [26]. This difference is measurable as a beat note, an effective heterodyne measurement between the mode *frequencies*. As we now measure the path length difference via this beat note, the output is scaled by ω/L compared to measuring path length alone. Such devices have a small footprint and are routinely used in the aviation industry as well as in scientific endeavours [30]. They however suffer from the "lock-in" effect where the gyroscope can become insensitive to small rotations (on the order degree per hour, °/h) due to backscatter in the cavity [29].

A Fibre-ring optical gyroscope (FOG) is a Mach-Zehnder interferometer constructed with a long loop of optical fibre, where two laser modes from a single source counter-propagate through the fibre. This bundle of fibre can have an extremely long path length when wound appropriately, bringing the effective interferometer area up to several km^2, whilst remaining relatively compact.

Both devices run into issues with temperature fluctuations, from the drift of the laser frequency to the change in the length of the fibre. It is this bias drift that limits some of the best optical gyroscopes commercially available. This is to say that over time a gyroscope at rest will drift from its original zero-point. This is especially harmful for navigation using inertial measurement units (IMUs) that rely on a suite of gyroscopes and accelerometers in order to accurately relay space and angle coordinates [27]. Navigation is achieved by integrating the sensor readings, hence any errors and uncertainty in the measurement are amplified. It is therefore of interest to generate sensors that are resilient to these kinds of long-term drifts. Atomic sensors are one such solution.

1.2.3 Atomic rotation sensing

To generate an atom interferometer we must generate an atomic analogue to optical beamsplitters, since a key aspect of any interferometery is the splitting of waves. Atom-optic beamsplitters are made from the coherent manipulation of either external (i.e. momentum) [31, 32] or internal (i.e. electronic) [33] states of an atom. We go into more detail about the splitting of the atomic ensemble in chapter 3. The nature of the atomic ensemble being split must also be considered [5]. Whilst thermal atomic ensembles (such as atoms in a mageto-optical trap) are relatively quick to generate, their thermal velocity distribution makes it difficult to address the entire population with a single process - there are still significant number of atoms that are not addressed and must be “blown away” with a resonant pulse. BECs offer an advantage in that the whole ensemble can be addressed, and coherent beamsplitting can be made very efficient [34, 35].

The motivation for atomic rotation sensing is found by considering the energy of the particle. In equation 1.5 if we compare the phase shifts for atomic and optical sensors ($\Delta\phi_{\text{atom}}$ and $\Delta\phi_{\omega}$ respectively) given the same interferometer area and rotation rate we see,

$$\frac{\Delta\phi_{\text{atom}}}{\Delta\phi_{\omega}} = \frac{mc^2}{\hbar\omega} = \frac{\lambda_{\omega}c}{\lambda_{\text{db}}v} \approx 1 \times 10^{10}, \tag{1.6}$$

based on cold atoms v.s. near infrared light. Of distinction here is that for photonic based systems the speed of light is a constant factor in the scalability, whereas for atomic systems we can affect both the de Broglie wavlength and the atomic velocity (by cooling). Atomic devices therefore have the possibility to out-perform optical devices, offering higher sensitivities. This particular comparison is a little unfair, however, as mile long atomic systems are somewhat unfeasible whilst routinely made in FOGs. Another consideration to make is the scaling with the number of particles, where typical laser beams can produce 1×10^{14} photons s^{-1} compared with 1×10^{7} atoms s^{-1} made by typical atom traps. With Bose-Einstein condensates this number decreases even further, with condensates of 1×10^{5} atoms produced in around 1 s in setups arranged for speed [36, 37].

Interferometers based on atomic beams remain the most sensitive atomic Sagnac interfereometers to date. Gustavsen et al. [38] report a short term sensitivity of $6 \times 10^{-10}\,\text{rad}\,\text{s}^{-1}/\sqrt{\text{Hz}}$ [39] using a beam of $\approx 1 \times 10^{11}\,\text{s}^{-1}$ Caesium atoms. The apparatus is over 3 m long however, and each Raman beamsplitter is separated in space, requiring its own optics. The overall interferometer area is $22\,\text{mm}^2$, with the arms maximally separated by 24 µm. Fountain interferometers are more compact and allow the pulses to share the same optics, removing uncertainties associated with differences between the separate beam alignments. The use of cold atom clouds also increases the sensitivity of the instrument, as we know the phase difference is inversely proportional to the atomic velocity. Dutta et al. [40] report a sensitivity of $1 \times 10^{-7}\,\text{rad}\,\text{s}^{-1}/\sqrt{\text{Hz}}$ with a continuously operated atomic fountain, which is able to prepare a cold atom cloud whilst simultaneously performing interferometry, cutting dead time in the interferometer.

There are a class of atom interferometers in which a reflection operation (or device) is not needed. Guided interferometers, where atoms are confined to some looped geometry, are becoming a more attractive way of generating large interferometer areas with a small experimental footprint [41]. There are a number of ways to generate such a trap, including magnetic storage [42, 43], dressed RF potentials [44, 45], time averaged dipole potentials [46–48], and computer generated holographic patterns [49, 50].

1.3 BEC interferometer in freefall

Let us turn our attention to the configuration we wish to investigate - that is an atom interferometer utilising a BEC. The specific geometry we are investigating is where the BEC is dropped under gravity during the interferometry sequence which will generate a Sagnac area, making it sensitive to rotations. BEC interferometry has advantages associated with the condensate's narrow momentum width - namely the ability to address the entire cloud with splitting processes, and an associated large coherence length [35, 51]. For small drop distances relative to the distances covered by fountains and beam experiments, we predict this scheme will be competitive with them in terms of sensitivity.

1.3.1 Description of Apparatus

The BEC interferometer in freefall is configured in the following way, detailed in chapter 3. A BEC is generated and held in an optical dipole trap. The BEC is then released and simultaneously split using an external-state beam splitter based on a Kapitza-Dirac pulse. There are no longer any confining or levitating forces and the BEC is allowed to accelerate under gravity. The split should be perpendicular to the direction of gravity in order to maximise interferometer area (see below and equation 1.5). The split packets then travel apart for the symmetric interferometer time, τ, before being reversed in momentum using a Blackmann pulse [52]. After another τ has passed the packets are recombined using a similar beam-splitting operation. As the atomic ensemble accelerates under gravity it will trace out a kite-shape in space, as shown in figure 1.2.

If no phase source is present then all population should then return to the central mode, the BEC at rest. Any accelerations of the cloud during the time

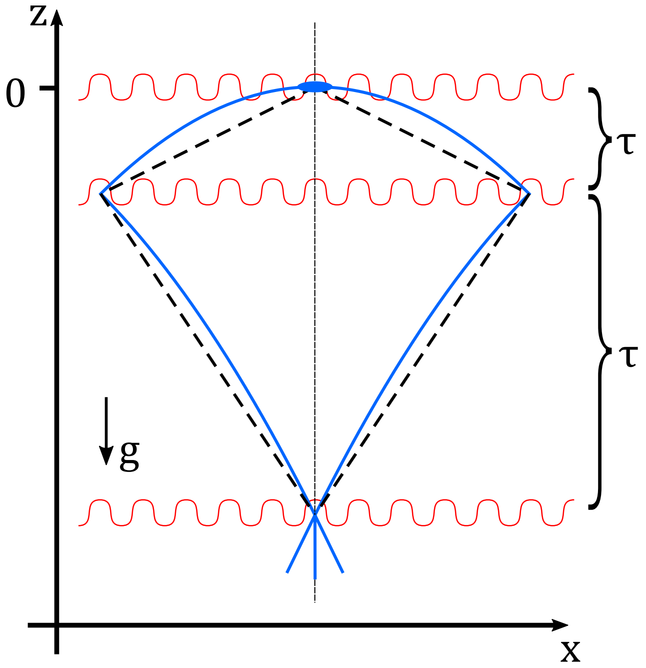

FIGURE 1.2: Space diagram of the freefall BEC interferometer scheme, showing the *position* of the BEC as it falls under gravity, g, during the interferometer sequence. A coherent pulse (red) splits, reflects and recombines the BEC as it falls (solid blue curve). The same beam, which encompasses the entire interferometry sequence, is used for all three pulsed operations. The time between pulses, τ, is shown for reference. The dashed-line kite shape has the same area as the blue curve. This is discussed more in chapter 3.

the interferometer is active, such as from the Coriolis force associated with a rotation, will result in population remaining in the split packets. What is of note in this scheme is that the interferometer (area) scales with the cube of the symmetric interferometer time, τ,

$$A_{ff} \propto \tau^3, \tag{1.7}$$

which we detail in chapter 4. A 10 ms drop corresponds to an area of around $A_{ff} = 0.23\,\text{mm}^2$ in our scheme. Therefore, small increases in the BEC drop time improve the sensitivity of the instrument dramatically. The smallest rotation rate one can detect is given by the sensitivity of the apparatus. The sensitivity in the the simple case where the phase variance is limited by shot-noise [53, 54], is given by

$$\delta\Omega = \frac{\hbar}{2mA\sqrt{N}}, \tag{1.8}$$

where N denotes the total atom number involved in the interferometer, which arises from considering noise from number fluctuations [53]. A freefall interferometer with the area above producing a BEC of 1×10^5 atoms every second results in a sensitivity of roughly $1 \times 10^{-6}\,\mathrm{rad\,s^{-1}}/\sqrt{\mathrm{Hz}}$. An equivalent sensitivity can be found for a (guided) ring interferometer with a radius of $r_0 = 270\,\mu\mathrm{m}$, which we motivate in the following section. To date, guided interferometry experimentally reports measured sensitivities on order $1\,\mathrm{rad\,s^{-1}}/\sqrt{\mathrm{Hz}}$ [55], with significant potential for improvement [56, 57].

1.3.2 Confined ring geometries

For the freefall interferometer, at its greatest point the split wavepackets are roughly $\approx 100\,\mu\mathrm{m}$ apart. Compared to the drop distance which is over $\approx 2\,\mathrm{mm}$, this means the interferometer area has an aspect ratio of roughly 20:1. One way therefore to increase the interferometer area in this configuration is to increase the separation in the horizontal (perpendicular to gravity) direction. One way to achieve this is by using higher momentum splitting ($n > 1$ in equation 1.5 above). Higher momentum states are however more difficult to excite efficiently, which is covered in greater detail in chapter 3. More efficient pulses, or pulse schemes may address this issue [58–60].

Guided interferometry is another attractive option. A method of generating optical potentials useful for guiding cold atoms we are looking into is the phase-only Fresnel zone plate (FZP). Based on the Fresnel lens of alternating zones one can shape light into arbitrary patterns. We wish to generate ring traps via this method, the details of which can be found in chapter 5, building on work done previously by Henderson et al. found at reference [61]. Rings with radii on the order of 100 µm have been produced [62], with possible scaling up to mm. We also have the possibility to generate and use dark-field traps, where atoms are stored in intensity minima. The combination of these effects can increase our sensitivity by orders of magnitude.

1.4 Outline of Thesis

This thesis is broken into three separate parts. Part I describes a new apparatus we built to motivate a new quantum technology. Here we describe the building blocks required to create a Bose-Einstein condensate from vacuum to atom trap. Part II deals with freefall interferometry and the changes that have been made to the apparatus common to previous work in the group to adapt to this scheme [63, 64]. Part III then goes on to motivate the hybrid near-field Fresnel zone plate, expanding on work by Henderson et al. [61, 62] to generate a new generation of plates for future experiments.

Part I contains work done by the author in conjunction with V. Henderson [65], part II uses apparatus constructed by A. Dinkelacker [66], B. Robertson [63] and A. Mackellar [64] with further improvements and adaptions by the author, and part III consists of new work by the author based on previous work by V. Henderson [65].

Publications featuring the author during their time at Strathclyde University can be found at the following references: [62, 67].

Part I

Apparatus

Chapter 2

Vacuum apparatus and magneto-optic trap

The creation of a Bose-Einstein condensate (BEC) is not a simple process. To achieve BEC, atoms must be cold and dense enough for their de Broglie matter-wave component to overlap [68–71]. We must push particles to some of the coldest temperatures it is humanly possible to achieve. To achieve this we turn to the realm where light and matter interact, trading energy quanta in such a way that the system is biased toward energy loss. When one method runs out of effectiveness, we can then change the way we hold, cool, or compress the ensemble as best suits our circumstance. The apparatus to produce such a state is also non-trivial; no simple fridge will suffice.

In this chapter we will cover some of the experimental necessities to produce a BEC of ^{87}Rb . Firstly, we shall describe the relevant forces for cooling and trapping of neutral atoms into a magneto-optical trap (MOT). A MOT provides the starting point for many cold-atom experiments, such as those involving the production of a BEC. We then cover the construction and optimisation of our vacuum chamber with a 2D+ MOT, a high flux atomic funnel which is key in speeding up BEC generation. Finally, we outline the path we take to achieve condensation, as has been routinely achieved in our group for many years now. For clarity, the vacuum chamber described here with the 2D+ chamber was newly constructed during the course of this PhD and is not the same chamber as is described in section 2.4 and in the following chapters, whose construction and characterisation has been fully described previously in the work of Dinkelacker [66], Robertson [63] and Mackellar [64].

2.1 Light-matter interaction forces

To achieve BEC, atomic physicists require the ability to cool and trap atoms. The way atoms interact with fields, namely with light and magnetism, provides us with a foundation to accomplish this. The cooling and trapping of neutral atoms is a well established and discussed topic, with many good texts on the subject [70–74]. Below we will discuss basic necessities to understand some of the detail further in this text.

2.1.1 Atomic Scatter

The first of two main forces we will deal with is that from atomic scatter. Atoms in a monochromatic light field with frequency ω will scatter by spontaneous emission with a rate, Γ_{sc} given by,

$$\Gamma_{sc} = \frac{\Gamma}{2}\frac{I/I_{sat}}{1+\frac{I}{I_{sat}}+\frac{4\Delta^2}{\Gamma^2}}, \tag{2.1}$$

where we define Γ as the natural linewidth and Δ as the detuning from the transition wavelength, ω_0, such that $\Delta = \omega - \omega_0$. Here we denote the beam intensity I and the saturation intensity I_{sat}, which are defined by the relationship with Ω_R the resonant Rabi frequency [74],

$$\frac{I}{I_{sat}} = 2\left(\frac{\Omega_R}{\Gamma}\right)^2. \tag{2.2}$$

The relation in equation 2.1 has a Lorentzian lineshape when plotted against Δ, reaching a peak when $\Delta = 0$. Scattering from spontaneous emission / absorption carries an associated change in momentum from the photon recoil of $\hbar k$, hence the force on an atom can be expressed as *force = change in momentum × rate of photon scatter events*, i.e:

$$F_{scatt} = \hbar k\Gamma_{sc} = \hbar k\frac{\Gamma}{2}\frac{I/I_{sat}}{1+\frac{I}{I_{sat}}+\frac{4\Delta^2}{\Gamma^2}}, \tag{2.3}$$

where the wavenumber, $k = 2\pi/\lambda$, is associated with the wavelength of the incident (photon) field, λ, and $\hbar$ is the reduced plank constant. The trick in order to make this force relevant to cooling an atom is to make it velocity selective.

Consider an atom in motion, with velocity, $\vec{v}$, travelling in the opposite direction of the beam propagation with the wavevector, $\vec{k}$. If the beam is resonant ($\Delta = 0$) then the atom will continually experience an acceleration opposite to its initial direction of propagation, even eventually reversing the direction of the velocity. We wish to diminish the effect of the force as the atom slows down, hence we need to make the force velocity dependent. Consider now the Doppler effect, the frequency of a wave is shifted by $\omega' = \omega - \vec{k} \cdot \vec{v}$ for the atom. The detuning, as defined above, can then be expressed in the frame of the atom as;

$$\Delta' = \Delta - \vec{k} \cdot \vec{v}, \tag{2.4}$$

where this $\vec{k} \cdot \vec{v}$ means that atoms experience a stronger force when they have a velocity that Doppler shifts the frequency of the beam toward resonance, i.e. $\Delta = \vec{k} \cdot \vec{v}$. The force weakens as the atomic velocity is decreased towards 0. Introducing a second, counter propagating beam with a similar detuning can then slow atoms toward $v = 0$. Six beams, one for each direction in 3D space, used to slow atoms in this way is referred to as *optical molasses*, where the slowing force originals from light-interaction only.

From this simple presentation of the scattering force it may seem that one may be able to stop an atom in place using this technique, but the truth is not as simple. The force is derived from incoherent scatter, which relies on the absorption and re-emission of a photon, and it is this spontaneous emission that limits us in the Doppler case. The *Doppler Limit* is the theoretical minimum temperature achievable, $T_D = \frac{\hbar\Gamma}{2k_B}$ [74–76]. However, sub-Doppler temperatures are experimentally achievable with techniques such as Sisyphus cooling [76, 77] and Grey molasses [67, 78, 79].

This orientation does not *trap* the atoms, as there is no spatial confinement and atoms will eventually diffuse from the beams. We must consider additional effects in order to successfully trap cold atoms in space.

2.1.2 Magneto-Optical effects for trapping

To successfully trap atoms we must consider the light-induced scattering force along with the Zeeman effect, whereby in the presence of a weak magnetic field, the degeneracy on the atomic hyperfine levels is lifted and the energy of the magnetic/Zeeman sub-levels, m_F, are shifted by a quantity [74],

$$E_{ze} = \mu_B g_F |\vec{B}| m_F, \tag{2.5}$$

where the Bohr magneton and the Landé g-factor are represented by μ_B and g_F respectively. Introducing a spatial variation (or gradient) in the magnetic field would therefore create a gradient in the energy landscape. The net result of this is that we can make the detuning from the atomic transition spatially dependent now. We generate a strong linear gradient with a set of coils with currents running counter to each other - i.e. a quadrupole magnet in anti-Helmholtz configuration, such as in figure 2.1. In essence, as atoms move from the centre of the quadrupole where the net field is zero, we can shift the energy of the atom up to make it more resonant with a (red-detuned) beam.

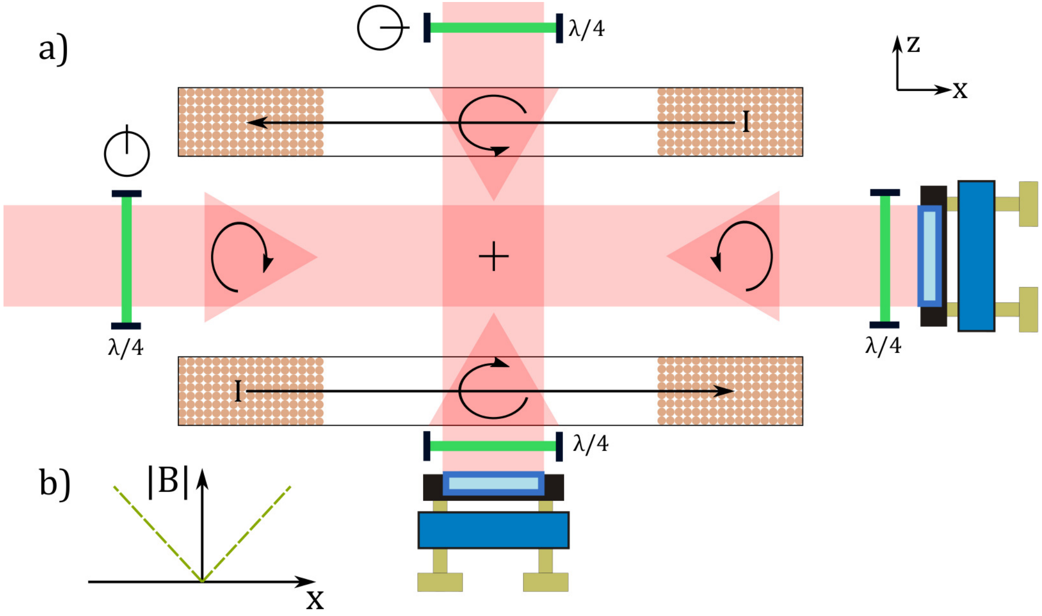

FIGURE 2.1: Illustration of the 3D MOT scheme in the x-z plane. a) Crossed beams at the centre of a quadrupole magnet in an anti-Helmholtz configuration. Running counter currents between the coils generates the magnetic field 0 at the centre. The triangles denote the polarisation of the beam in that direction. The orientation of the $\lambda/4$ waveplates between the two axes must be orthogonal, as the magnetic flux changes direction between the coil axis (z) and the perpendicular (x). b) Magnitude of the magnetic field as a function of distance from the centre of the coils.

We still need to circumvent the problem of what direction the force takes with respect to space. With unpolarised light all m_F levels are equally excited, but with polarised light selection rules force us to consider a family of $m_F \rightarrow m'_F$ transitions. Circularly polarised light, that is light polarised so that the E-field vector precesses around the quantisation axis (set by the B-field), will promote $\Delta m_F = \pm 1$ transitions, known as the sigma transitions, σ^+ and

σ^-. Consecutive σ^+ (σ^-) transitions will *pump* atoms into the stretched state - that is into the highest (lowest) m_F state available. This state is also the one most affected by the magnetic field and hence experiences the largest energy shift, as seen in equation 2.5. If this stretched state then meets the resonance condition on account of both the spatial (magnetic) and velocity (Doppler) shifts in detuning then the atom will undergo a scatter. In essence, the description (in one dimension) of the detuning can be extended to include the spatial dependence on magnetic field:,

$$\Delta' = \Delta - \vec{k} \cdot \vec{v} + \frac{g_F m_F \mu_B}{\hbar} \frac{dB}{d\vec{r}} \vec{r}, \tag{2.6}$$

where we have assumed the field is linear around the quadrupole centre at $r = 0$, where $|B| = 0$. This assumption allows us to take the gradient of the B-field multiplied by the distance from the trap centre (at $\vec{r} = 0$). From this, we can see that the magnetic gradient provides a spatially dependent force required for trapping the atoms.

The configuration is therefore to have magnetic gradient, with the σ_+ (σ_-) light propagating against the side where the field is positive (negative)[1]. Extending to three dimensions (with beam pairs along each axis usually) this is known as the magneto-optical trap (MOT). The interplay between the field zero and the beam propagation direction will be important in section 2.3.3 where we examine a peculiarity with respect to beam polarisation.

With coil pairs in an anti-Helmholtz configuration, a fact to remember is that along the coil axis the direction of the field is opposite to that in the radial, hence the polarisation of the beams between these will be orthogonal. For instance, if a Helmholtz coil pair is separated in z then the angle of the $\lambda/4$ waveplates of the beams in this axis are set at 90° from those in the x-y axis. This ensures the correct circular polarisation is used for each axis. This is shown in figure 2.1. Also, if one is to reverse the direction of the current in the magnetic coils then the opposite of a trap is generated - atoms are ejected from the trap centre. These two facts are useful to consider when aligning a MOT for the first time. If the polarisations are set correctly, then it may be prudent to invert the coil current.

Purely magnetic trapping is possible, as a gradient in the potential is evident. Two things become evident in practical considerations. The sign of the

---

[1] This is in the laboratory frame. The relative direction of travel in respect to the quantisation field is what makes the transitions σ^+ or σ^- [74].

m_F state becomes important, as it prefaces the gradient of the B field, meaning that atoms either become "high-field seeking" or "low-field seeking"; attracted to or repulsed by strong magnetic field amplitude. In either case, atoms will need to be pumped into the same (stretched) state otherwise a large fraction of the population will go un-trapped. Magnetic gradients on order Tesla per meter (T/m) are required to trap atoms at room temperature. As a consequence magnetic trapping for neutral alkali atoms usually takes place once the atoms are already cooled.

In essence, appropriate magnetic fields in combination with a pair of counter-propagating circular-polarised (cooling) laser beams which are detuned to the red of the atomic transition create position-dependent laser scattering rates which enable magneto-optical trapping. A touchstone of atomic physics, many parts come together to generate an effective MOT. Recently, work towards reducing the experimental size, weight and power (beams, mirrors, etc) has been done with the *grating MOT* [80–83]; a single-beam, grating-based device for trapping and cooling of atoms, using the diffracted orders to generate the necessary beam-geometries.

2.1.3 Dipole Potential

An atom interacting with a field is influenced by its intensity landscape as well. This is to say that a strongly focused beam can be used to hold atoms through a separate mechanism to the one described above. Named the *dipole force*, it is a key element in experimental cold-atom physics [84]. Where the scattering rate in equation 2.1 is concerned with spontaneous emission, the dipole force arises from the in-phase *dispersive* component of the induced atomic dipole moment [85].

Analogous to the Zeeman shift described in section 2.1.2, the AC Stark effect is a light-induced energy shift of the atomic levels. This intensity dependent energy shift generates a potential. In the rotating wave approximation (where $|\Delta| \ll \omega_0$) the dipole potential, U_{dip}, is described by the equation [74, 85],

$$U_{\mathrm{dip}}(\vec{r}) = \frac{\hbar\Gamma^2}{8I_{sat}}\frac{I(\vec{r})}{\Delta}, \tag{2.7}$$

where we see that potential depth is proportional to intensity, and inversely proportional to detuning. Given that force is the gradient of potential we see that:

$$F_{dip} = -\nabla U_{\mathrm{dip}} \propto \frac{dI(\vec{r})}{d\vec{r}}, \tag{2.8}$$

where spatial gradients in the intensity landscape give rise to the dipole force. Note that the sign of the detuning in equation 2.7 will change the direction of the force; red detuned beams (i.e. $\omega < \omega_0$, Δ is negative) draw atoms to regions of high intensity, and blue ($\omega > \omega_0$, Δ is positive) push them away. We divide these into two classes of dipole traps; red (attractive) and blue (repulsive).

Note that the scattering rate, equation 2.1, depends on I/Δ^2 compared to the I/Δ in the dipole potential case. At larger values of detuning, therefore, the dipole force plays a more dominant role. Indeed, when concerned with generation of the BEC, we cannot rely on the scatter force around temperatures where recoil is on a similar order of magnitude, as this will lead to losses from our trap.

Also note that ^{87}Rb has two lines, the D_1 and D_2 at 795 nm and 780 nm respectively. A more complete version of U_{dip} includes contributions from both lines [85]. More comprehensive reviews of the theory and implementation of the dipole force can be found at references [68, 69, 84, 85]. We revisit dipole traps in chapter 6, with respect to the novel generation in the near field.

2.2 Vacuum chamber for Bose-Einstein Condensate production

Essential to any cold-atom experiment is the vacuum chamber, or more specifically, having a low background pressure. Atomic experiments are done in vacuum in order to minimise collisions with background gasses. This becomes especially important when one is considering generating BECs, as in order to guarantee a long BEC lifetime it must be created in UHV, or in ultra-high vacuum. UHV is generally defined as a background pressure below 1×10^{-9} mbar [86]. BEC experiments generally require lower pressures, nearer 1×10^{-11} mbar as the BEC lifetime scales inversely with the background pressure [87].

On the other hand, MOTs are usually loaded from a background vapour of the atomic species used. The pressure of this background vapour for alkali atoms is on order of 1×10^{-7} mbar. It is therefore pertinent to separate where the BEC is formed from where the MOT is loaded. A dual chamber system achieves this, with a source MOT in a "high pressure" reservoir feeding a "low pressure" chamber where the BEC is eventually formed. The pressure difference is maintained by a differential pumping tube (DPT), which is effectively a long pipe with a small aperture through which we can funnel atoms.

This flux of atoms is provided by a 2D MOT, a conventional MOT along two axes, but left unconstrained along the third [88]. Atoms here are cooled and trapped along two dimensions and are thus funnelled into an atomic beam of sorts. This beam can then be directed along the DPT and into the awaiting 3D MOT in the low pressure chamber. A higher flux of atoms can be achieved by adding an additional beam along the axial direction - what is conventionally known as a 2D plus (2D+) MOT [89]. We construct and evaluate the performance of this in section 2.3.

The following sections will describe the new chamber apparatus, with a particular focus on the 2D+ MOT.

2.2.1 Vacuum Apparatus

The dual chamber apparatus is comprised in the following way, of which a 3D render of can be found in figure 2.2. Two glass cells ($100 \times 30 \times 30\,\mathrm{mm}^3$) are connected to a central stainless steel block which has a partition in the centre, separating the two. On the high pressure (2D, right of figure) side a $220\,\mathrm{L\,s^{-1}}$ (Agilent Starcell) Ion Pump and four rubidium dispensers (SAES Getters) are attached. The low pressure (left of figure) has a $45\,\mathrm{L\,s^{-1}}$ (Gamma Vacuum Diode) Ion pump and a non-evaporative getter (NEG, SAES Getters Capaci-TORR D400-2). For ease of pumping the system with a Turbo-Pump each side is fitted with a valve (MDC Vacuum MAV-150-V). The distance from the exit of the 2D+ MOT to the centre of the 3D MOT is roughly 370 mm.

Specific characterisations of our bakeout procedure, including temperature and pressure monitoring can be found in Ref. [65]. The parts were degreased (soak in MICRO90 solution) and ultrasonic cleaned (20 min at 41 °C in acetone followed by the same in isopropanol). The chamber was then baked for two weeks above 200 °C before being finally sealed at around 4.6×10^{-11} mbar on the low pressure side, and less than 1×10^{-9} mbar on the high pressure side.

The differential pumping tube (DPT) is fitted inside the main vacuum body and separates the two chambers. The DPT extends into the 2D chamber such that the aperture lines up with the end of the glass cell. The DPT is staggered, i.e. tapers open in segments, with a 2 mm diameter opening, expanding to

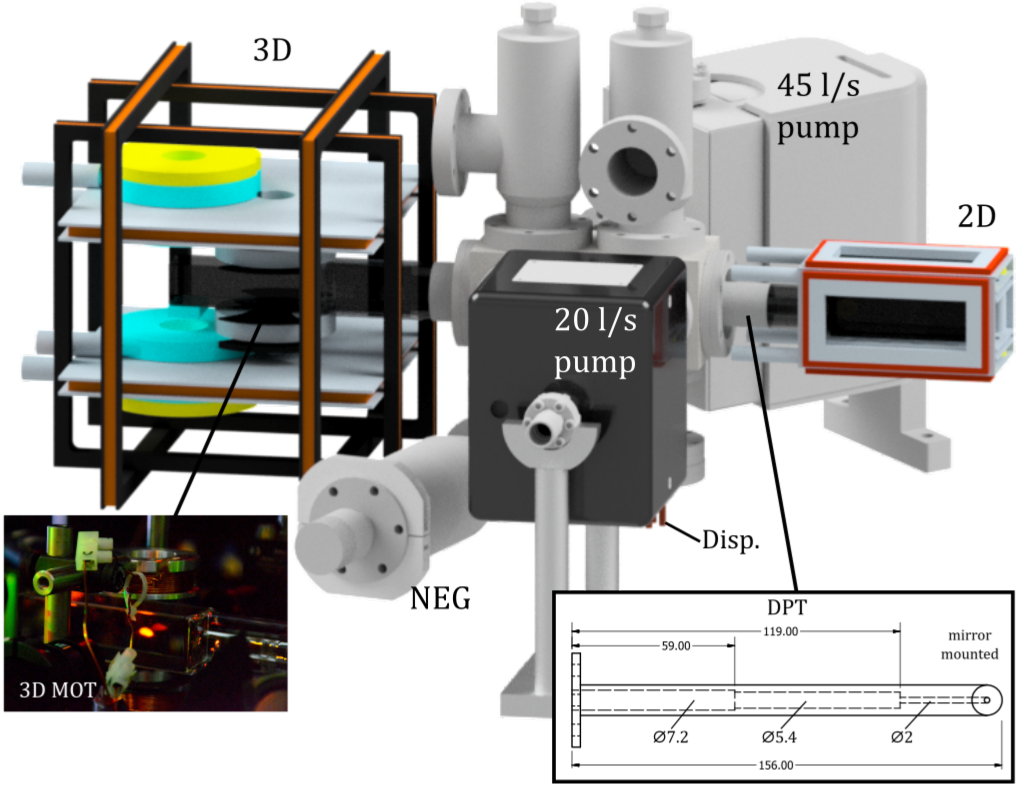

FIGURE 2.2: Render of vacuum apparatus, including the two chambers, separated by the differential pumping tube (DPT - inset bottom right). At the tip of the DPT a protected gold mirror is attached to provide a reflective surface for the $2D^{+}$ MOT. The two pumps attached are also labelled, in addition to the NEG. The blue and yellow highlighted parts make up the 3D printed watertight enclosure for the high current coils.

5.85 mm then 7.2 mm in diameter. The overall length of the DPT is 158.98 mm. This shape accounts for the drop due to gravity as well as the (thermal) angular spread of atoms through the tube, minimising collisions with the tube walls whilst maintaining a narrow atomic “beam”. The DPT is able to maintain ratio of pressures between the two chambers of of 2.1×10^{3}.

Highlighted in blue and yellow in figure 2.2 are the 3D printed enclosure for the high current quadrupole coil pair for magnetic trapping. The coils are made using 1.85 mm enamelled copper wire wound 17×17 turns across. The coil pair has a resistance of $1.34\,\Omega$, which will require water cooling in order to run currents $>$20 A through in order to generate magnetic gradients of $\approx$ 200 G/cm for trapping. The enclosure is 3D printed from sintered nylon (SLS Nylon PA2000, printed by 3DAlchemy). The coils sit on 1 mm copper feet, and have thin copper prongs on the inside face of the coil in order to maximise water exposure and heat dissipation. This is illustrated in figure 2.3 The 10 mm inner diameter nozzles (hose barb) for water ingress/egress form part of the printed structure. Since the coils are submerged inside the enclosure we trail the wire out the nozzle, following the flow of water to a T-junction in the hose. Here, the wire is then fed through a thermocouple compression fitting (RS 839-9496), which acts as a watertight seal, allowing us to connect the coils directly to a power supply. The coil wire is enamelled, which acts as a barrier such that we avoid making the compression fitting live, bypassing a large resistive load. In previous designs we have soldered the current carrying wire to a metal hose fitting, making it live, in order to deliver current.

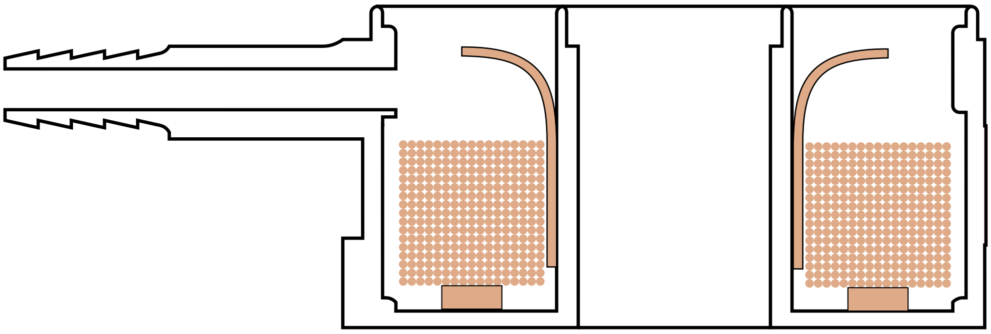

FIGURE 2.3: Illustration (not to scale) of the coil, copper feet and prong inside the 3D printed coil enclosure. There are three feet, 1 mm in height, and three prongs fitted inside each coil enclosure. These help dissipate heat from the sides of the coil that do not have contact with the cooling water.

2.2.2 Dispensers

We use Rubidium alkali-metal dispensers as an atomic source. Four dispensers (SAES AMD) are arranged in a circle, connected at the end of a copper feedthrough on the underside of the vacuum chamber. Dispensers generally consist of a small bar of alkali-metal compound that when heated sufficiently will sublime atomic alkali from its surface. The heat is delivered by resistive heating from passing a current through the ceramic compound. Dispensers have a finite lifetime, hence we install 4 to future-proof for this.

The background vapour pressure in the 2D MOT chamber is directly measured by sending a probe beam through a non-trapping region of the 2D MOT and scanning the frequency to measure the full ^{87}Rb D$_2$ line Doppler spectrum. We use a probe beam with an intensity of 0.46 mW cm^{-2} or roughly $0.3 I_{sat}$.

From a fit of the Doppler spectrum we can estimate the background pressure using the `Elecsus` program [90, 91]. The program fits the Doppler spectrum to an equivalent temperature, and from this temperature we can make a lower-bound estimate of the vapour pressure [92–94].

In figure 2.4 we plot the fully optimised 2D MOT (including polarisation considerations below) loading rate as a function of the dispenser current, along with the corresponding vapour pressure. We operate at a vapour pressure slightly lower than where the maximum flux occurs (corresponding to dispenser current of 6.8 A) to ensure the 3D MOT does not completely saturate within 1 s when recording our polarisation results below in section 2.3.3.

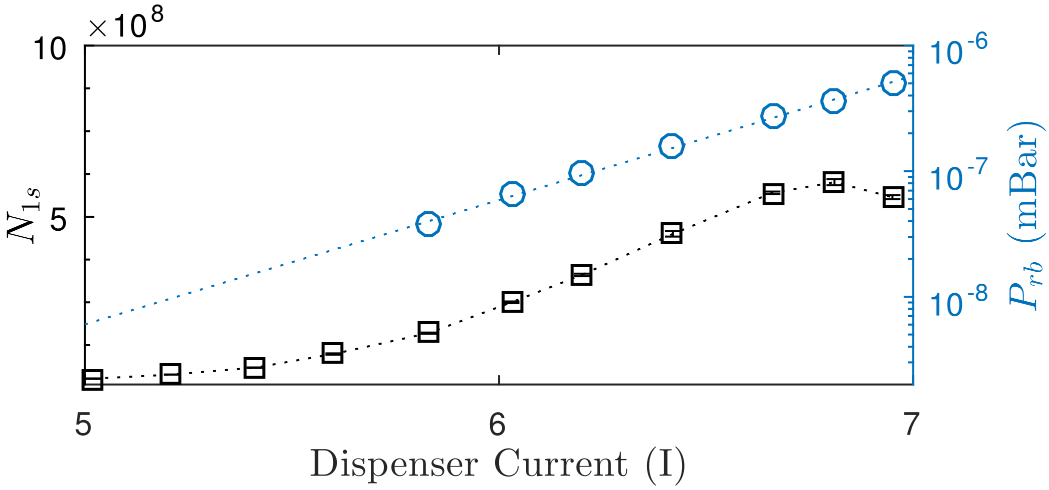

FIGURE 2.4: The number of atoms loaded in 1 s in the 3D MOT (black squares) as a function of different currents through the dispensers. The vapour pressure (blue circles) is directly measured with a 0.3 I_{sat} probe beam, whose frequency is scanned to produce Doppler spectroscopic peaks. These peaks are then analysed by the Elecsus program to convert into a pressure[90]. Flux improves until a pressure of approximately 1×10^{-7} mbar, where background collisions begin to degrade performance.

Note an experimental oversight where the activation current (roughly 5 A) is higher than the manufacturers specification, which we attribute to significant heat dissipation through the *copper* feedthroughs used. Consequent designs have noted this and the group now uses nickel or molybdenum based feedthroughs for dispensers, where activation is now observed closer to 4 A.

2.2.3 2D magneto-optical trap design

Here we will generally describe the 2D MOT apparatus, found on the high-pressure side of the dual chamber. Performance of the 2D+ MOT can be found in section 2.3.

Our 2D MOT is a segmented design based on reference [95], a diagram of which can be found in figure 2.5. The multiple segmented design occupies a smaller physical volume on the optical table, not needing the large expansion optics necessary for elliptical MOT beams common in 2D MOTs. In the elliptical design, the wings of the Gaussian beam mean the MOT confinement is weaker near the entrance of the differential pumping tube and thus has a greater angular spread. In the segment design you generate multiple smaller MOT segments which then feed into each other to produce the atomic beam. You can then physically bring the last MOT region closer to the DPT, allowing more atoms to propagate through the DPT aperture, increasing the atomic flux.

Our laser system for both 3D and 2D MOTs consists of two 780 nm home-built ECDLs, operating with an output power of approximately 50 mW - the details and construction of these can be found at references [63, 65]. Our cooling laser is 12 MHz ($\approx 2\Gamma$) red detuned from the D_2 cooling transition ($^5S_{1/2},\ F = 2 \rightarrow {}^5P_{3/2},\ F = 3$) and the is repumper locked to the $^5S_{1/2},\ F = 1 \rightarrow {}^5P_{3/2},\ F = 2$ transition. Both cooling and repump beams are coupled into a polarisation maintaining fused fibre splitter (Laser2000 CP-PS-P-1x2-780 series) which that splits the coupled input power equally between multiple output fibres. See section 2.2.5 for more details on the fibre splitters. Each output is then collimated and expanded to a $1/e^2$ waist of 9.3 mm.

Light then enters our compact 'distribution block' that divides the light equally between three 'MOT regions'. The block consists of a series of half ($\lambda/2$) waveplates and polarising beam splitters (PBS) housed in a custom built aluminium mount (see top of figure 2.5). The separation between each region is set by the thickness of the $\lambda/2$ waveplate mount at 8 mm. The waveplates are adjusted by rotating inside the mount, and secured using a locking screw. Light from the reflected ports of each PBS passes through quarter waveplates, setting the polarisation to circular for trapping in the 2D MOT chamber. Individual polarisation and intensity can be set for each cube, used to correct for small discrepancies in the fibre splitter output. Each beam is retro-reflected by

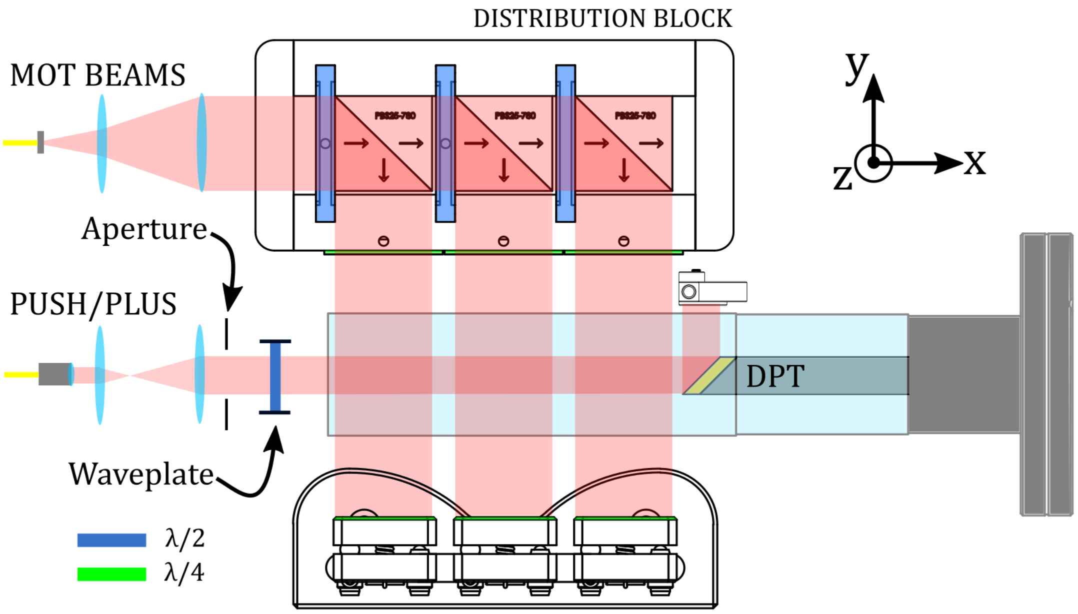

FIGURE 2.5: View of the 2D$^+$ apparatus in the x, z plane, where gravity is in the $-z$ direction. Beams in the veritcal (z) axis are omitted for clarity, but are identical to those shown (in y). The central chamber is 30 mm × 30 mm × 150 mm in size, and all optics are inch in diameter. The MOT regions are each separated by 8 mm, the last of which ends at the tip of the gold mirror that is secured to the end of the differential pumping tube. A 3.13 mm $1/e^2$ waist beam, retro-reflected from the gold mirror in vacuum and a dielectric d-shaped mirror outside the chamber, forms the plus beam along the centre of the cell. An aperture was used to limit the beam width to fit inside the differential tube with no retro-reflection, forming the 1 mm waist push beam. Figure adapted from [65].

a mirror with a $\lambda/4$ plate glued to the front of it to ensure the correct handedness of sigma polarisation is incident on the atoms upon reflection.

A set of rectangular coils produce the quadrupole field for trapping, separated along the z axis (out of page in figure 2.5). The coils measure 100 x 45 mm, centred around the glass cell window. The modelled magnetic field is plotted in figure 2.6, alongside an outline of the glass cell and MOT beams. A set of 1.1 G A^{-1} shim coils in the y and z axes allow the atomic beam to be moved in the transverse plane.

The whole design takes up no more than 20 cm^2 on the optical table and the use of optical fibres to transport the light allows for changes to the laser system, without disturbing the 2D MOT alignment. See section 2.2.5 for more details on our fibre usage.

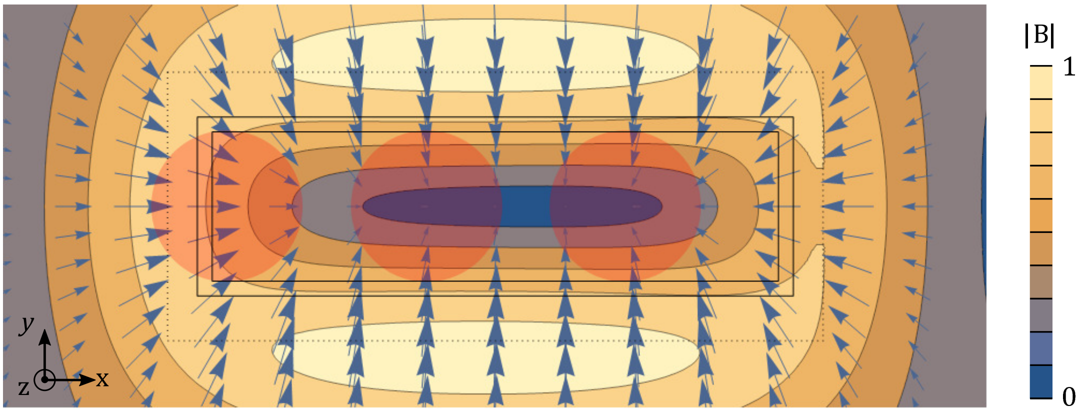

FIGURE 2.6: Contour and vector plot of the magnitude ($|B|$) and direction (arrows) of the field of the 2D$^+$ MOT in the x-y plane (at $z = 0$). The glass cell boundary is denoted by the solid line, and the coils by the dotted line. The red circles show locations of the MOT cooling beams, each with a $1/e^2$ waist of 9.3 mm .

2.2.4 The 2D+ MOT

The 2D MOT's primary function is to funnel atoms through the DPT aperture. There is a small cone of angles of which atoms from the 2D MOT will pass through to the 3D MOT. In order to increase the yield of atoms that cross the distance a push beam is used [96–98]. The push beam is a small, off-resonant beam that pushes atoms along via radiation pressure [99], and is considered most effective tuned to resonance. Some atoms with velocities in the $-x$ direction (see figure 2.5), can be reversed in the presence of the push beam [100].

The 2D+ MOT is an extension of this idea, in which an additional 'plus' beam is added along the non-trapped axis of the 2D MOT [89, 101, 102]. Whilst the push beam is only as wide as the DPT aperture, the *plus* beam is much wider than this, reflecting off the mirror which forms the front of the DPT. This now retro-reflected beam forms a rudimentary cooling beam, but with a hole in the centre along the 2D MOT axis (x). There is still pushing at the centre of the plus beam, where there is no counter-propagating beam, so that atoms that fall into the centre of the plus beam are propelled downstream. We expect atoms to be cooled via optical molasses along this axis since there is generally no magnetic field here, but this is not strictly true as we discuss in section 2.3.3. Orginally shown by Dieckman et al. [89], the 2D+ improves flux by narrowing the axial velocity distribution of atoms reaching the 3D MOT, increasing capture.

Our push/plus beam is derived from the same cooling laser as described in section 2.2.3, but has an independent frequency detuning control and is coupled into its own fibre (Thorlabs PCM series). The fibre output is collimated and expanded to a waist of 3.13 mm to form the plus beam. The beam has a peak intensity of 2.1 mW cm^{-2}. This beam is retro reflected by means of a gold mirror situated in vacuum (Edmund Optics 47-114) and a dielectric pickoff mirror (Thorlabs BBD05-E03), as shown in figure 2.5. The edge of these mirrors and the end of the last MOT segment are as close as possible to maximise the first MOT segment overlap in the chamber (left most circle in figure 2.6).

2.2.5 Note on the usage of fibre splitters

It is common in most experiments of this ilk to distribute light using PBS cubes in free space. We opted to instead use fibre optics to distribute the light amongst both our 2D and 3D MOT systems, requiring the use of fibre splitters in-lieu of PBS cubes for portioning off light. The fibre splitters here are *fused fibre couplers* - where two fibres are “fused” together by removing the cladding and intertwining the cores. At the fusion point, intensity is transferred between fibre cores as the evanescent part of the wave outside one core leaks into the other. The length of the fusion junction determines the efficiency of the light transfer. Junctions can combine light if both fibres have light coupled into them, or split if only coupled into the one. Multiple splits can be achieved by chaining fusions points together, but typically performance diminishes with additional fusion points. Any unused fibre ends are terminated - usually by crushing the fibre end in order to reduce back-scatter.

Trapping and cooling of atoms in MOTs is sensitive to changes/fluctuations in the light polarisation. Therefore, it is necessary to use polarisation maintaining (PM) fibres for this application. PM fibres have a “fast” and “slow” axis corresponding to the two birefringent axes the fibre has been constructed with. The input light must have its polarisation axis match with one of these axes in order to maintain its polarisation along the length of the fibre. The polarisation extinction ratio (PER) is a useful quantifier of this, which is defined as the ratio of the power in the aligned (i.e. linear) polarisation to the total power, reported in decibels (dB).

Typical fibres (e.g. Thorlabs PCM) have a reported PER of 20 dB. PM fused fibre couplers are the same, but the fusion point limits our ability to control the PER with careful alignment, as it is set in construction. It is therefore impossible to optimise each output independently without affecting the other outputs.

However, using a Schäfter+Kirchhoff polarimeter (SK010PA-NIR - see section 2.3.2), we could efficiently make a good compromise in beam-fibre polarisation alignment thanks to the device. We first aligned the input fibre polarisation, then checked all the outputs in turn, optimising each until the lowest tolerable value was found. In practice we did not have to change the alignment much for the output fibres. We report these values alongside the manufacturer specifications in table 2.1.

Output #.	Quoted PER	Measured PER
1:2 #1	21.5	25.5
1:2 #2	18.5	25.5
1:3 #1	21.7	22.0
1:3 #2	20.2	24.9
1:3 #3	22.1	19.2

TABLE 2.1: Polarisation extinction ratio (linear:rest) of the fused fibre couplers used in the calibration of the 2D and 2D+ MOTs. The measured value is the final PER in use after optimisation.

2.3 Performance of the 2D+ MOT

We used a 3D MOT load to characterise the performance of the 2D+ MOT. The 3D MOT was made 370 mm downstream in the secondary chamber, as in figure 2.2. The 3D MOT is loaded for 1 second and the number of atoms, N, arriving in the 3D MOT is counted via fluorescence imaging with a photodiode (Thorlabs DET36A/M). The detected fluorescence signal over time describes the 3D MOT loading curve with flux, R, from the 2D MOT [82]

$$N(t) = R\tau_{trap}\left(1 - \exp^{-t/\tau_{trap}}\right), \tag{2.9}$$

where τ_{trap} is the trap lifetime (s) and R the flux arriving from the 2D+ MOT (atoms s^{-1}). When $t \ll \tau_{trap}$ then the linear term dominates and we equate R with the slope of the loading curve.

The trapping and cooling beams for the 3D MOT are formed from another fibre splitter, this time with one input and three outputs. Both fibre-splitters are roughly 50% power-efficient. Around 80 mW is incident on the 3D fibre, corresponding to roughly 14 mW at each of the fibre outputs. Each output is then collimated and expanded to a $1/e^2$ waist of 19 mm and retro-reflected to form the six beams required for trapping. A magnetic field gradient of 16.8

G cm^{-1} for the 3D MOT was generated with a separate set of coils. For the performance analysis in this chapter, the full 3D coil (and former) as shown in figure 2.2 had not been implemented yet. Instead, for initial testing we used an 80 turn, $r = 30\,\text{mm}$, 60 mm separation "test-coil" which we ran at 3.5 A to provide the required field gradient.

2.3.1 Performance and analysis

The 2D MOT parameters (beam power, alignment, etc) are optimised by observing the 1 s loading time into the 3D MOT without the plus beam on. Loading for this amount of time allows us to directly measure R, corresponding to the number of atoms in the trap after a 1 s load, N_{1s}.

We note the two parameters with the greatest effect on flux are the 2D beam power and the background vapour pressure (see figure 2.4). Our total power is limited to 60 mW over the whole 2D system and 80 mW over the 3D. We suggest that additional power in the 2D MOT will increase the flux further, as we see R increases linearly with beam power, with no sign of plateauing. In the future, this could be confirmed with access to more laser power than was currently available. As it stands we can load $> 5 \times 10^9$ atoms in 15 s of flux at a rate of $R = 1.6 \times 10^8\,\text{s}^{-1}$. We measure the temperature of the cloud in the 3D MOT to be 500 µK via time of flight flourescence images [103, 104]. However, optimisation for lower MOT temperatures was not under-taken with the test coil arrangment. We envisage an optical molasses stage after trapping atoms will cool sufficiently in order to be then transferred into a magnetic trap like we have done previously - see references [63, 64] and section 2.4.

2.3.2 Push/Plus comparison

When measuring the 1 s load time with the push/plus beam activated we see an immediate increase in 3D MOT size corresponding to an increase of flux of around an order of magnitude when compared to loading solely with the 2D MOT. The waveplate immediately after the push/plus beam telescope in figure 2.5 adjusts the polarisation of the push/plus beam, and was used to observe the effect of the push/plus beam polarisation on the 2D+ MOT flux. In theory, since there is no magnetic field gradient along this direction (in x, see figure 2.6) then the system should be invariant to the polarisation of the beam. For atoms to accelerate efficiently, linear polarisation should be chosen in order that atoms are pushed without becoming optically pumped. We consider the push beam to be the central core of the plus beam that does not undergo retro-reflection. An aperture before the waveplate allows us to switch between the push and plus beams without changing beam intensity.

The polarisation of the beam exiting the fibre is linearly polarised. Polarisation is measured with a Schäfter+Kirchhoff polarimeter (SK010PA-NIR), which displays the orientation of polarisation as a point on the Poincaré sphere[2], along with the linear PER - the ratio of linear polarisation to all other polarisations. With a $\lambda/2$ waveplate the orientation of linear polarisation is rotated in the (transverse) plane of the beam. A rotation of the waveplate by θ corresponds to a rotation of the polarisation by 2θ, hence $\theta = 45°$ will change vertical linear (V) into horizontal linear (H). The effect of the push/plus beam polarisation angle on atom number is plotted in figure 2.7. The top graph, contains data pertaining to the push and plus beam over a waveplate rotation of 180°. A zoom in on the feature at 90° is shown on the bottom graph, corresponding to the shaded area. A difference in flux of a factor of two between V and H polarisation is shown for the plus beam (black circles, figure 2.7 top), where the change between the two is linear (figure 2.7 bottom). For the sole push beam (blue crosses, 2.7 top) there is no noticeable change in flux with waveplate rotation.

The variation of flux with the plus beam is not expected, as naïvely one would expect the *orientation* of linear polarisation to not have an impact. One consideration was the two mirrors involved in the retro-reflection. Upon reflection a phase difference between the V and H polarisation components accrues (π for metallic mirrors and variable for dielectrics) and hence the reflected beam might not have the identical polarisation if it was not purely V or H to begin with. Measuring the return (plus) beam polarisation we find that pure V or H linear polarisation returns as such. At rotations $+(-)10°$ from horizontal, the return beam polarisation is fully circular left (right). The linear change in flux from V to H (figure 2.7 b) suggests this little circularity in the return beam plays little to no role in the performance of the plus beam.

With a quarter waveplate ($\lambda/4$) exchanged for the $\lambda/2$ a different effect is observed. In figure 2.8 we plot the loaded atom number after 1 s against waveplate angle, along with the linear PER. A high PER here means a high degree of linear polarisation, where 0 dB PER corresponds to fully circular

---

[2] The Poincaré sphere displays polarisation as a point on a sphere where the poles correspond to fully horizontal and vertical polarisation.

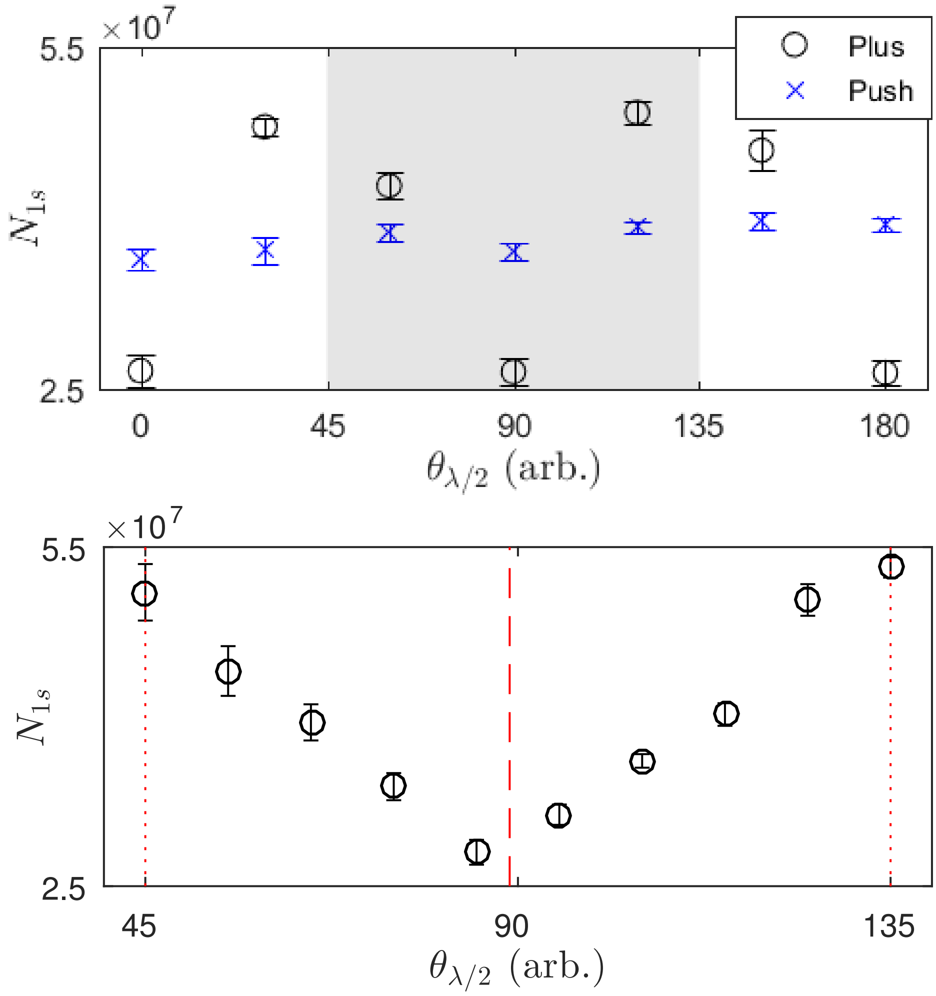

FIGURE 2.7: Number of atoms in the 3D MOT after 1 s of loading as a function of waveplate angle, corresponding to a linear polarisation rotation. The black circles denote the retro-reflected plus beam and the blue crosses the apertured push beam. (Top) Push beam performance is observably unaffected by polarisation, whilst the plus beam sees a factor of two increase in flux changing from H to V polarisation, corresponding to a 45° rotation. (Bottom) Number of atoms loaded in 1 s with the plus beam over the region denoted by the grey shaded area, showing the linear change between V (dotted line) and H (dashed line) polarisation.

polarisation. The output from the fibre is linear at its output, so rotating a quarter waveplate changes it between fully linear and fully circular with a 45° rotation. The load rate shows a higher sensitivity to the PER of the push beam, as shown in figure 2.8 a). At the point where the beam is most linear, the 1 s load peaks at 4.0×10^7 atoms. By making the beam less linear, the flux decreases. the handedness of the circular polarisation, denoted in figure 2.8 as 160° for right-handed and 240° for left-handed, also effects the load rate by about 25%.

In figure 2.8 b), the effect of load rate on plus beam polarisation linearity is plotted (blue circles) as well as the PER of the input (or upstream) and retro-reflected beam. A higher maximum atom number was obtained using the plus beam, as compared to the push, with a $N_{1s} = 4.4 \times 10^7$. This occurs where the two beams are slightly, and roughly equally elliptical. The handedness of the beams at this angle is circular right - which has already been established to perform better than circular left where the worst performance is also recorded (at 260°). The best performance was observed for (vertical) linear polarisation, as we expected given the reasons we introduced in section 2.2.4.

2.3.3 Plus beam polarisation effect mechanism

The common simple picture in magneto-optical trapping sees the magnetic field aligned with the direction of the atom's velocity, so that the polarisation is always perpendicular to the magnetic field. In these cases the force from a single beam is given by

$$F_{MOT} \propto \frac{I_{beam}/I_{sat}}{1 + \frac{I_{tot}}{I_{sat}} + \frac{4}{\Gamma^2}\left(\Delta + \vec{k}.\vec{v} + m_F \frac{\mu_B g_F}{\hbar}|B|\right)^2}, \tag{2.10}$$

where I_{beam} and I_{tot} denote the total beam and MOT optical intensities, $\vec{k}$ the wavevector and $\vec{v}$ the velcoity of the atom, m_F the Zeeman sublevel and g_F the Landé g factor. The principle of the MOT relies on this force having a null in the centre in both position (trapping) and velocity (cooling) [105]. Velocity selectivity is achieved via detuning (i.e. $\Delta \pm \vec{k}.\vec{v}$) but trapping requires circular polarisation to play a part, allowing directional sensitivity [105, 106]. Here, however, the polarisation is always orthogonal and selection rules permit the excitation of sigma (σ) transitions only, where $\Delta m_F = \pm 1$, for magnetic fields transverse to the polarisation.

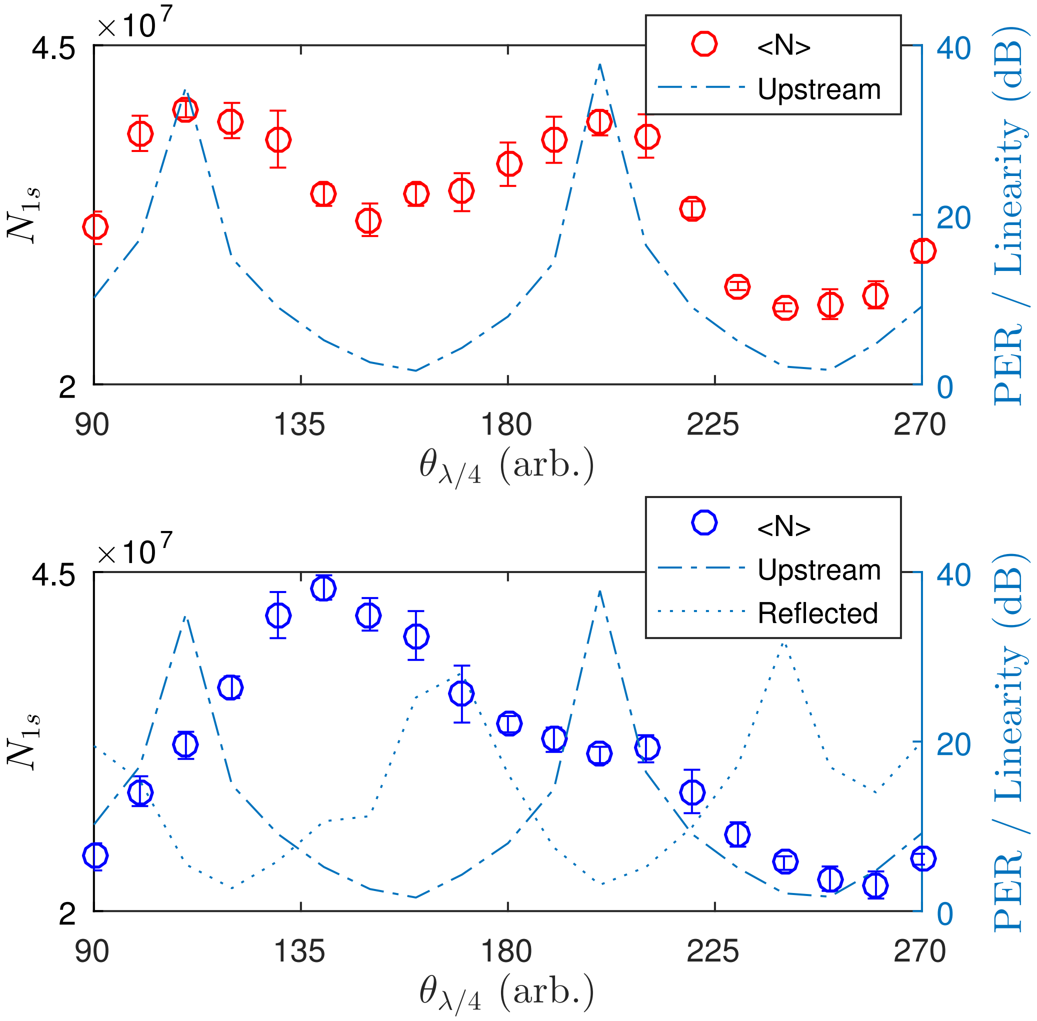

FIGURE 2.8: Number of atoms in the 3D MOT after 1 s of loading as a function of waveplate angle for a $\lambda/4$ waveplate, changing from linear to circular polarisation, as denoted by the PER (lines, right axis). Load rate for the push beam (top, red circles) and plus beam (bottom, blue circles) are plotted with corresponding PER (Blue lines) of the original (dashed) and reflected (dotted) beams. For the push beam, highest flux occurs where the beam has a high degree of linear polarisation. The plus beam show more complicated effects, peaking where the beams have similar right-handed circularity. Both cases do not perform as well as in the fully linear regime in figure 2.7.

Our glass cell is made of standard NBK7 (Schott) glass which has a refractive index of 1.5112 for 780 nm light and is not anti reflection coated. We lose roughly 7% optical power due to reflections on a single pass through through the 2.5 mm cell wall. The retro-reflected MOT beams have to go through the cell wall twice. We ignore absorpative losses to due the quarter waveplate and dielectric mirror as they are anti-reflection coated (Thorlabs B coating). This total loss of 14% beam power is quite significant and weakens the confinement strength along the return direction (in positive y and negative z of figure 2.5). The location of the force null then changes, due to this imbalance, to a location where the magnetic field is not zero in the transverse direction.

With a transverse magnetic field component, the angle of the polarisation of the plus/push beam becomes important. We are now able to align the laser E field with that of the magnetic field, exciting π transitions ($\Delta m_F = 0$). One consequence of this change is that the Clebsch-Gordon coefficients are drastically different for σ and π transitions, where σ transitions in favourable conditions can cycle much faster than π. The saturation intensity is also less for σ [107]. As a consequence more 'pushing' can be done with a σ polarised beam. Thus aligning the polarisation vector with the magnetic field lowers the flux.

When the beam is V polarised, it must therefore be perpendicular to the local B field, and when H polarised it is parallel. The direction of the field may even be 'sensed' by the ratio of load rates with circular right vs circular left polarisation in the $\lambda/4$ scheme: more right suggesting the field is in the $-z$ direction, which we expect given the retro-mirrors lie on this side of the chamber. The $\lambda/4$ plus case must be analysed with more care, as the return beam plays an impact, as its handedness is inverted upon retro-reflection.

2.4 Route to BEC - in brief

Bose-Einstein condensation as a phenomenon is achieved as *bosonic* particles reach a critical temperature and density where the ground state becomes macroscopically occupied. Here the single-particle wavefunctions overlap significantly enough for the ensemble to described using only a single wavefunction. The Nobel Prize in 2001 was won for the experimental realisation of this elusive state of matter, jointly between Cornell and Wieman [108] and Ketterle [109]. More comprehensive descriptions of the state and its properties can be found at the following references [68, 69, 71, 74, 110, 111].

A BEC is formed by the atoms' wavelength growing to a certain size that they begin to overlap significantly. Condensation is therefore the point at which the atomic separation approaches the de Broglie wavelength, λ_{db}. The atomic wavelength is related to the atomic temperature, T, by the following,

$$\lambda_{\mathrm{db}} = \frac{\hbar}{\sqrt{2\pi m k_B T}}, \tag{2.11}$$

where k_B is the Boltzmann constant and m the atomic mass. A more intuitive quantity by which to measure the degree of overlap is the phase space density, PSD,

$$\mathrm{PSD} = n\lambda_{\mathrm{db}}^3, \tag{2.12}$$

which is a dimensionless quantity which combines the de Broglie wavelength with the number density, n. The critical value of PSD for condensation changes with the shape of the trapping potential, but for a 3D harmonic trap, such as that found in a focussed Gaussian beam trap, this is around $\mathrm{PSD} = 1.2$ [112]. From equation 2.12 it is evident therefore to produce a BEC we should minimise temperature and maximise density.

The MOT is only one such constituent part of the machine typically used to produce BEC. The 2D/3D setup, as described with the caveats in section 2.2, is generally used for experiments that require rapid cycle times and a low vacuum pressure. At the MOT, the PSD is roughly $\approx 1 \times 10^{-8}$, so we must cool and compress the ensemble further to reach degeneracy. Cooling is done by evaporative cooling, and compression is done by loading the atoms into tighter traps - gradually such that losses due to poor mode matching between traps are minimal.

We shall briefly detail the route taken by our previous experimental apparatus, which we will eventually construct the freefall BEC interferometer in. More specific detail of the apparatus construction is covered in the theses of Mackellar [64], Robertson [63] and Dinkelaker [66]. Our approach is a magnetic/optical hybrid [63, 113]. From the 3D MOT, loading into a magnetic trap which we then use to transport the cloud across the chamber, during which we begin performing radio-frequency (RF) evaporation [68]. We have roughly 7×10^8 atoms with a PSD of $\approx 4 \times 10^{-6}$, before RF evaporation in the magnetic trap, and 7×10^7 atoms with a PSD of $\approx 1.5 \times 10^{-3}$ after. The magnetic trap is then lowered into a crossed-dipole trap, in which the trap depth is reduced and the cloud evaporated to degeneracy. The entire process takes around 10 seconds to perform; including 3 s of RF evaporation and 5.6 s of dipole evaporation. In total, one experimental cycle time is approximately 40 s long, when we include the 30 s of MOT loading. This time will be significantly reduced with the adoption of the $2D^+$ MOT described above in section 2.2. There are multiple ways one might additionally speed this up for other experiments, as production of BEC can be made very fast in chip-trap setups [114, 115], for example.

This particular system we are using has been operated and iterated upon for nearly a decade, showing a clear robustness in operation, despite running out of rubidium twice. All experimental controls of note are configurable and automated via `LabVIEW`, including our pulse parameters for interferometry (see chapter 3), as it had been configured for use in magnetic gradiometery [116]. Introducing additional devices, such as our peizoelectric stack in chapter 4 is as simple as daisy-chaining the device into the trigger pulse-train, with timing offsets we know and can control and account for. From day-to-day operation our biggest maintenance issue is our fibre-alignment, as the majority of our preparatory optics are delivered to the chamber via fibre-couplers. The use of fibres allows for changes to be made to the preparatry optics without affecting alignment on the chamber, at the price of fibre-injection losses (although with careful mode-matching these losses can be made minimal [117]).

The hybrid quadrupole magnetic trap has a maximum magnetic gradient of 200 G/cm when supplied with 165 A current. The coils themselves are made of hollow copper pipe, 1 mm inside diameter and 1 mm thick, such that the cooling water is delivered directly to the coils. Over a days worth of experiments (running continuously as above) the coil temperatures never reach above 30 °C.

The crossed dipole trap is formed from a 1070 nm laser (IPG Yb fibre) which can deliver up to 10 W of light at the cell, intensity controlled by an AOM at the laser output. The beam is split via a polarising beam splitter, then crossed at 128° to make a crossed dipole trap [85]. Typically the trap is loaded initially with 3.2 W optical power/laser light and is decreased to around 220 mW by the end of the evaporation stage. We measure the final trap frequencies to be 29.1 by 48.6 Hz in the x and z directions (via observation of sloshing-mode oscillation [68]), at the point of formation of the BEC. Repeated measurements at other final intensities allow us to infer a scaling of $f_x = 0.60 * P^{0.46}, f_z = 141 * P^{0.54}$ in the x and z, as a function of final power, P. This deviates slightly from the expected $f_{x,z} \propto \sqrt{P}$ scaling, probably due to anharmonicity in the trap and gravity.

From this point onwards the experiment differs from the work mentioned previously, in order to accommodate the interferometry in freefall. The same MOT and hybrid trap is used to prepare a Bose-Einstein condensate, but the interferometry setup has been modified slightly. The interferometry beam is derived from the same source, but has been expanded in diameter (collimated, not focussed at the atoms) and strikes the chamber from a different angle in order to be retro-reflected. Details can be found in the following section.

Part II

Interferometry

Chapter 3

Preparatory optics for a BEC Interferometer

In this chapter we consider the constituent parts of a freefall BEC interferometer, namely the characterisations of the splitting pulses used, their modifications from previous [116] characterisations and how changing the geometry affects the experiment and the phase accumulation.

We have already introduced the principle of interferometry in chapter 1. In this chapter we discuss the technical means to create an interferometer with a BEC, focusing on the Kapitza-Dirac method used to form matter-wave beamsplitters for our BEC in section 3.1. We will first describe the mechanism and formalism behind the coherent process, before detailing our pulse sequence and performance, including the reflection.

We wish to perform a rotation measurement perpendicular to the earth's gravity, which is accomplished by dropping the BEC under gravity. The modifications to the apparatus required to achieve this are described in section 3.2. As the condensate moves, however, it will also move out of the interferometry beam. It is then important to build up a picture of where the atom is with respect to the beam and what local intensity the beam imparts to the atom at that position. We describe our calibration of this in section 3.3. Finally we introduce our calibration under gravity, allowing us to know the power each pulse is required to be to accomplish effective splitting/recombination, alongside a measure of asymmetry, showing our sensitivity to alignment with the gravitational axis in section 3.4.

3.1 Splitting pulses in Interferometry

Any atomic interferometer is dependent on a series of operations in order to split, reflect, and re-combine the atomic wavefunction. There are many ways to achieve this. Given our BEC with its narrow width momentum distribution, we can choose a technique to take advantage of this and address the entire ensemble with a splitting pulse - namely the Kapitza-Dirac pulse. We will see with a composite, three-stage pulse it is possible to achieve momentum transfer to the cloud with great efficiency.

3.1.1 Common Techniques: Intro

In interferometry, by comparing the relative phase between two different paths travelled by a single wave source we probe the difference between those two paths. To this end, one requires a mechanism by which the source can be split coherently into the two parts. To split a classical oscillating electric field, i.e. light, we use beam splitting devices which rely on a material change - a change to the index of refraction. For atomic systems there are analogous beam splitters.

With light we consider the electric field along the whole path of the interferometer, splitting and recombining along the way, so similarly we need to put the atomic ensemble into a superposition of path 1 and 2. Put another way, we need a method to coherently separate and recombine the cloud somehow. This separation is usually physically in space via a change in momentum. For instance we may split an atomic cloud in such a way that one half will travel upwards, whilst another will stay “stationary”, in the concerned axis. This is illustrated in figure 3.1. The waves then need to be recombined in some manner. ’Reflection’ is therefore a requisite of any interferometer dealing in momentum separated paths. Finally there must be another beam splitter to recombine the packets, which then *interfere* by an amount related to the phase difference. The outputs of an atom interferometer are generally the atomic populations of the two momentum states. If no phase is accrued between the two paths, the waves will remain in the same manner as they entered the interferometer (e.g. at rest), but any phase change will exhibit itself as a presence in the “second” channel. This forms a rudimentary atomic Mach-Zehnder interferometer, as illustrated in the figure.

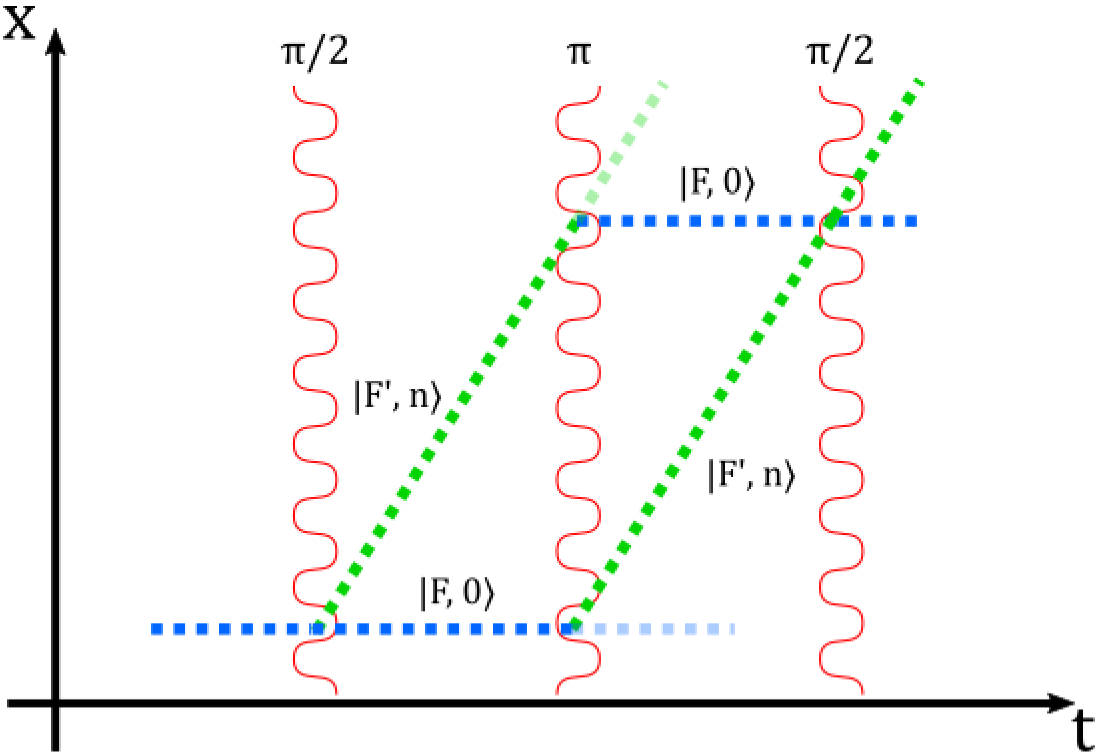

FIGURE 3.1: An example of an atomic Mach-Zehner interferometer. Three pulses of light (red) act to split, reflect and recombine an atomic ensemble. In this particular example, common to many modern experiments, an ensemble prepared in some ground state, $|F, 0\rangle$ (dashed blue line), is split by applying a resonant $(\pi/2)$-pulse, transferring half the population to the $|F\prime, n\rangle$ state (green dashed line). The difference in the state populations after the final pulse is related to the phase difference accrued.

This is most often implemented by two-photon Raman transitions [118, 119]. The Raman process is a resonant two-photon process, far-detuned from the single-photon transition which has the result of minimising spontaneous emission. Two low-lying energy states are coupled resonantly with a pair of beams, one detuned from the other to make an effective "moving lattice". This lattice movement allows for the transferral of momentum - $2\hbar k_\lambda$, where k_λ is the lattice photon wavenumber [14]. Splitters are then generated with $\pi/2$ pulses and reflections are similarly achieved by a π pulse. Gustavsen et al. used this technique in their formative atomic Sagnac interferometer [38, 39], and indeed many modern Sagnac interferometers also utilise this method of splitting [40, 120, 121]. However inhomogeneities in the system erode the performance of these pulses, be it magnetic, in intensity or most notably in atomic velocity [122]. It is difficult to make these pulses 100% efficient in practice, hence the tails (lighter lines) after each pulse in figure 3.1. Methods to improve Raman pulse efficiency are an active area of research, including optimised shaped pulses [123, 124].

Decreasing the average atomic velocity is another factor in improving pulse efficiency, with sub-recoil clouds being made for use in interferometric systems [125]. For splitting a BEC we can make use of the already narrow momentum distribution to address the entire cloud with a tailored pulse. These pulses are described in the next section.

3.1.2 Diffraction from a Light-Grating: Bragg and Kapitza-Dirac Scattering

Bragg and Kaptiza-Dirac (KD) scattering are interesting processes to consider for interferometry as they leave the internal state of the atom unchanged. Atoms are usually multi-level, so this scattering method uses interactions that do not allow higher-lying internal energy states to be populated.

In the Bragg / KD case, coherent scatter is achieved by diffraction from a lattice potential in the light field. An illustration of the two cases are shown in figure 3.2. We understand how to generate interfering potentials with light (same frequency, polarisation and spatial overlap), and a simple retro-reflected beam will interfere into a sinusoidally varying potential - a lattice. The process then involves a pair of stimulated absorption and emission events.

Bragg scatter is much like its analogue in the x-ray crystallographic world. At a specific angle of incidence of an x-ray at the crystal axis, the reflected wavefronts from the crystal lattice constructively interfere. In a similar fashion, atoms will diffract from a lattice if travelling at the Bragg angle with respect to the wavenumber of the optical lattice, k. Transfer between $|\pm 2n\hbar k\rangle$ is therefore possible, where n denotes the number of photon pairs we coherently scatter [34]. This was first shown for atomic beams by Martin et al. [32, 126]. For stationary atoms a similar situation occurs when the difference in frequency between the two beams is shifted such that the lattice moves with corresponding velocity, $n\hbar k/m$, to the momentum transfer. Large momentum transfer using the Bragg technique is possible by scattering into higher n states, but this requires prodigiously large beam powers [127].

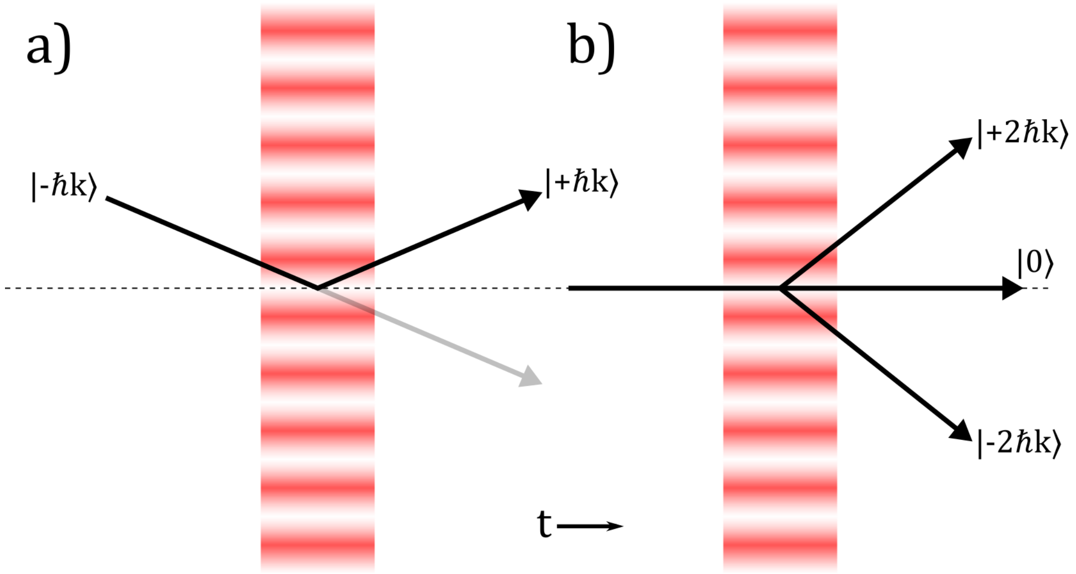

FIGURE 3.2: Illustration of the cases for off-resonant scatter from a photonic grating - a standing wave of light (red regions) is generated from a single-frequency source. a) Bragg scatter case, where at a specific angle to the lattice normal atoms will scatter $2\hbar k$ momentum into the symmetric momentum state. b) General Kapitza-Dirac scattering case, where any atom (stationary with respect to the lattice) will scatter into symmetric ± momentum states as the grating is pulsed on. Scatter into higher $|\pm 2n\hbar k\rangle$ states, where n is an integer, is possible with this technique.

Kapitza-Dirac scattering is the somewhat more general case [128]. Scatter from a lattice can be achieved without the stringent need for "angle" dependency, but we lose some control over the specific momentum transfer occurring. The main caveat is that in KD scatter the lattice vector does not discriminate with regards to scattering forwards or back along the lattice k. Hence we have equal populations of ± after one event. This is sketched in figure 3.3. It is this KD pulse that we use to split our condensate, which we cover in more detail in the next section.

3.1.3 Kapitza-Dirac pulses

Kapitza and Dirac in 1933 first suggested that an electron beam may be deflected by a standing wave of light [129]. To observe the effect however required the invention of the laser in order to observe a "useful" beam splitter. Kapitza and Dirac's theory is more general and applies to not only electrons, but also matter waves [128]. The first observations of Kapitza-Dirac scatter of

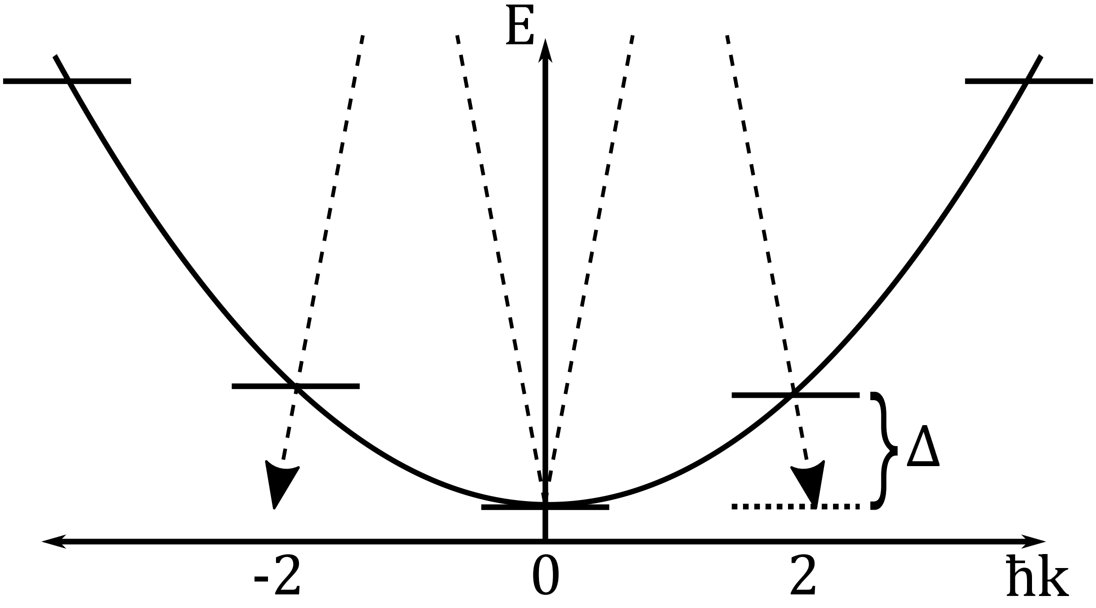

FIGURE 3.3: Energy-Momentum diagram of the various plane-wave momentum states available to an atom at rest. The parabola denotes the Energy-momentum relationship $E \propto k^2$, and the various states denote the eigenstates of the 2-photon absorption events. Given the distribution is symmetric between positive and negative momentum states, one scatter equally populates the ± states. Using 2 identical photons introduces a detuning, Δ equal to the energy of that state.

atoms by a standing wave produced by laser light were in 1986 by Gould et al. [31]. A beam of sodium atoms passing through such a light-field was deflected by discrete amounts of $2\hbar k$ momentum.

This procedure follows that of [130], which includes a generalisation to pulses outside the Raman-Nath criteria where the atom-light interaction time is small, i.e. an effective thin-lens approximation for atoms [131]. We bring the ansatz,

$$|\psi\rangle = \sum_n C_n\left(t\right)|\phi_n\rangle, \qquad |\phi_n\rangle = e^{i2nkz}, \tag{3.1}$$

where we define the atomic wavefunction, ψ, in terms of a series of plane waves, ϕ_n, in momentum space. Here, n denotes the nth plane-wave harmonic with $2\hbar k$ separation, starting with $n = 1$. It is then a matter of putting this into the Schrödinger equation. The Hamiltonian,

$$\hat{H} = \frac{\hbar}{2m}\frac{\partial^2}{\partial z^2} + V_0 \cos^2\left(kz\right), \tag{3.2}$$

includes the common kinetic operator, denoted by the double derivative, and the potential term from the crossed-beam lattice, or standing wave, in the form of a cosine squared. Note we are neglecting atomic interactions in this picture. The Schrödinger equation then becomes,

$$i\hbar|\dot{\psi}\rangle = i\hbar\sum_n \dot{C}_n|\phi_n\rangle = \frac{\hbar}{2m}\sum_n C_n\frac{\partial^2}{\partial z^2}|\phi_n\rangle + V_0\sum_n C_n\cos^2(kz)\,|\phi_n\rangle, \tag{3.3}$$

where note we have ignored the existence of (excited) internal states, as in this configuration we should have very large detuning values such that we are far from excitation through this channel - i.e. we presume the two photon coherent process dominates. The kinetic term drops out of the spatial derivatives, whilst the cosine squared acts as a would-be ladder operator, given $\cos^2(kz) = \frac{1}{4}\left(e^{i2kz} + e^{-i2kz} + 2\right)$, changing the n-value of the harmonic as follows,

$$i\sum_n \dot{C}_n|\phi_n\rangle = \sum_n \frac{E_n}{\hbar}C_n|\phi_n\rangle + \frac{V_0}{\hbar}\sum_n \frac{C_n}{4}\left(2|\phi_n\rangle + |\phi_{n+1}\rangle + |\phi_{n-1}\rangle\right), \tag{3.4}$$

where we introduce the 2n-recoil energy, $E_n = (2n\hbar k)^2/2m$. When we consider the populations of each nth state, $P_n = \langle\phi_n|\psi\rangle$, a series of coupled equations emerge. Multiplying through by $\langle\phi_n|$ and removing the orthogonal terms leaves us with, for the nth state,

$$\dot{C}_n = -i\left[\frac{E_n}{\hbar}C_n + \frac{V_0}{4\hbar}\left(C_{n+1} + 2C_n + C_{n-1}\right)\right]. \tag{3.5}$$

We solve equation 3.5 numerically and plot values of the population P_n for ^{87}Rb in Figure 3.4 with orders up to $n = 4$ in order to better understand the impact the pulses have on our momentum distributions. In this simulation we assume all atoms start in the ground state ($|0\rangle$), and we apply a pulse of varying length and a height of 10.35 E_r, where E_r denotes the lattice 1-photon recoil energy, $E_r = (\hbar k)^2/2m$. We have omitted the higher momentum states ($n > 2$), as in practice we rarely see population in momentum states above $|\pm 4\hbar k\rangle$ for the pulses we use ($< 40\,\mu$s). In this simulation they have negligible population. Notice that we do not see a complete "flop" like we would in a two-level system - this is due to the effective detuning, Δ, as seen in figure 3.3.

To fulfil the Raman-Nath criteria then the interaction time must be much smaller than the time it takes an atom to see a full oscillation within the trap - i.e. that $\tau > 1/\omega_r$, where ω_r is the recoil angular frequency for the lattice beam.

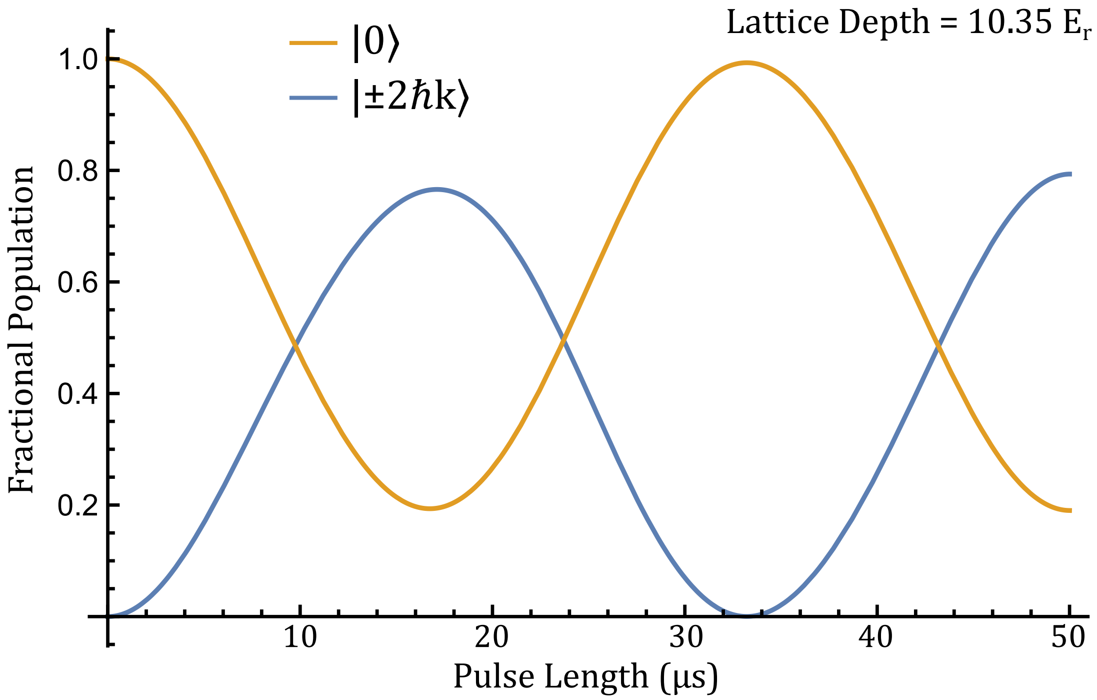

FIGURE 3.4: Numerical simulation of equation 3.5 up to $n = 4$ for pulses of various length. For clarity, only the $n = 0$ and combined $n = \pm 2$ modes are displayed, as other orders contribute $< 1\%$.

In the Raman-Nath regime we effectively ignore the Kinetic energy of the particle, removing the self energy part proportional to E_n in equation 3.5, and are left with the "ladder" operations. The resulting simultaneous equations have a solution in the form of a Bessel function,

$$C_n(t) = (-i)^n e^{-iV_0 t/2\hbar} J_n(V_0 t/2\hbar), \tag{3.6}$$

and thus the population can be expressed,

$$P_n = |C_n|^2 = J_n^2(V_0 t/2\hbar), \tag{3.7}$$

as an analytic solution to equation 3.5, when the Raman-Nath criteria is satisfied, where J_n denotes the nth Bessel function of the first kind [132]. The Raman-Nath criteria, however, is only valid for short interaction times [131]. Comparing with longer pulses of higher energy, as seen in figure 3.4, we see that this "approximation" in terms of Bessel functions is no longer valid.

It is important for us to consider pulses outside the Raman-Nath regime, as our composite pulse scheme (detailed below in section 3.1.4), utilises much longer pulses. In the case of our splitting beam, for example, the Raman-Nath criteria is roughly $1/\omega_r \approx 4\,\mu s$. A single pulse is also unable to invert the fractional population - due to the effective detuning and the presence of higher lying momentum states that can be coupled into. We can, however, design effective splitting pulses by using a pulse train, or a composite pulse, with several heights and lengths.

3.1.4 Composite Pulse Description

Bragg scattering was offered as a method of obtaining 100% effective coherent splits of atomic population [133] as with careful tuning of the atomic lattice one can reach a resonance condition, allowing for an effective time-independence to the interaction time length. Pulses (or atom traversal) could be done over 100s of µs. The moving lattice requires two beams with independent frequency control to generate [32, 134, 135].

An alternate solution to achieve complete splitting is to overcome the inherit detuning in the KD configuration. A straight two-photon absorption is not resonant from one momentum state to another using a stationary lattice (where the two beams have equal frequencies), as evident in figure 3.3 where an effective detuning Δ will always persist. However, we can circumvent this by utilising a composite pulse, as suggested by Wu et al. [136], which we have implemented in references [64, 116].

The essence of the technique is to use multiple pulses. Wu et al. [136] developed the scheme of two separated pulses, which was demonstrated in the work of Hughes et al. [58, 137] who then introduced a small amount of light into the separation time as a means of coupling the two pulses, boosting the fidelity of the transfer to 99.9933 % [137]. This “triple pulse” then effectively gives us parameters to vary such that we can tune the Rabi-oscillations of the various momentum state populations. We can make a situation where all state populations are at the bottom of their oscillation save the one we wish to populate. To computationally verify this we can make V_0 in equation 3.5 time dependent, $V_0(t)$, thus letting the pulse height change with the time.

As we are using a red-detuned, retro-reflected beam (see section 3.2 below), we use the same parameters as in [137], which is shown on figure 3.5. The first and last parts of the pulse are 6.06 recoil energy, E_r in height and last, $T_1 = 21.68\,\mu s$, whilst the middle has a height of $0.52\,E_r$ and lasts $T_2 = 36.44\,\mu s$.

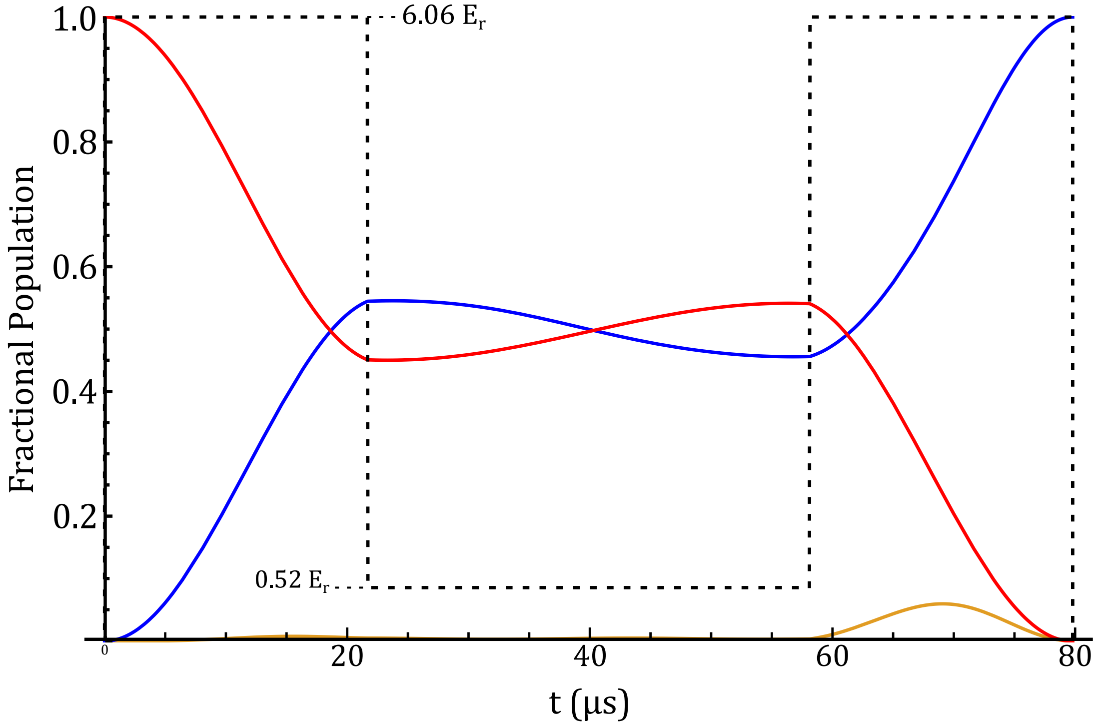

FIGURE 3.5: Our triple pulse scheme to achieve complete transferral of the $|0\hbar k\rangle$ atomic population into the symmetric $|\pm 2\hbar k\rangle$ state. Shown are the populations, $|C_n|^2$, of the ground $|0\hbar k\rangle$ state (red) and the (summed) symmetric states $|\pm 2\hbar k\rangle$ (blue) and $|\pm 4\hbar k\rangle$ (yellow) states. Full state transferral with a single stationary lattice pulse is not possible, but by splitting the pulse into three sections, we can account for this by allowing the population to "settle" in the time between. In practice we find leaving the light on in-between, facilitates better transferral.

3.1.5 Reflection

To reflect the atoms we need to address the transition from forward to reverse momentum states, and vice versa. We achieve this with a Blackman pulse [52], which has a finite envelope that goes to 0 at the wings. The Blackman shape reportedly suppresses high frequency artifacts, when compared e.g. with a rectangular pulse, resulting in a more efficient transfer [63, 138]. Finding the optimum pulse is a matter of letting, $V_0(t)$, in the simulation above vary like a Blackman pulse, changing the starting population to maximum in one of the $|\pm 2\hbar k\rangle$ states, and then varying pulse height and length, T, to maximise for population transfer ($+ \leftrightarrow -$). We calculate a peak transfer (of $\approx 100\%$) for a pulse with a height of 12.2 E_r and pulse length $T = 136\,\mu s$.

3.2 Apparatus

Here we shall detail some of the practical aspects of producing the splitting beam with pulse control detailed so far. This is described previously in the work of Robertson [63] and Mackellar [64], but any major changes since those works have been detailed below. This mostly pertains to the adjustment and spatial broadening of the KD beam, as well as the new calibration for beam power. This was done so that atoms falling under gravity would still interact with the KD beam. The new KD calibration is required to allow for the Gaussian beam's spatial variation of power with position as well.

3.2.1 Beam path and control

Our interferometry beam now needs to be much larger than the previous beam, which had a 47 µm focus, in order to still affect the condensate after it has accelerated under gravity. We want to maximise the time the atoms fall, as Sagnac phase in our freefall / kite configuration scales with $\propto t^3$, but to still have enough power to perform a closing pulse. We have seen above in section 3.1.4 that our pulse needs a maximum height (for a $|0\rangle \rightarrow |2n\hbar k\rangle$ operation) of 6.06 recoils.

In figure 3.6 a) we see the experimental arrangement of the interferometry beam. The beam is prepared elsewhere on the table and fed to a periscope to bring it to the height of the vacuum chamber, where it enters the cell from the Horizontal with a 46° angle of incidence. Note that the faces of the cell the beam enter and exit are perpendicular. The mirrors highlighted are used for alignment purposes. The beam in this configuration have a $1/e^2$ diameter of roughly 1.5 mm, and can deliver up to 3.5 mW of power. This power is controlled by an AOM, whose VCO (voltage controlled oscillator) output is gated by a mixer driven with a DC signal from a control computer. Futher details of this circuit can be found in Ref. [63]. The voltage control can output from 0 V to 10 V , but our AOM system saturates with an input voltage around 600 mV. Thus a 6% stepdown box (voltage divider) is placed in the signal path. This guarantees we do not saturate the AOM with the full range of our controller.

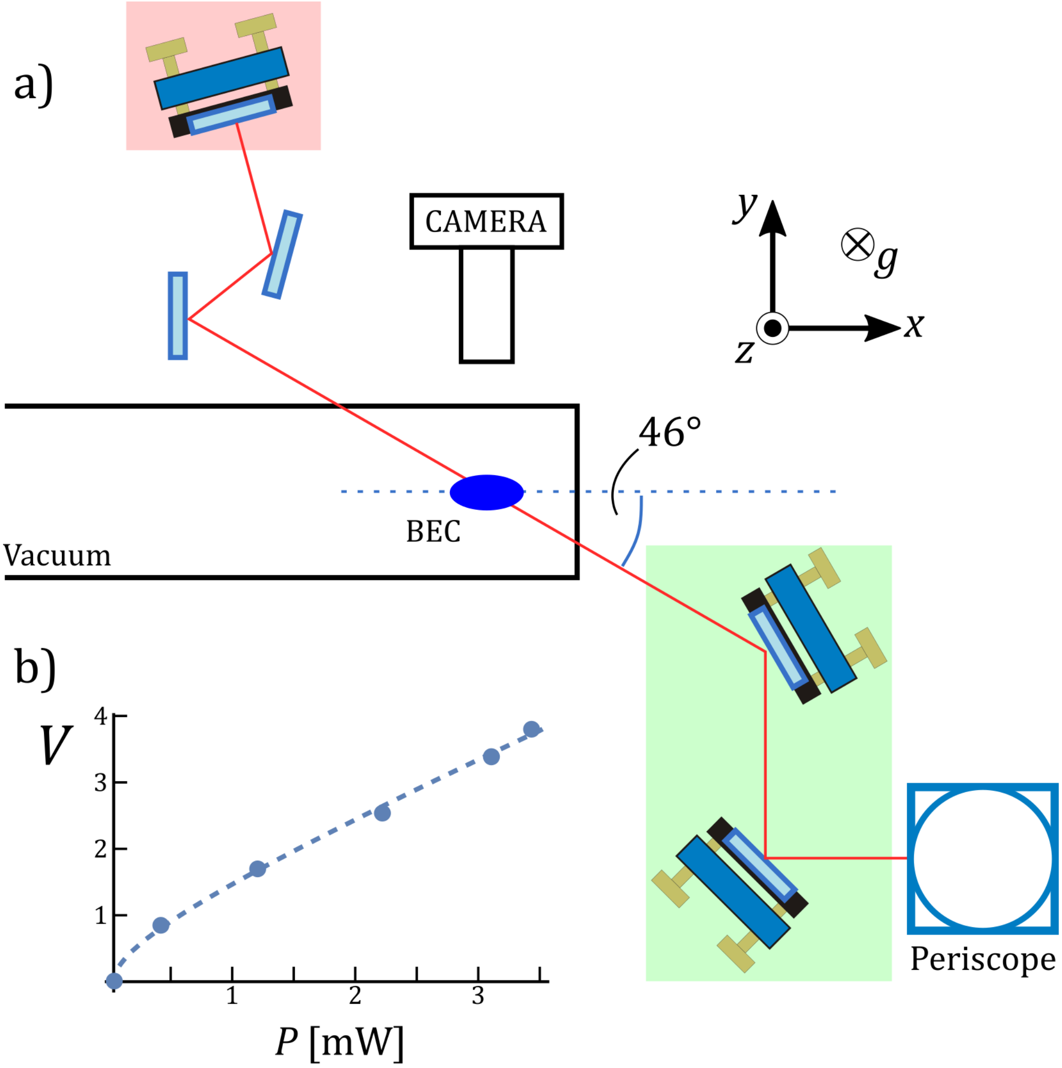

FIGURE 3.6: a) Sketch of the KD beam path through the cell and the angle with respect to the imaging camera. Gravity is in the $-z$ direction. The green / red highlighted mirrors are used for moving the angle of the beam with respect to gravity, and the retro-reflection respectively. The orientation of the camera is included to facilitate comparison with the full set-up in appendix A. b) The calibration curve for the beam power, P, as a function of the applied voltage, V.

3.2.2 Voltage to Power calibration

It is not trivial to apply a pulse with a specific energy. The natural language of our computer controller is an output voltage, which translates into an amplitude control for the AOM. By measuring the resulting beam the AOM generates we translate this into a beam power, P. The actual effect this has on the atoms, i.e. the energy which we report as an equivalent number of recoil energies, E_r, depends on a multitude of factors, more so now that we have expanded and moved our beam. Day-to-day fluctuations in laser output, misalignments from mirror sag, dirty windows, etc, will all change the power the atoms see over time with use.

Figure 3.6 b) shows the voltage to beam power calibration performed. This gave us the general shape of the curve. The power in the beam for a requested control voltage is thus worked out by the following calibration curve;

$$V = S\left(A\,P + \sqrt{\frac{B}{S}\,P + (C\,P)^2}\right), \tag{3.8}$$

with the curve parameters, A, B, C, detailed in table 3.1. The scaling factor, S, allows for a day to day calibration as the beam power fluctuates over long time periods - the x-axis scaling we require. In practice, this is usually set around $S \approx 0.5$. It is also this term that we change to normalise the beam power as the BEC traverses different spatial regions, thereby different intensities, of the beam during freefall, discussed in section 3.3.

Param.	Value
A	0.0285
B	0.0714
C	0.0283

TABLE 3.1: Curve parameters used in equation 3.8 to fit the voltage requested from the controller, V, to deliver the beam power, P specified.

We can then achieve a calibration by varying the power in the beam and plotting the resulting split populations of the BEC, and the compare with numerical simulation, as done previously [63, 64]. We can, however, achieve a calibration of the entire Gaussian beam by sampling the BEC split for a variety of *drop times*, corresponding to a different part of the beam, and fitting the numerical simulation of equation 3.5 to it, by including beam parameters, width, height and offset, in the equation. This is detailed in section 3.3.

3.3 Optimisation under gravity

The challenge facing the BEC freefall interferometer is the introduction of the beam diameter into the calculation for the power of the beam. We have seen previously (in section 3.1.4) that the split with the triple pulse can be calibrated against simulation to distribute population fully to a symmetric momentum distribution, given sufficient knowledge of the pulse height. This usually takes place at the waist of a beam, mostly because the phase front curvature of the beam is flat at this point and thus exciting varied phase across the condensate can be avoided [139, 140].

As the BEC falls however, it will cover distances around a millimetre after 14ms. Focused beams in this regime tend to be some 100 times smaller (we previously used a 47 µm beam [63, 64]), hence our beam needs to be larger to accommodate this. Wider beams necessitate higher power to maintain the same intensity, which the BEC is sensitive to. This places constraints on how far we can drop the condensate and still have enough power to recombine the packets fully. It is also important, much like the calibrations done previously, to know what intensity is actually incident on the atoms, and map this to a pulse height to make use of the calculation in 3.1.3. The problem is outlined in figure 3.7 - where the power in the beam now has to match where in the beam spatially the condensate is at that particular moment we apply the interferometry pulse. The challenge then is to work out a map of the lattice height as a function of drop time, and use this calibrate the interferometry pulses as the BEC traverses the beam.

3.3.1 Calibration of freefall with time

We outline the problem in 3.8 a). The interferometry beam has a Gaussian profile and as the atoms accelerate under gravity (z-axis) they will move further away from the beam centre at $z = 0$, with peak intensity I_0. We only control the time of the drop, which we must associate with a position. This is done by imaging the cloud for different drop times and measuring the position. The

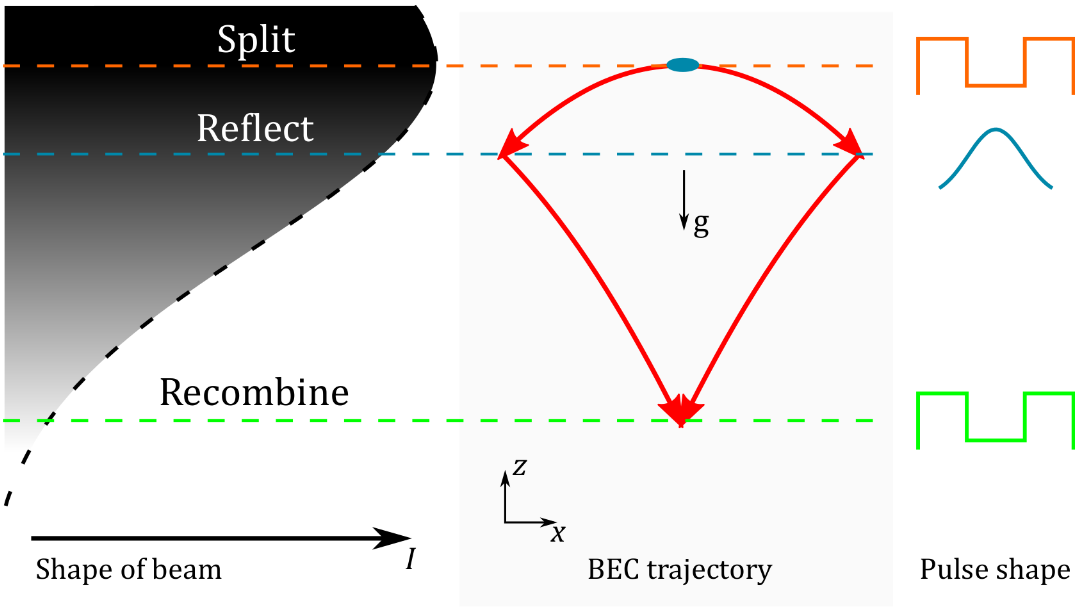

FIGURE 3.7: The problem of performing interferometry in freefall where as the BEC falls, the local intensity of the beam that it experiences changes. Knowing the location of the BEC in space is crucial therefore to understand how much power is required to produce the calibrated pulses discussed in section 3.1.4. An illustration of the beam (arb. scale) is shown on the left, reflecting the relative changes in local intensity from pulse to pulse. The kite-shaped area the BEC packets outline is shown in the centre, with the three interferometry pulses shown; split, reflect and recombine, with the corresponding pulse shape shown on the right.

cloud position is calculated from a $\frac{1}{2}gt^2$ curve, as the cloud drops due to gravity.

Modelling the effect of the Gaussian on the beam power is a matter of introducing the drop distance, z, into the numerical simulation seen in figure 3.4. This introduces information of the beam shape. More specifically we wish to change the pulse height term, U_0, from equation 3.5 to now vary with the introduced distance parameter. In effect we now have

$$U_0 = A \exp\left[\frac{-2(z-z_0)^2}{w^2}\right], \tag{3.9}$$

where z_0, w and A represent the Gaussian free parameters - offset, width, amplitude - respectively. It is important to note for the simulation that A is measured in the number of recoil energies, and not a *direct* measure of beam power, rather an indication of the depth of the lattice formed in the retro-reflected interferometry beam. This therefore takes into account any uncertainties we had

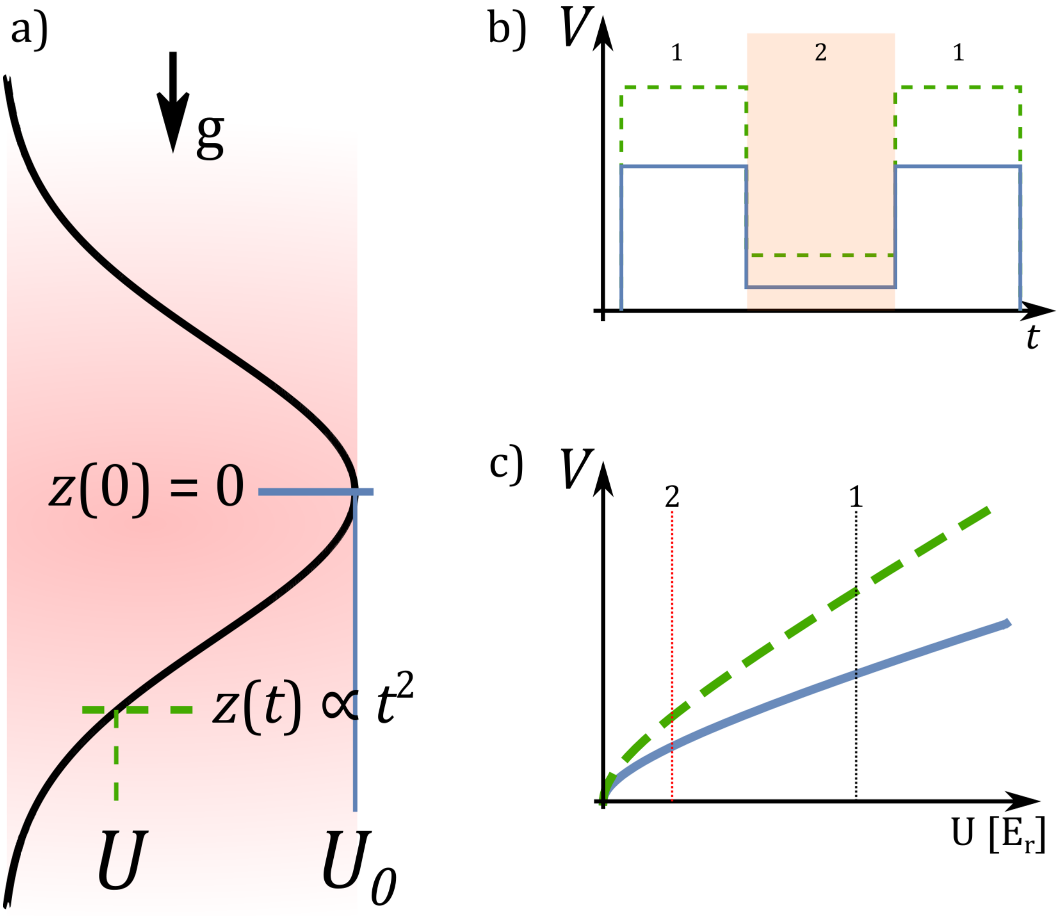

FIGURE 3.8: Outline of calibration of interferometry beam with BEC in freefall. a) By using the interferometry beam at different times after dropping the BEC to split the cloud, we can infer the shape of the beam. The BEC is small compared to the beam such that at points $z(0)$ and $z(t)$ the local intensity is different, P vs P_0 respectively, hence the pulse height the atoms see changes drastically, changing the split proportion. b) The first composite pulse has a shape denoted by the solid (blue) line - as seen by our AOM system as a voltage, V. At a later time the pulse will need to be scaled up in power in order to achieve the same split, denoted by the dashed (green) line. The curve is scaled by the ratio of beam powers, P/P_0. c) The calibration curve of the desired pulse height, U, vs control voltage necessary to achieve such. The same pulse energies (in recoil energy, E_r) required are denoted by 1 and 2 and similarly in the shaded regions in b).

about beam overlap, differences in power (due to loss in the glass for example) and other imperfections: it is a direct representation of the K.D. beam's useful power. Converting this energy into a power would more than likely underestimate it because of these factors.

With equation 3.5 now dependent on spatial variables all that is required now is to include it into a fitting algorithm with the Gaussian free parameters as fitting constants. We run this fit using Mathematica's `FindFit` command.

3.3.2 Pulse height with time calibration

We apply a rectangular pulse, 20 µs in length, of which we set our computer voltage control at a constant value, typically 0.7. This voltage-to-pulse calibration will allow us to set S in equation 3.8. This pulse in general is arbitrary, but a low voltage, i.e. a shallow lattice, will avoid ambiguities in the fit corresponding to exciting higher orders or as to generating complicated lines owing to figure 3.4 being convolved with a Gaussian. Figure 3.9 shows an example of one of these plots as the solid (orange) dots.

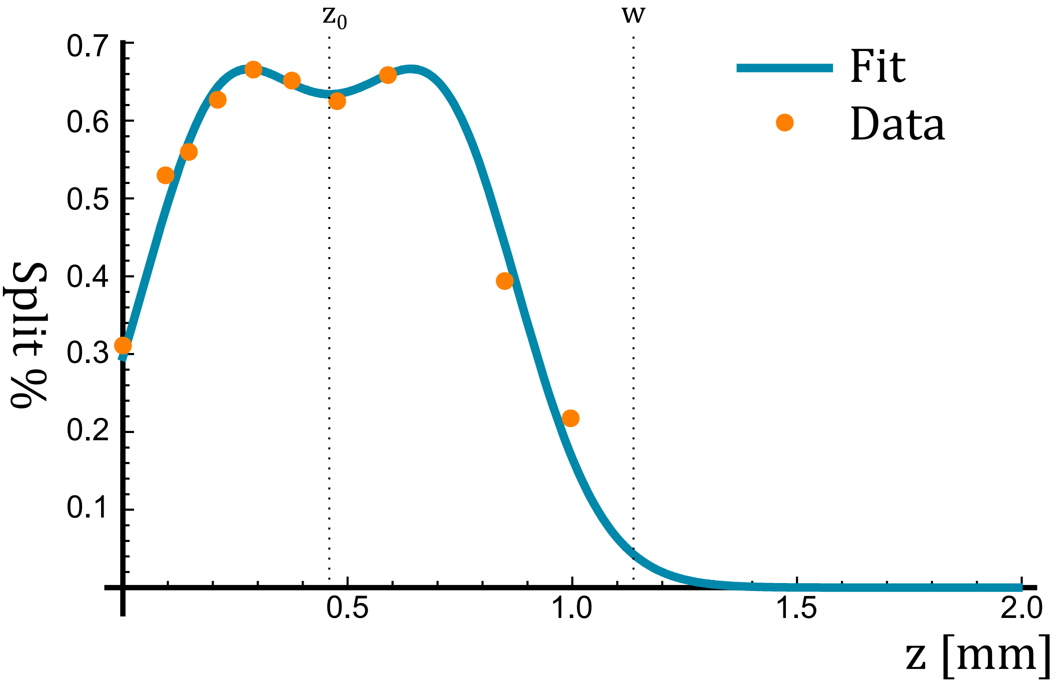

FIGURE 3.9: Calibration curve of the interferometry beam via measurement of the BEC split fraction as a function of the ballistic drop distance. The BEC is dropped for various times for which a distance is attributed. The same (20 µs, 0.7 V) square pulse is then applied and the percentage split into the $|\pm 2\hbar k\rangle$ is measured (orange circles - standard error is on order of the marker size and has been omitted for clarity). This is then fit to a numerical simulation as detailed in 3.1.4 with the pulse height as a free parameter (blue line). This allows us to determine the height (in recoils, E_r) and the width (in µm). The dashed lines denote the beam centre, z_0, and the $1/e^2$ waist, w as indicated.

From the fit of figure 3.9 to the pulse height we infer the scaling factor to be used in equation 3.8. For figure 3.9 the fit returned values for $A = 10.9\,E_r$, $w = 0.68\,\mathrm{mm}$ and $z_0 = 0.46\,\mathrm{mm}$, which sets S at 0.40. At the beam centre note the dip in the figure. The power in the beam is such that at z_0 the beam power is slightly over the first maxima of figure 3.4, hence moving from this position will take us over the crest, hence why moving positive or negative of this position looks symmetric. For reference the position of the waist is also plotted.

The calibration therefore, to ensure the same pulse height for any drop time, is

$$V(z) = S^{+}\left(A\,U + \sqrt{\frac{B}{S^{+}}U + (C\,U)^2}\right), \quad S^{+} = \frac{P_0}{P(z)}S, \tag{3.10}$$

where our pulse height, U informs the voltage, V in the same way it did in our beam calibration, however its is modulated by the ratio of beam intensity in the Gaussian, P_0/P multiplying the calibrated S.

3.4 Sensitivity to gravity: measuring asymmetry

One obvious consequence of dropping the condensate is that it begins to move. Unsurprisingly, because it is accelerating under gravity, its velocity increases the longer it is dropped for. The splitting operation is sensitive to this velocity as it is factored in as an initial momentum. Note in the previous derivation of the split populations in a Kapitza-Dirac split the atoms are assumed to be at rest. A small perturbation in velocity does not immediately bring the pulse into the Bragg-regime - but similarly it does bring an imbalance to the $\pm 2n\hbar k$ orders. This effect is simulated and compared with measurements in experiment.

With longer separation between pulses, the time the BEC spends in free-fall increases, and hence its velocity due to the downward acceleration of gravity will also increase. If the splitting beams are perfectly perpendicular to gravity (i.e. aligned in the horizontal, x-y plane) then such a velocity is ignored by the geometry of the beams. However small misalignments in the splitting beam axis means some of this velocity couples into the splitting beam, effectively causing an asymmetric detuning in the crossed beams. In the atom frame it is akin to seeing a moving lattice, which puts us in mind of the Bragg picture of section 3.1.2. The treatment is fundamentally different, since the angle, and thus the velocity, is small. We firstly describe a theoretical treatment, arriving at a small angle (first-order) approximation which we validate with experiment. This has potential implications as a 'tiltmeter', which we discuss at the end of the secion.

3.4.1 Angle-dependent Kapitza-Dirac splitting

In effect, by including an initial velocity we bias the entire energy-momentum parabola (i.e. figure 3.3) by the amount $v_0 = \hbar k_0$, which is plotted in figure 3.10. The k_0 here is a "virtual" wavenumber associated with the lattice period. An initial momentum implies an initial energy, which will bias the system somewhat up the curve. The shifts in momentum are still quantised by the $2n\hbar k$ values from the 2-photon transition, and hence the spacing does not shift. The positive and negative values are, however, no longer degenerate, and hence will have difference detuning values. This imbalance in detuning, simply treated, will change the Rabi frequencies of each transition, so that the same length pulse will deliver different populations.

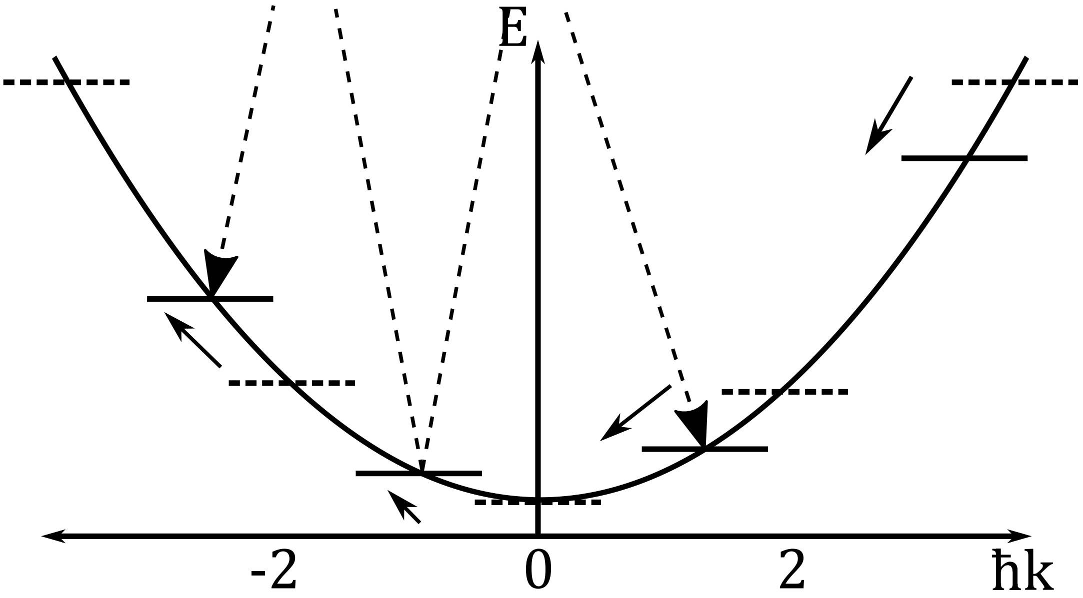

FIGURE 3.10: Illustration of the shifted energy levels in the momentum spectrum due to an added initial velocity to a Kapitza-Dirac pulse scheme. Note the forward and reverse momentum states are no longer degenerate.

One can simply take equation 3.1, in the spirit of [58], and add the small, non-integer initial velocity to the plane wave momentum states, $|2n\hbar k\rangle \rightarrow$

$|2(n+\epsilon)\hbar k\rangle$, where we have represented it as a fraction of one 2-photon transition, $\epsilon = v_0/2\hbar k$. This modifies the plane waves;

$$|\phi_n\rangle = e^{i2(n+\epsilon)kz}. \tag{3.11}$$

It is still straightforward to get to the coupled equations of 3.5, assuming the Fourier spectrum is also changed in the same way. This spectrum shift is illustrated by the arrows in figure 3.10.

Let us consider the effect of adding this perturbation to first order, i.e. the transition $|0\rangle \to |\pm 2n\hbar k\rangle$. The detuning previously for this same-two-photon transition was $\Delta = 2n^2 E_r/\hbar$, where we recall the recoil energy $E_r = \hbar k^2/2m$, which we now add an initial velocity, v_0. Our modified detuning is now, $\Delta' = \Delta + k \cdot v_0$, where we add the first order term from the Doppler shift. This will modify the Rabi frequency, $\Omega' = \sqrt{\Omega_2{}^2 + \Delta'^2}$, thus expanding the new Δ'^2,

$$\Delta'^2 = \left(n^2 \frac{\hbar k^2}{m} + k \cdot v_0\right)^2 = n^4 E_r{}^2 + 2n^2 \frac{\hbar k^2}{m} k \cdot v_0 + (k \cdot v_0)^2, \tag{3.12}$$

where we see the original detuning (first term) and two additional terms in $k \cdot v_0$. The term in v_0 will be identical for the transition to both the forward and reverse final momentum states, however the central $\propto k^3 v_0$ term will differ by sign. To calculate the population of the different momentum states in this closed system we expand the general expression for the Rabi oscillation, $P \propto \sin^2(\Omega\tau_p/2)$, to first order;

$$P_\pm \approx (\Omega'_\pm)^2 \frac{\tau_p^2}{4} + \mathcal{O}(\tau_p^4), \tag{3.13}$$

where τ_p denotes the pulse length. We can then take the difference between forward and negative populations, $A = P_- - P_+$, which we shall refer to as "Asymmetry", A. Noting the sign of $\vec{k} \cdot \vec{v}$ term in equation 3.12 changes between plus and minus orders, we obtain an expression for A,

$$\begin{aligned} A &= 4n^2 \frac{\hbar k^2}{m} k \cdot v_0 \frac{\tau_p^2}{4} \\ &= n^2 \frac{\hbar k^3}{2m} g \sin\theta \, t_d \tau_p^2, \end{aligned} \tag{3.14}$$

where we have replaced v_0 with the velocity due to gravity, $v_0 = g t_d/2$, where

t_d is the time the BEC has spent in freefall: the drop time. The beam (horizontal) and gravity (vertical) axes are perpendicular, and we measure the small angle, θ, with respect to the beam, we have used the sine term instead of the usual cosine found in dot products. With a fixed pulse time it is easy to see that the relationship between the drop time and the asymmetry is linear. This gradient then could be used to find the angle between the splitting beam and gravity, $\frac{dA}{dt_d} \propto \hat{k} \cdot \hat{g}$. For small angles this can be further reduced to linear in both θ and t_d. We will illustrate this in the next chapter.

3.4.2 Observation in Experiment

With the above, it is clear that the relationship between the perceived asymmetry in the system, the imbalance between ± momentum packets, and the initial velocity is linear. For the experiment of a BEC in freefall this velocity is related to the time at which the BEC has been in freefall, t_d, as it accelerates under gravity. Therefore by allowing the BEC to fall for various times and measuring the resultant asymmetry we can verify this. Figure 3.11 shows an example of a asymmetric split at $t_d = 10\,\text{ms}$ after release from the dipole trap, before applying a $10\,E_r$, 20 µs long KD pulse and imaging the split condensate. On the left is a line graph of each of the individual packets, normalised to the height of the central peak, which contains roughly 4×10^4 atoms. We integrate over 40 pixels in the x direction from each of the packet centres in order to fairly compare, as a horizontal cut through the packets would unfairly represent them given the angle at which they lie. The right image shows the full image of the split condensate, the 15% difference between the left and right packets visible to the eye.

For imaging it is worth noting that the condensate falls out of the camera's view if we leave it to fall for more than 20 ms. To obtain a more accurate number of atoms in the condensate we need to let the condensate expand for nearly 50 ms before imaging and fitting with a Thomas-Fermi distribution. To facilitate both imaging and expansion we turn the magnetic quadrupole back on to around 20 G/cm to accelerate atoms back into the camera view [116, 141]. After 80 ms this brings the atoms back to the centre of the camera. Since we are only interested in the atomic population this should not impact our results.

Figure 3.12 shows three such measurements where we have changed the vertical angle of the KD splitting beam through the atoms. This was achieved by adjusting the two-mirror dogleg before the cell along the KD beam path

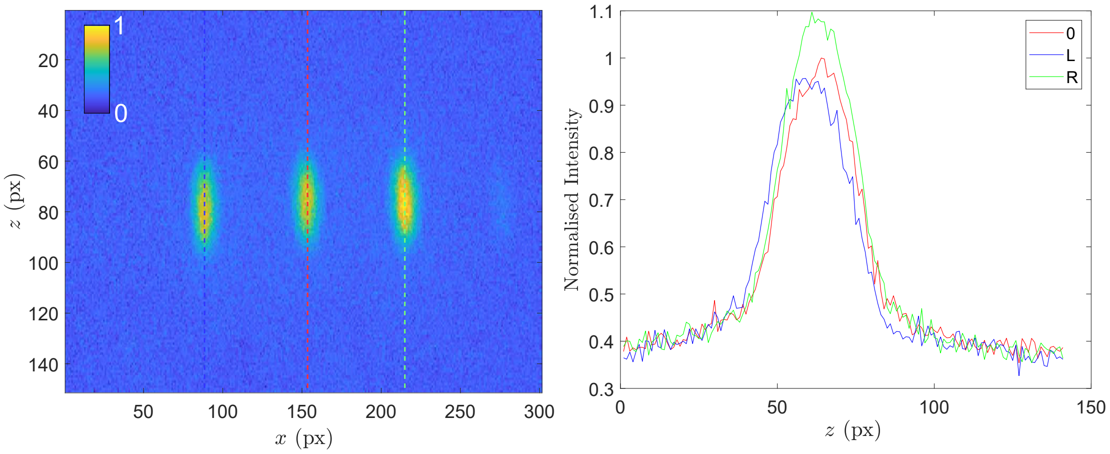

FIGURE 3.11: (Left) Image of the imbalanced condensate split after a drop time of $t_d = 10\,\mathrm{ms}$ a $20\,\mu\mathrm{s}$, $10E_r$ height pulse. One px corresponds to $7\,\mu\mathrm{m}$. (Right) The integrated line profile of each condensate where we have integrated across 40 pixels from each packet centre in the x direction. The (intensity) heights are normalised to the central peak. The centre condensate contains 4×10^4 atoms.

(the green shaded area of figure 3.6 (a)). The angle θ in the legend denotes the angle of the beam with respect to the horizontal plane perpendicular to gravity, and is calculated by the fitted gradient ($\frac{dA}{dt_d}$, denoted by the dashed lines) with equation 3.14.

3.4.3 As a measure of angle relative to Gravity

Measuring the angle with respect to gravity is a key alignment step for many measurement devices, including atomic gravimeters [142–144] and terrestrial gravitational wave observatories [145, 146]. The idea of an atomic or "quantum" tiltmeter is not new [147, 148], but these are primarily based on interferometric measurements, utilising the phase induced by deflection from gravity [125, 149]. Here we are measuring the tilt of our splitting beam with respect to gravity via the imbalance in the split and not an interferometric quantity, hence causes of spurious phase in the interferometer, such as beam flicker, is not an issue. Still, one must be confident enough that this initial velocity is due to the misalignment of the beam and not another source of velocity such as a stray magnetic field gradient[63, 116], or release from the side of a harmonic trap [68, 150].

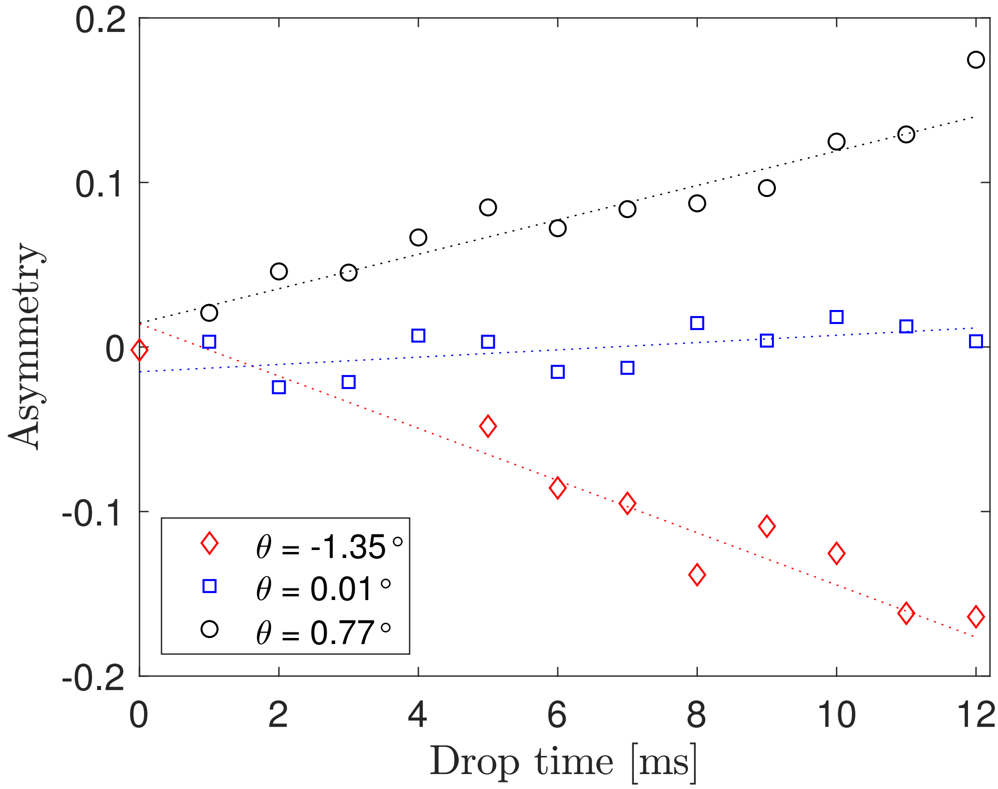

FIGURE 3.12: Asymmetry as a function of the drop time for various alignments of the splitting beam perpendicular to gravity. Once split, the difference in population between the $|\pm 2\hbar k\rangle$ momentum states is defined as the asymmetry. The values of angle in the legend are calculated using equation 3.14. Standard error is less than one symbols width and has been omitted.

Equation 3.14 shows that the Asymmetry and drop time are linearly related via the drop angle, for small angles. In figure 3.13 we plot the gradients measured on fig 3.12 against the angle measured geometrically using the camera image. As seen above in figure 3.11 the height of the packets are different for the left and right going condensates. We find the centre of each peak by fitting each peak with a Thomas-Fermi profile [71] and draw a line through them. We can then compare this line with the axis of gravity, which we know from dropping the condensate. Our camera is also at an angle to the interferometry beam by $45 \pm 1°$ in the horizontal $(x - y)$ plane - as seen in figure 3.6 - which will scale the result by $1/\sqrt{2}$. With this knowledge we geometrically attribute an angle of the beam with respect to gravity.

A fit to the data is plotted (in red) with the dashed lines representing the first order confidence bounds. We also plot the derivative of equation 3.14 with

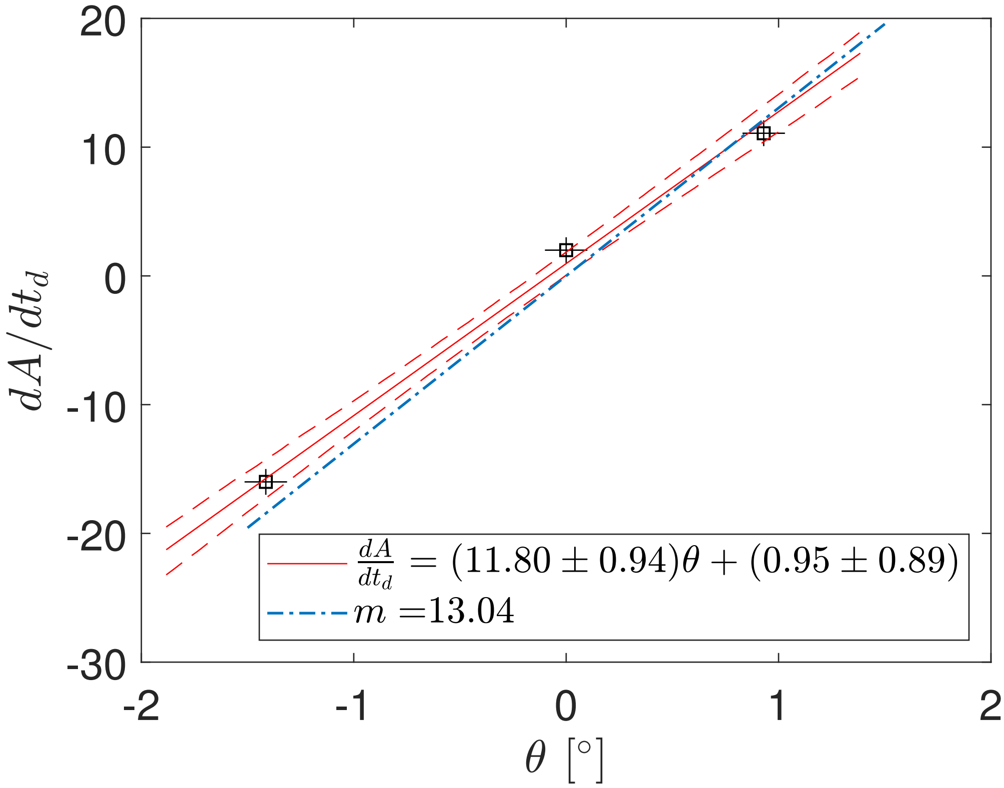

FIGURE 3.13: Plot of the gradient of asymmetry vs. drop time, $\frac{dA}{dt}$, against the beam angle with respect to gravity, as measured geometrically using the imaging camera. The data in figure 3.12 is plotted as the (black) squares. The solid (red) line is a fit to this data, with the (red) dashed lines showing the first order standard deviation. Values are plotted in the legend. The (blue) dash-dot line is the gradient of the first order calculation as in equation 3.14 for the pulse used (see text).

respect to t_d (in blue) for comparison. We use an uncertainty in θ of 0.1° from our fit through the peak centres on the camera image - but this may be a generous overestimate given the few data points, and the fact the split is in 3D. Our purpose of this calibration was to align the beam perpendicular to gravity to avoid asymmetry affecting our results, as such this is more of a proof-of-principle tiltmeter with a resolution of $\approx$ 1 mrad in comparison to atomic tiltmeters with µrad resolution. The data is similar enough to our theoretical curve, so in practice a single plot of asymmetry versus drop time could then be input and the angle read out, but our current error in calibration rules this out as use as a high-sensitivity tiltmeter. It is, however, a useful calibration for techniques involving Kapitza-Dirac splitting under gravity - key for our interferometer with a BEC in freefall as seen in chapter 4.

Chapter 4

Using the BEC interferometer

We now have the requisite parts to form an interferometer. The purpose of this chapter is to introduce the method we have used to trial finding a signal and in particular rotating the table. A calculation of the phase accumulation for the freefall interferometer is detailed in section 4.1. We must then be able to vary the phase somehow, which in the case of pure Sagnac measurement means moving the table at some rate. This has been achieved in other international labs by moving the table mechanically [39, 57]. We use a piezoelectric stack to move our table, which is floating on pneumatic air as is standard to reduce vibrations on the table, detailed in section 4.2. To have a better idea of what this entails and how to attribute this to a rotation we install an optical Michelson interferometer to co-measure the table displacement. We show early data from our atom-interferometer during rotation and non-rotation of the experimental table, and establish a roadmap of improvements toward a distinguishable measurement.

4.1 Calculating phase

In this section we make an estimate on the parameter space of our interferometer to inform the rate at which we will need to make a measurable rotation. This allows us to predict the strength of signal we should expect to see given a particular rotation rate.

4.1.1 Sensitivity for the freefall BEC interferometer

The area traced by the split halves of the BEC is equivalent to that of a kite whose area we know simply as one half of the product of its diagonals. Therefore we need to know how far apart the packets travel before they are reversed,

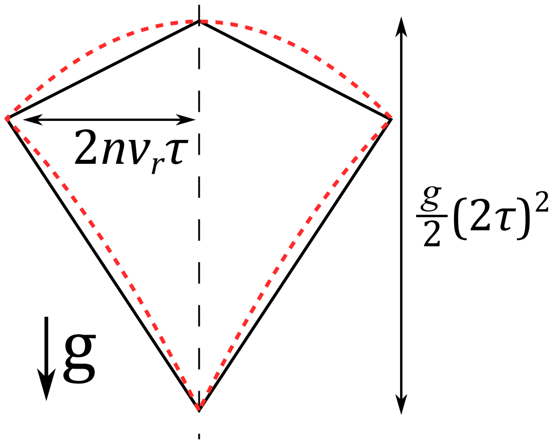

FIGURE 4.1: Lengths in the calculation of the kite-shape interferometer area. The BEC is released from the top of the shape and accelerates towards the bottom of the page. The total area enclosed is proportional to $4nv_rg\tau^3$, with τ the symmetric interferometer time, v_r the recoil velocity and n an integer denoting the momentum state after the BEC split. The dashed line shows the true path traced by the atoms in time, accounting for the parabolic trajectory under gravity. Both kites have the same area.

and by how far they are dropped, which we find with simple Newtonian mechanics. The packets receive $2n\hbar k$ recoil when split initially and travel the symmetric interferometer time, τ, apart. Here the n is an integer denoting the momentum state the condensate is excited into, and we remember that k is the wave-number of the incident field. More detail on the splitting mechanism can be found in chapter 3. One packet will therefore travel with $2n$ times the recoil *velocity*, $v_r = \hbar k/m$. The condensate is always falling due to gravity during the interferometer sequence, hence is accelerated by g, the gravitational acceleration at the earth's surface, over the full 2τ. A diagram of this can be found in figure 4.1. The area, A_{ff}, is given as

$$A_{ff} = 4nv_rg\tau^3, \tag{4.1}$$

where we note the τ^3 dependence. The motion under gravity is parabolic, so our kite in Figure 4.1 should look more curved because of this, as denoted by the dashed line, making the area calculation parametric in time. However, if one integrates the equations of motion to find the area we arrive at the same result as equation 4.1. We therefore say that the accumulated phase grows with the cube of the symmetric interferometer time. Longer drop times achieve larger sensitivities, as the accumulated phase difference will increase significantly for longer interferometer times. The phase difference, as per equation 1.5 is given by,

$$\Delta\phi = \frac{2\, m_{87}}{\hbar}\, A_{ff}\, \Omega = \frac{8\, n\, v_r\, g\, m_{87}}{\hbar}\, \tau^3\, \Omega, \tag{4.2}$$

giving us our two experimental controls, the rotation rate and symmetric time.

In this experiment we use an $n = 1$ interferometer, so only the first momentum eigenstate is excited. Ways to excite to higher momentum states exist [127, 151, 152], but it is difficult to achieve with Kapitza-Dirac type splitting alone[1]. Rubidium-87 has a recoil velocity of $v_r = 5.89\,\mathrm{mm\,s^{-1}}$ [153], and we take gravity as $g = 9.8\,\mathrm{m\,s^{-2}}$. This gives us an interferometer area of $A_{ff} = 0.23\,\mathrm{mm}^2$ for a $\tau = 10\,\mathrm{ms}$ symmetric time. This area is comparable to other guided apparatus, including $0.5\,\mathrm{mm}^2$ magnetic [57] and $0.2\,\mathrm{mm}^2$ optical [41] variants. Free space interferometers, such as those operating on fountains, can achieve areas of $11\,\mathrm{cm}^2$ [154], given (thermal) atoms that travel distances nearly 1 m in length.

4.1.2 Phase map

We can now draw a map of the phase difference as a function of the two experimental controls, Ω and τ. The phase difference present in a rotating interferometer is given by equation 1.5. The phase difference in a BEC interferometer with Kaptiza-Dirac pulses exhibits itself as a difference in the fractional populations of the atomic momentum states - in our case between $|0\hbar k\rangle$ and joint $|\pm 2\hbar k\rangle$. Remember the excited $|\pm 2\hbar k\rangle$ states are degenerate, comprising a single excited state (see figure 3.3). In theory, a closed interferometer will return all its population back to the $|0\hbar k\rangle$ state in the absence of any perturbing fields, but in reality the atom optic operations will add a phase themselves so some population will be present in the $|\pm 2\hbar k\rangle$ state. We must therefore compare the non-rotated interferometer with a rotated one in order to discern a phase difference which we can attribute to a rotation.

The change in phase as a function of fractional population of the (symmetrically populated - see section 3.4) first momentum state, $|\pm 2\hbar k\rangle$, is given by;

$$\Delta P_1 = \left| P_{|0\hbar k\rangle} - P_{|\pm 2\hbar k\rangle} \right| = \frac{1}{2}\left(1 - \cos\left(\Delta\phi + \phi_0\right)\right), \tag{4.3}$$

---

[1] With composite pulses we can directly address higher momentum state transitions, but the linewdith of such transitions greatly decreases with increasing n and hence are more vulnerable to timing and intensity errors.

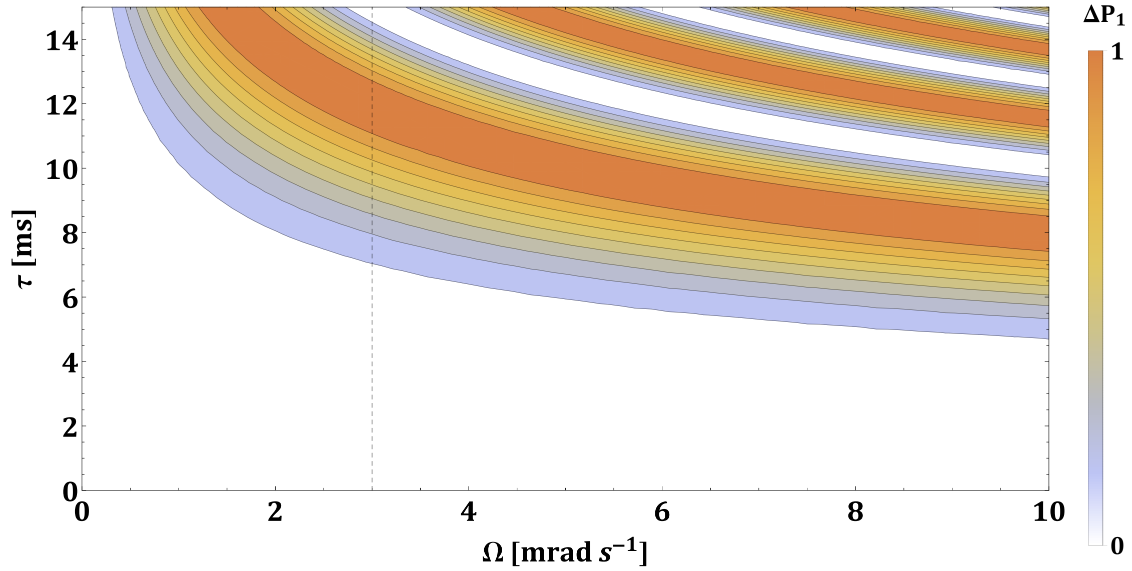

FIGURE 4.2: Contour map of population change, ΔP_1, as a function of the two interferometer parameters; symmetric time (the separation between pulses), τ, and the rotation rate, Ω. The dashed line denotes the rotation rate of the table in the shaded area of Figure 4.4

where we add an arbitrary offset phase, ϕ_0, based on the additional phases gained from the light pulses [116, 155]. We plot this absolute difference for $\phi_0 = 0$ in figure 4.2. The vertical line denotes a rotation rate of $3\,\mu\mathrm{rad\,s}^{-1}$, which is the fastest we are able to push our table (see section 4.2). At this rate, we expect 50% of our population to shift with $\tau = 10\,\mathrm{ms}$.

4.2 Applying an artificial rotation

We need some form of rotation to detect that we can apply deterministically with relative ease. An obvious choice might be to mount the interferometer apparatus on top of a rotating / floating platform, but this is unfeasible given the optical access constraints modern atomic physics apparatus have. However, a common part of modern optics experiments may be able to help here - the floating optical table, usually employed to decouple ground vibrations from disturbing sensitive optics and lasers. The table floats on pneumatic legs which damp vibrations on the table. We can rotate the table in a fashion by giving the table a "shove" and letting the pneumatic legs absorb the shock. A recent experiment by Moan *et al* [57] use a translation stage to push the table.

In a similar fashion, piezoelectric transducers (PZTs) have been used by Gustavson *et al* [39] to rotate their apparatus. We will also use a PZT in order to induce a motion on the table.

4.2.1 Piezoelectric displacement of the optical table

We use a Thorlabs PK4GA7P1 Piezoelectric stack, which has large free-stroke displacement of 100 µm when provided with a 150 V bias. "Stack" here denotes that the construction of the PZT consists of many smaller PZTs bonded together to which the biasing voltage is applied simultaneously. The advantage of using this is that the actuation is still quick without sacrificing blocking (i.e. pushing) force when compared with amplified piezoelectric actuators for instance [156], which may travel millimetre distances but are compromised by a weaker blocking force.

Figure 4.3 shows a photograph of the apparatus, including the PZT it its holster (inset), secured to one of the floor-contact legs of the table. A hemispherical ceramic cap ensures contact between the PZT and the table at all times throughout its motion.

We need the PZT to move fast in order to generate rotation rates that we can observe using our interferometer. This leads us to a limitation with the electronic driver that will control the PZT. The slew rate, S_R, measured in $\mathrm{V\,s^{-1}}$, gives us an indication of the speed of PZT actuation, governed by the capacitance of the device, C, and the peak current, I_{pk}, the driver can provide, $S_R = I_{\mathrm{pk}}/C$. Our PZT, due to its size and its stacked-PZT construction, has a relatively high capacitance of 17 µF, where most PZTs quote their capacitances in 100s of nF.

We found that common piezoelectric drivers (e.g. Thorlabs K-cube KPZ101) cannot drive our PZT fast enough as they are limited by the peak current they can safely generate. The K-cube for instance can provide a peak current of $I_{\mathrm{pk}} = 7.5\,\mathrm{mA}$, hence has a slew rate of $S_R = 441\,\mathrm{V\,s^{-1}}$. The rise time, that is the time it will take the PZT to fully extend when a voltage is applied, t_r, is found by

$$t_r = \frac{CV_{PZT}}{I_{\mathrm{pk}}} = \frac{V_{PZT}}{S_R}, \tag{4.4}$$

which for a 150 V PZT is 350 ms, corresponding to a rotation rate of under $0.2\,\mathrm{mrad\,s^{-1}}$. We need to increase the current the driver can supply in order to overcome the high capacitance. We use a PIEZODRIVE MX200 driver, which

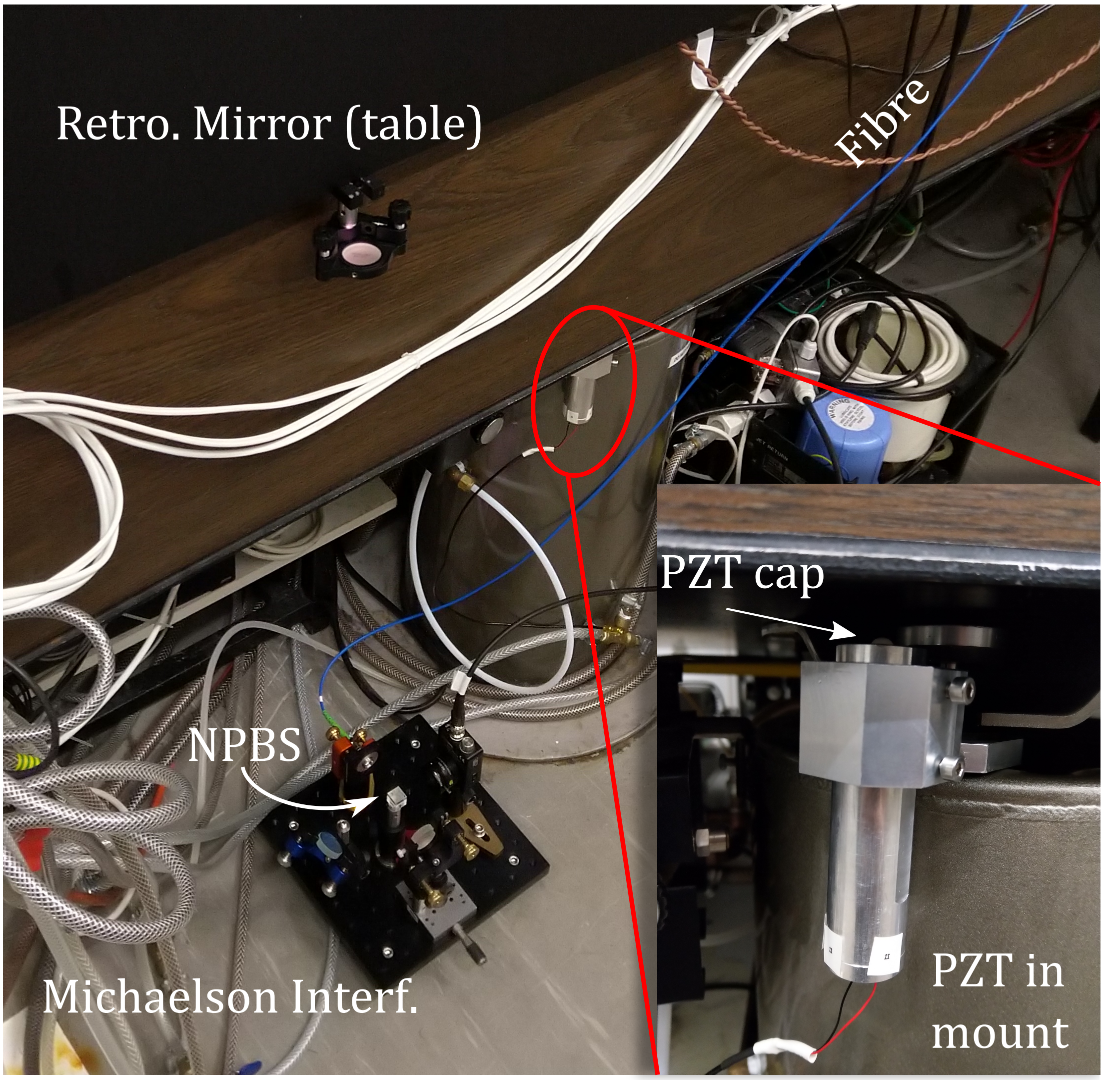

FIGURE 4.3: Photograph of the PZT-table apparatus, showing the PZT in holster (inset) attached to one of the floor-contact legs used to generate a rotation, and the Michelson interferometer used to co-measure the table's movement. One arm of the Michelson reflects off the "Retro. Mirror" connected to the floating table, and is split and recombined on a single non-polarising beam splitter cube.

can safely deliver a peak current of $I_{\mathrm{pk}} = 1\,\mathrm{A}$. For a rise time of $t_r = 10\,\mathrm{ms}$, a peak current of 255 mA is required, which this driver can safely produce.

We now have a means of pushing our table and inducing a rotation that we believe will be sufficient to be picked up by the BEC interferometer. We need to verify that the PZT is moving the table at the speeds we expect it to. We check by means of a Michelson interferometer, as detailed in the following section.

4.2.2 Attributing a rotation rate

To directly measure the table's motion we install a Michelson interferometer, as seen on the laboratory floor on figure 4.3. One arm of the Michelson reflects off a mirror attached to the floating table, whilst the rest of the apparatus rests on the floor. Light from one of our beam dumps (for the cooling laser) is fibred in from the table as a light source. The Michelson breadboard is mounted on vibration-damping feet (Sorbothane®, AV4/M) to minimise disturbances from the floor.

The optical Michelson interferometer gives us a record of the speed of the table above the leg closest to the interferometer. As the table moves fringes are seen on the photodetector from the interference between the Michelson arms. One complete fringe is attributable to a distance in the "table arm" of the Michelson of $\lambda/2$, and the corresponding velocity is this distance divided by the time taken for each full interferometer fringe.

To attribute this to a rotation rate we can make a simple geometric argument. Our table legs are spaced 1.65 m apart, with the sets of legs across the smaller edge coupled together, hence we need only consider this longer edge dimension. The rotation rate then is simply

$$\Omega = \frac{d_t}{1.65t}, \tag{4.5}$$

where d_t is the distance travelled during the time, t. For a rotation rate of $3\,\mathrm{mrad\,s^{-1}}$, with our $d_t = 100\,\mu\mathrm{m}$ long PZT we need $t = 20\,\mathrm{ms}$. The cloud will drop roughly 2mm in this time, which is slightly outside our interferometry beam waist.

In truth it is not as simple. The PZT does not simply "push" the table with a constant speed as it extends, instead it must be thought more as an acceleration. Figure 4.4 shows the trajectory of the table as measured by the Michelson interferometer. The instantaneous rotation rate is worked out as the velocity, $v = d_t/t$, divided by the leg length, $\Omega = \frac{v}{1.65}\ ^\circ\mathrm{s}^{-1}$. In this figure a 20 ms long sinusoidal ramp is applied to the PZT. The first (left) dashed line denotes when the PZT is fully extended. Notice that the table continues to travel after the PZT has extended, and that the corresponding table speed begins to decrease, as gravity is now slowing the table, reaching its peak height at the second (right) dashed line. The peak speed however is reached before the PZT fully extends. The (red) shaded region denotes where the interferometry sequence takes place, shown as having a total interferometer time of 20 ms.

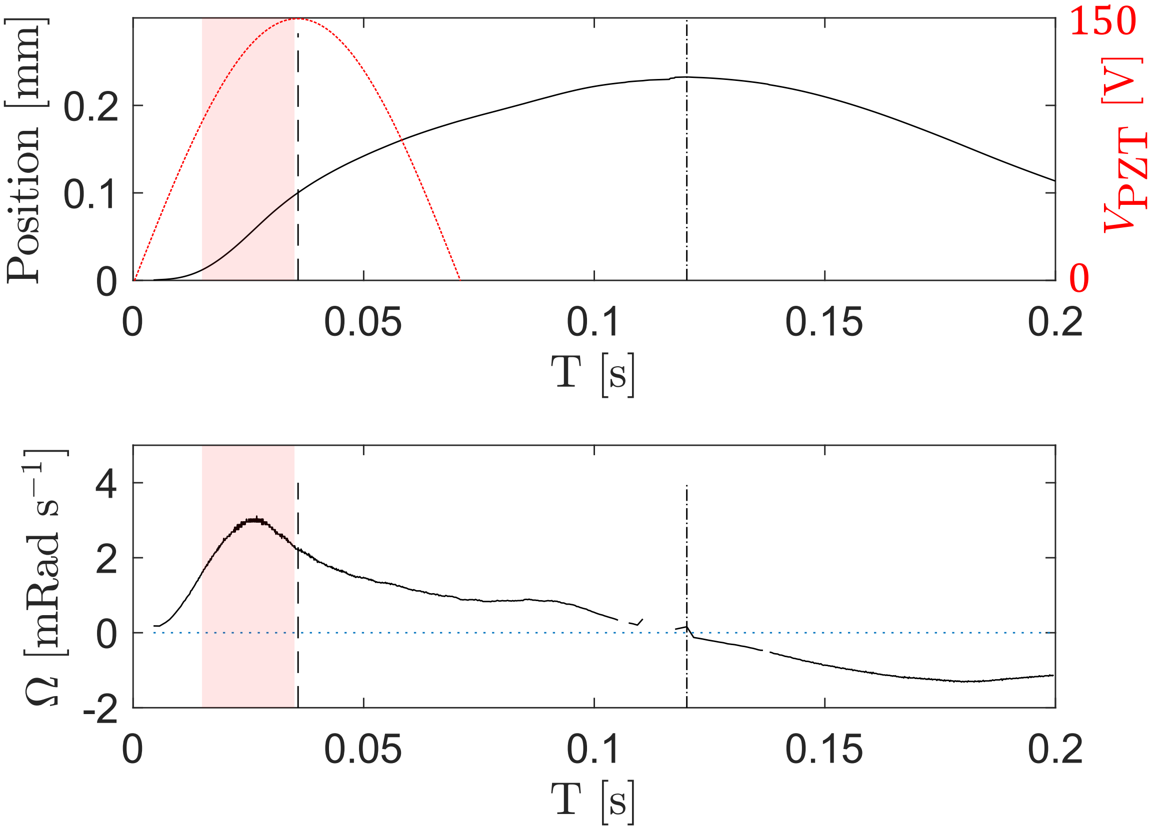

FIGURE 4.4: The table trajectory curve as recorded on the optical Michelson interferometer, showing the displacement (top) and the projected rotation rate (bottom). Dashed vertical lines denotes the peak of the PZT drive - as highlighted by the dotted PZT voltage curve (top, red) reaching the apex of the sinusoid. The dash-dot line denotes where the velocity inverts and the table begins to fall with gravity. Interferometry is performed around the apex of the velocity/rotation curve at 35 ms, where the shaded region denotes the time the atoms are in freefall. We have omitted data around $\Omega \approx 0$ due to noise on the Michelson output.

4.3 Sagnac Measurement

Now we have all the parts together to perform a Sagnac measurement. The interferometry sequence goes as such: after a BEC is generated in a crossed dipole trap, the trap is turned off and the BEC allowed to fall under gravity; simultaneously a KD pulse splits the BEC into two packets with $|\pm 2\hbar k\rangle$ momentum; a time τ is allowed to pass before the packets are reflected using a Blackmann pulse, and recombined after an additional τ time. The resulting interference between the two packets is presented by the population difference between the $|0\hbar k\rangle$ and $|\pm 2\hbar k\rangle$ states.

Figure 4.5 shows the same measurement repeated over the course of half an hour. Here we use a symmetric interferometer time of $\tau = 7.5\,\mathrm{ms}$. We record the fractional population of the $|0\hbar k\rangle$ state (i.e. the central lobe on figure 3.11 (b)). To aid in distinguishing a rotation signal from noise or experimental drift, the table is only rotated on even numbered shots, hence we *interleave* rotated with non-rotated shots. These are shown by the cross and circles on figure 4.5. We take the mean and standard error for each set. The rotated data has a mean population of $39 \pm 3\%$ and the non-rotated with $41 \pm 3\%$. The two are within standard error - so no clear distinction is seen in this particular shot.

4.3.1 Discussion

Our choice here for $\tau = 7.5\,\mathrm{ms}$ was as large as we could achieve before our beam ran out of power to perform a closing pulse efficiently. At $\tau = 10\,\mathrm{ms}$ the BEC drops roughly 2 mm and is well into the tail of our Gaussian interferometry beam. Our interferometer area therefore has dropped by a factor of $\left(\frac{7.5}{10}\right)^3 \approx 0.42$.

There are sections of data (e.g. figure 4.5: 22-28 min) where the rotated and non-rotated data are distinctly separate, although equally there are times the two move in step (e.g. 1-10 min). There are experimental drifts here that affect the phase of the interferometer we have not attributed; to name a few, magnetic fields [116], laser intensity fluctuations [157] and wavefront curvature [140]. Great effort has been made to minimise the effects of stray magnetic fields and laser intensity fluctuations [63, 64]. We assume the interferometry beam is collimated well enough that it is incident on the BEC well inside the Rayleigh length. However, there may be some residual curvature of the beam that affects the phase in-between the pulses, especially at the closing pulse

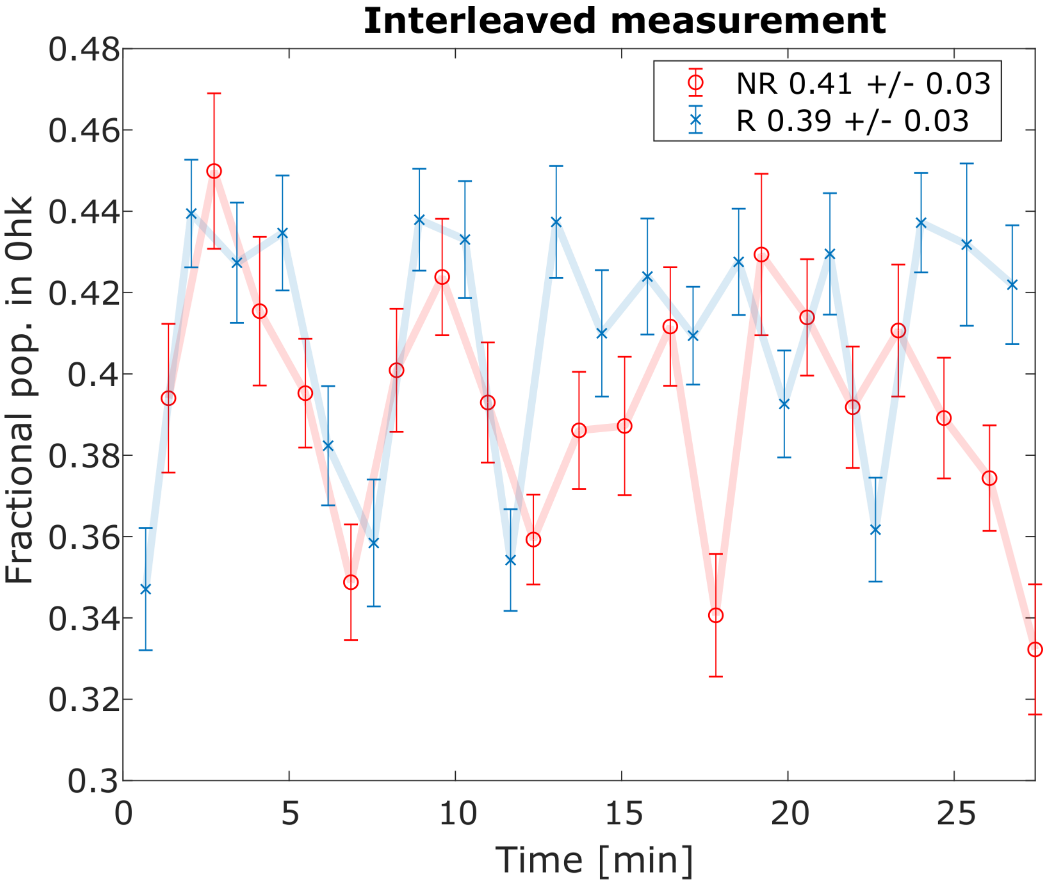

FIGURE 4.5: Fractional population in the $|0\hbar k\rangle$ state after interferometry for the same interferometry sequence over 30 minutes. The symmetric interferometer time is $\tau = 7.5\,\mathrm{ms}$. The rotation of the table is applied every other shot in an interleaved measurement. The crosses (blue) and circles (red) denote measurements where respectively the table rotation is (R) and is not (NR) applied. The difference in the means of each set is roughly 2% with an uncertainly of 3%, showing no clear distinction from noise; although some parts of the data show a clear distinction between rotated to non-rotated shot. The oscillatory behaviour may be indicative of sensitivity to ambient temperature.

which takes place at the edge - and therefore most curved - part of the Gaussian beam. This affect would apply to both rotated and non-rotated data, but may serve to explain some decrease in the contrast

No distinguishable measure of rotation is presented here: either the table does not move fast enough to introduce a large enough phase shift, or the signal contrast itself is too low. As seen in figure 4.2 for a symmetric time of $\tau = 7.5\,\mathrm{ms}$ and rotation rate of $\Omega = 3\,\mu\mathrm{rad\,s^{-1}}$ then we expect a population change of around 10%. The calulations of population in section 4.1 are all contingent on the signal contrast being 100%. Early measures of interferometer pulse *efficiency* estimate this to be in the high 80% (via three-packet contrast interferometry, see previous work of Mackellar [64] and Robertson [63]) but this data suggests it may be lower than 20 %. We routinely see mean values in fractional population difference of 2 % to 4 % in figure 4.5. Running for a longer interferometer time will greatly increase this, owing to the phase scaling with τ^3 as in equation 4.2.

There is also a discussion surrounding mean field effects, an expansion of the BEC owing to self-repulsion of the cloud, affecting the phase of the BEC [158]. We are yet to see any noticeable difference in signal when releasing the cloud immediately into interferometry, or waiting for mean-field effects to abate before splitting. For investigations into mean-field effects using this apparatus see the theses of Mackellar [64] and Halket [159]. More work needs to be performed to determine performance and to investigate likely sources of phase-noise and experimental instability, given the sinusoidal character of some data in figure 4.5, indicating perhaps a temperature fluctuation with a six minute period, given the time-scale. Alternatively, using a PZT with a greater blocking force, rather than a long travel distance, could be more useful as it could potentially launch the table with a greater velocity and achieve greater rotation rates.

To push into higher values of τ we need to get around problems with our power in the KD beam. One such solution is to start the cloud at the top of the Gaussian and use the full diameter of the beam, which $2w = 1.36\,\text{mm}$ currently. The BEC travels 2 mm over the total interferometer time of 20 ms (i.e. $\tau = 10\,\text{ms}$), hence even then the beam diameter needs to be larger than it currently is, which also necessitates an increase in the power available in the beam. Currently we are limited to around 4 mW of power in the KD beam at the chamber, corresponding to a control voltage of 5 V (see figure 3.6 b)). In the current configuration, after 15 ms in order to apply a closing pulse (with max pulse height of 6.06 recoil energies) we need to increase our power by a factor of 4 - as described in section 3.3. By means of comparison our control voltage is 1.18 V at this point. Similarly, after 20 ms our power would need to increase by a factor of 91 - asking the control voltage to be $> 5\,\text{V}$, exceeding our maximum power. There is potential to gain a lot of power by removing the fibre in the KD beam path, which has an insertion loss of around 48%, but the purpose of said fibre was to ensure the Gaussian shape of the beam, as the KD laser source is from an ECDL with an elliptical-shaped output [63, 65].

Replacing the source with a higher-power output is another solution, albeit an expensive one. In summary, with more power in our interferometry beam we would be able to close the interferometer fully at longer drop times, leading to an increased area, and hence an increased sensitivity to the applied rotation.

Assuming an interferometer contrast of around 20 % then we would expect to see a signal twice the standard error by increasing $\tau > 9\,\mathrm{ms}$. As it currently stands we would need 15 times more power to close the interferometer efficiently after $2\tau = 18\,\mathrm{ms}$, or if we expanded the beam to have a waist of $w = 2\,\mathrm{mm}$ then we only require a 4 times increase in power. One solution is therefore to replace KD beam laser source with a higher power laser. Alternatively, we need only expand the beam along the axis of gravity, so using cylindrical lenses may be appropriate in this case, which will reduce the realtive increase in power by a factor of $\sqrt{w}$. Another option is to use the current laser as a seed laser and injection lock a second laser with a higher output [160], thus preserving the spectral qualities whilst increasing power. These considerations motivate future experimental changes that will hopefully bring us to a successful measurement of rotation.

Part III

Fresnel Zone Plate

Chapter 5

Optical waveguides and the Fresnel Zone Plate

The interferometer geometry described in chapter 4, that is a BEC falling under gravity, has one major downside in that it can only measure rotations about axes *perpendicular* to gravity. One therefore cannot make a 3D gyroscope, or hope to use this geometry solely in order to construct one. In a similar vein of wishing to minimise apparatus footprint but maximise area, we can use confining potentials to guide our atoms in a loop in order to be sensitive to the Sagnac effect. Using light to guide the atoms, we can make configurable traps with careful use of optical devices.

Atom interferometry performed in guiding potentials is of particular interest to us, as macroscopic geometries can be constructed with minimal apparatus footprint. The equivalent of a meter long drop distance in freefall could be the size of a pea if confined within a ring geometry, for instance. Generating such traps is no easy feat.

In this section we detail the theory behind the generation of the Fresnel zone plate (FZP) and some experimental results. The generation and theory of the priciple of application to atom trapping has been described in the group before in the work of V. Henderson [61, 65]. We detail the fundamentals to understand the FZP method of trap generation in this chapter, with particular attention to ring traps because of their applications in the measurement of rotation. Chapter 6 contains results from simulation of a new regime of interest - high numerical aperture FZPs (High NA FZP), where the trap reflects local changes in intensity, and global changes of phase. These simulations are performed in a "hybrid" arrangement, where an FZP and a spatial light modulator (SLM) are used in conjunction to create dynamic, high NA, high accuracy atom traps.

5.1 Optical Waveguides

In this section we shall review some state of the art optical trap and waveguide configurations that can be used to generate ring-traps and others.

Trapping atoms, that is to localise an atomic distribution in *space*, is a key requisite to many modern cold-atom experiments. The magneto-optical trap (MOT), as described in chapter 2, is perhaps the most widely used and can hold $> 1 \times 10^{10}$ atoms at µK temperatures. Atoms stored in MOTs however are not particularly dense, limited by radiation trapping - where scattered photons are recaptured by the cloud before they can escape, providing an effective inter-atom force. The strong light scattering cross section means that this trap is ill suited for waveguide generation.

Optical dipole traps are an inspiration for a class of waveguides. Optical dipole traps are conceptually simple, as they rely on the intensity of light. Atoms are attracted to regions of intense (a lack of) light given that the beam is red (blue) detuned from resonance. The force is weak, so traps tend to be shallow compared to the larger radiation pressure and magnetic traps at a few mK in depth. Optical dipole traps can be made such that their optical excitation rate is very low, and as such can store dense ensembles of atoms at extremely low temperatures for relatively long times. Choice value of detuning also means that losses to light scatter are low [85]. Their flexibility in generation is what is most exciting, as exotic geometries may be produced to investigate interesting physical problems [161].

We have already described the mechanisms by which these traps work in section 2.1. Trapping atoms was first demonstrated for neutral atoms by Chu et al [162] who trapped roughly 500 sodium atoms at the focus of a 10 µm Gaussian beam, loading from a molasses cooled cloud. Miller et al. demonstrated a much more successful dipole trap, coined the far off resonant trap (FORT), loading atoms from a MOT at much lower temperatures [163]. The FORT demonstrated that using a highly intense, THz red detuned beam can be an effective trap, with negligible spontaneous emission.

5.1.1 Time-average trap generation

The field of atomtronics [56, 164, 165] requires some exotic trap shapes where atoms are confined in potentials that bend, split, loop, have barriers, etc. These sorts of waveguide shapes are not easily generated with static beams[1], and so another method to generate these is required. One method is to use interference, which we discuss in section 5.1.3. Another is to use dynamically painted potentials, where the trapping beam is swept faster than the trapping frequencies for the atom, such that the atoms feel the *time-average* of the potential.

Moving a beam fast enough can be done in a number of ways. Sweeping a single focus gaussian beam using acoustic optical modulators (AOMs) is one method, as the angle of the beam can be changed by altering the frequency of modulation at the AOM. Two AOMs in series angled perpendicular to each other allow for full transverse coverage [46, 47]. For more complicated pattern design, it is then a matter of designing appropriate parametric curves that when fed to the AOM controllers will reproduce the target [166]. This technique has already realised a number of patterns relevent to atomtronics [48, 167, 168]. Because the potential is an average over time there are imperfections due to the scanning, including inducing a phase across the condensate in a ring trap [169]. Because this technique relies on the focus of a single gaussian beam, which only weakly traps along the beam (propagation) axis, some form of light sheet is also usually needed [47, 170].

There is also considerable work done with adiabatic traps - those of a combination of magnetic and radio frequcney radiation [171]. These are not as flexible as the painted potentials, but can generate smooth “shell traps” [172–174] and toroids [45, 175], for use where ring-traps are applicable, such as in atomic interferometry and sagnac sensing [56].

5.1.2 Blue Detuned Traps

Most traps previously discussed in the literature use red-detuned guides, as the correlation between intensity and atomic potential is intuitive and simple to generate, as atoms are attracted to areas of highest intensity. Blue detuned traps however make use of the repulsive nature of such light to confine atoms in areas of darkness, but require a bit more complex engineering in order to confine atoms completely. The process of generating such traps is a varied and broad topic [176].

---

[1] One may suggest to just “cut” the beam into the required shape by amplitude modulation, but diffraction from edges and significant power losses make this approach undesirable compared to the other methods mentioned in this section.

We know that the strength of the two light-matter forces, radiation pressure (from atomic scatter) and the dipole force, can be expressed in terms of the common laboratory parameters intensity, I, and detuning, Δ,

$$F_{\mathrm{S}} \propto \frac{I}{\Delta^2}, \; F_{\mathrm{D}} \propto \frac{I}{\Delta}, \tag{5.1}$$

where it is most important to note that the dipole force depends on the sign of the detuning directly; we cannot make a blue-detuned MOT[2]. To avoid scatter the red detuned traps make use of large intensities to offset the large detuning values. In the blue case it is slightly different. Because we now trap in areas of *low* intensity, atoms with low energy, i.e. at lower temperatures, will not experience great amounts of scatter. Therefore, the requirement that our detuning be large is not as strict in the case of blue detuning, as cold atoms will not spend most of their time inside areas of large intensity.

Any smoothly varying electric field with a zero-crossing will produce a region of darkness which can be exploited to facilitate dark (blue-detuned) trapping [179]. Laguerre-Gauss (LG) and Bessel beam shapes are two obvious classes of trap as they both exhibit field nulls, but they are limited (in simple cases) to only trapping in two planes, namely those in the transverse plane (x,y), and require something akin to a light-sheet potential in order to achieve 3 dimensional trapping. In Lee et al. [180], four light sheets are combined to create an inverted pyramid that forms a dark trap with gravity confining along the last axis. The optical pipe [181] uses an LG mode to produce a hollow beam which can be used to guide atoms or trap with the addition of a magnetic quadrupole along the length of the pipe. Conical refraction [182] generates a region of darkness known as the Poggendorff dark ring which is a good candidate for dark ring trapping [183, 184], with potential extension to 3D trapping [185]. This is an example of a broader class of 3D dark traps known as optical bottle beams, introduced by Arlt and Padgett [186]. These can be generated in a variety of different methods [187], including conical refraction [183], the interference of multiple gaussian beams [188], holographic shaping with an SLM [189] or a phase-plate [190, 191]. Optical ferris wheels [192] and other dark traps based on the interference of multiple LG modes [179] that generate lattices in 2 and 3 dimensions have particular use in quantum computing and simulation. Lastly, we can generate blue traps with our FZP technique

---

[2] Strictly this is only true for transitions of the Type-I kind. Blue-detuned MOTs using Type-II transitions are routinely made for molecular systems[177], and recently in ^{87}Rb [178]

described in this chapter, but as we shall see in chapter 6, we can also generate blue traps in a hybrid method that will allow for multiple traps to be generated with the same FZP.

5.1.3 Fourier propagation and computational trap design

Light fields are complex in nature, that is they can be modelled with a field amplitude and associated phase. We shall denote this in the following way;

$$E(x,y) = E_0(x,y)\exp(i\phi(x,y)) \tag{5.2}$$

with field amplitude, E_0 and phase ϕ. Within this work we consider a uniform polarisation across the beam, but relaxing this constraint would be an interesting avenue to pursue, especially given the effects of tight focusing in the non-paraxial regime [193].

We wish to generate a desired "arbitrary" field at a position by controlling the *phase* at another, distinct to beam shaping using amplitude modulation. Put another way, if we want a shaped trap at $z = f$, then at $z = 0$ we want to know what phase to apply to a beam in order for it to interfere (upon propagation) into the desired trap. Changes to the phase (and amplitude) of a field propagate in a way that is modelled well by Helmholtz propagation [194]. This method of field propagation relies heavily on the Fourier transform and use of the optical 'propagator', $\mathcal{H}\left(z\right)$.

We perform our Fourier transform to plane waves in 3D, $(x,y,z) \rightarrow (kx,ky,kz)$. The field at the origin, $E\left(z=0\right)$ is related to the field at a distance z, $E\left(z\right)$, by

$$E\left(z\right) = \mathcal{F}^{-1}\left[\mathcal{H}\left(z\right)\mathcal{F}\left[E\left(0\right)\right]\right] = \mathcal{F}^{-1}\left[e^{ik_z z}\,\mathcal{F}\left[E\left(0\right)\right]\right], \tag{5.3}$$

where we define the propagator $\mathcal{H}\left(z\right) = e^{ik_z z}$ and $k_z = \sqrt{k^2 - k_x^2 - k_y^2}$. Using this relationship we establish a relationship between the fields at two points along a beam's propagation. Transforming between the two is a simple computational task, allowing us to understand what form the beam will need to take a the origin in order to transform into the desired shape at the focus. The means by which light can be moulded into this form are varied.

Methods to affect the transverse phase of light primarily work by changing the path difference of the beam at different transverse positions. Simply this is achieved by varying the thickness of a substrate (e.g. glass, silicon) from location to location across the beam width. These "phase plates" are ubiquitus in optics as a way of generating focii without losing power to absorption [195]. Absorbent plates are not without their uses; being able to make spatial intensity inhomogeneities you can generate vortices [196] and produce solitons [197] in the technique of "phase imprinting".

There are also the class of dynamic phase plates, the spatial light modulators, or SLMs, of which there are a wide variety[198]. Digital micro-mirror devices (or DMDs) are one such modulator, that affect intensity by either reflecting or not reflecting pixels of light. They achieve this by being comprised of many micro-sized mirrors which can be switched to change the angle of reflection [199–201]. There are also SLMs based on nematic liquid crystals (NCSLM). These operate in a similar principle to LCD displays, but instead utilise pixels comprising of liquid crystals which retard light incident upon it by a controlled amount dependent on the orientation of the axis of the crystals, changing the effective index of refraction. NCSLMs can therefore achieve a higher bit depth of phase change, with some state of the art devices allowing some 256 phase levels. The necessity of switching via fields however means that there is dead space around each pixel in the form of wires, etc, to power each crystal - up to 8% of the total area in some basic models. Both types here have pixel sizes that range from 5 µm to 10 µm in dimension. NCSLMs can be made more light-use efficient, as switching a pixel does not require throwing away light as is the case on a DMD. DMDs on the other hand can switch much faster - some state of the art devices reaching several kHz, compared with the NCSLM refresh rate of around a hundred Hz[3].

For SLMs, generating arbitrary patterns by only varying the phase of the incident light is challenging as the required amplitude control has to be achieved artificially. A number of techniques exist to achieve this, of which an extensive review can be found at Ref. [202]. One common method is to force the amplitude at the input into the shape you require and adjust the phase to compensate for this. One such method is the Iterative Fourier Transform Algorithm (IFTA), where the field is propagated back and forth between the target design and the input field many times in order to refine the hologram quality. The IFTA was first proposed by Gerchberg and Saxton [203]. This is improved

---

[3] Comparing commercially available products in the Thorlabs NCSLM series with Texas Instruments DMD chips. SLM technology is still seeing improvement [198].

upon by the work of Pasienski and DeMarco [49] with the mixed region amplitude freedom (MRAF) algorithm. This CGH algorithm uses the IFTA method, but designates regions of the output plane where the resulting amplitude can be wildly different from the target, given its spatial location, usually far removed from the area of interest (e.g. blank space around ring). This prioritises beam shape over power usage, so it is perfectly suited for atomic trapping where the quality of the trap is more important, e.g. potentials used to trap BECs.

Interest in CGH algorithms continues, for example, with the Conjugate minimisation routine [204, 205], and *offset* MRAF [206], which show robustness against the generation of vortices, where GS and MRAF algorithms are not intrinsically resilient.

5.2 Fresnel zone plates

The Fresnel Zone plate is a kind of phase plate, using the physical structure of the plate to encode the phase information. In this way it is not a strict hologram, like those discussed above in section 5.1.3, but shares the same Fourier propagation method of generation and is discussed in similar terms.

The scientist and engineer Augustin-Jean Fresnel originally developed the Fresnel lens in the 1860s as a means of simplifying the design of lenses for use in lighthouses, allowing for thinner, wider lenses that focus more of the light from the source. A typical refractive lens might be 10s of cm thick by the time it is large enough to be useful in a lighthouse setting and impractically heavy, but by cutting annular segments of various size and angle one can maximise the light refracted by using thinner glass segments and prisms. Illustrations of this can be found in figure 5.1 a) and b). This invention is said to have "*saved the lives of thousands of ships*" [207].

The Fresnel zone plate is an extension of this idea. Similar focusing ability is achieved by using alternating opaque and transmissive zones, instead relying on diffraction instead, as seen in figure 5.1 c). 50% of the light is lost in absorption this way, however. Modulating the thickness of the glass is another such way; in a similar fashion of the NCSLMs the path length of light through the glass sets the amount of retardation achieved, as seen in figure 5.1. The efficiency of the resultant pattern is vastly improved by increasing the bit-depth of

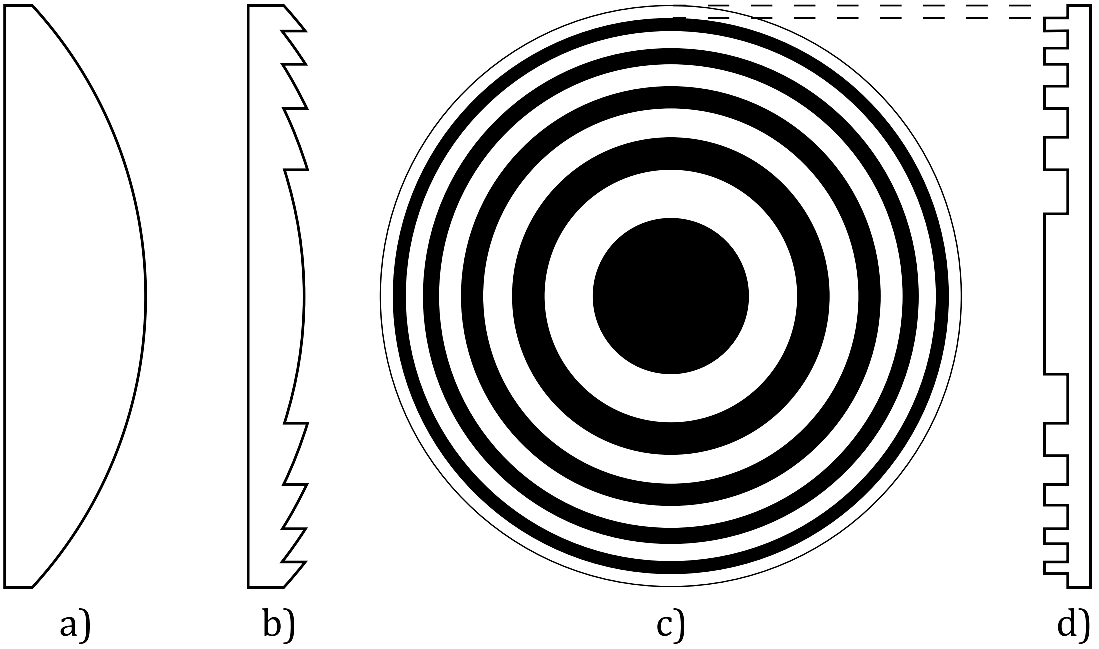

FIGURE 5.1: Examples of Fresnel lenses and zone plates, including: a) Conventional (plano-)convex lens; b) an equivalent Fresnel lens; c) front facing view showing the Fresnel zones as alternating black / white; d) binarised Fresnel zone plate we are designing. Whilst the Fresnel lens is a continuously curved surface, we can recreate the majority of features with purely two zones.

the FZP. FZPs are used extensively in the field of x-rays [208, 209] and optical tweezers [210, 211].

5.2.1 Principle of the Fresnel zone plate

We briefly detail the important aspects for generating a FZP with a target intensity distribution of our choosing. The process is based on the "Angular Spectrum respresentation with propagators" methodology in Refs. [194] and [10], and developed in [61]. This is distinct to the methods detailed above in section 5.1.3, in which extensive computer algorithms are used to generate arbitrary target fields given a known input, often making use of computer intensive interative algorithms to generate a single hologram. Secondly, we do *not* make use of the paraxial approximation $k_z = k - \frac{k_x^2+k_y^2}{2k}$ [10]. In view of these two points, we thus make no approximations about the input beam, or its propagation. The simulation can be seen as an "exact" model of the field between the target and its associated FZP, which is a key aspect to discussing the effects in chapter 6. Some limitations to the simulation exists however, as we do not include effects of polarisation, vector orientation of the field, and the angle at which features propagate in the simulation plane are limited by the pixel dimension.

The process of computationally generating an FZP is shown in Figure 5.2. We first denote a grid of pixels, with each pixel size of around one wavelength, which for us is $\lambda = 1070\,\text{nm}$. The desired output field is then specified upon this grid at the focal plane of the the FZP, which we tailor for the intensity; the phase is left flat. Although this is not done for any particular reason, the phase is not left random as large phase steps will generate vortices or wildly diffracting features we wish to avoid. A phase profile is, however, exploited in the hybrid double-ring trap in section 6.5.1 to generate controlled areas of zero intensity. The field is then propagated "backwards" in space by the desired focal length of the FZP. At this point the phase of the light will inform the shape of our FZP, translating the phase at each point to a corresponding thickness of glass, much like in the case of the Fresnel lens.

The nanofabrication techniques used to generate kinoforms in this way can achieve a limited level of detail in relief, hence sloped and curved features found on the ideal phase pattern (and Fresnel lenses) are not easily manufacturable[4]. It is sufficient to divide the slopes into steps, dividing the π phase shift between zones. In its simplest form, and the one we consider here given its ease of construction, the plate is "binarised" or split into rings of either 0 or π phase shift, much like the optics discussed above. The binarised (or stepped) phase profile is then complete as far as the kinoform generation is concerned.

For testing the simulation, we then apply our input beam (here, a Gaussian beam) and propagate the field forwards again (by the focal distance). Comparisons between the original target and the FZP with propagation can then be made. This is done in Ref. [61].

In essence, even with missing amplitude information (replacing I_{0f} with a gaussian) and flattening the phase profile drastically (binarisation), the output pattern is well suited for atom trapping. The lowest frequency components, which are oft the most important in optical traps (i.e. harmonic confinement), are well reproduced. More information on this can be found in Ref. [62]. These binary FZPs with long focal distances achieve a remarkable accuracy of pattern reproduction, with an RMS error around 3% in the brightest 50% of the

---

[4] This is currently under development.

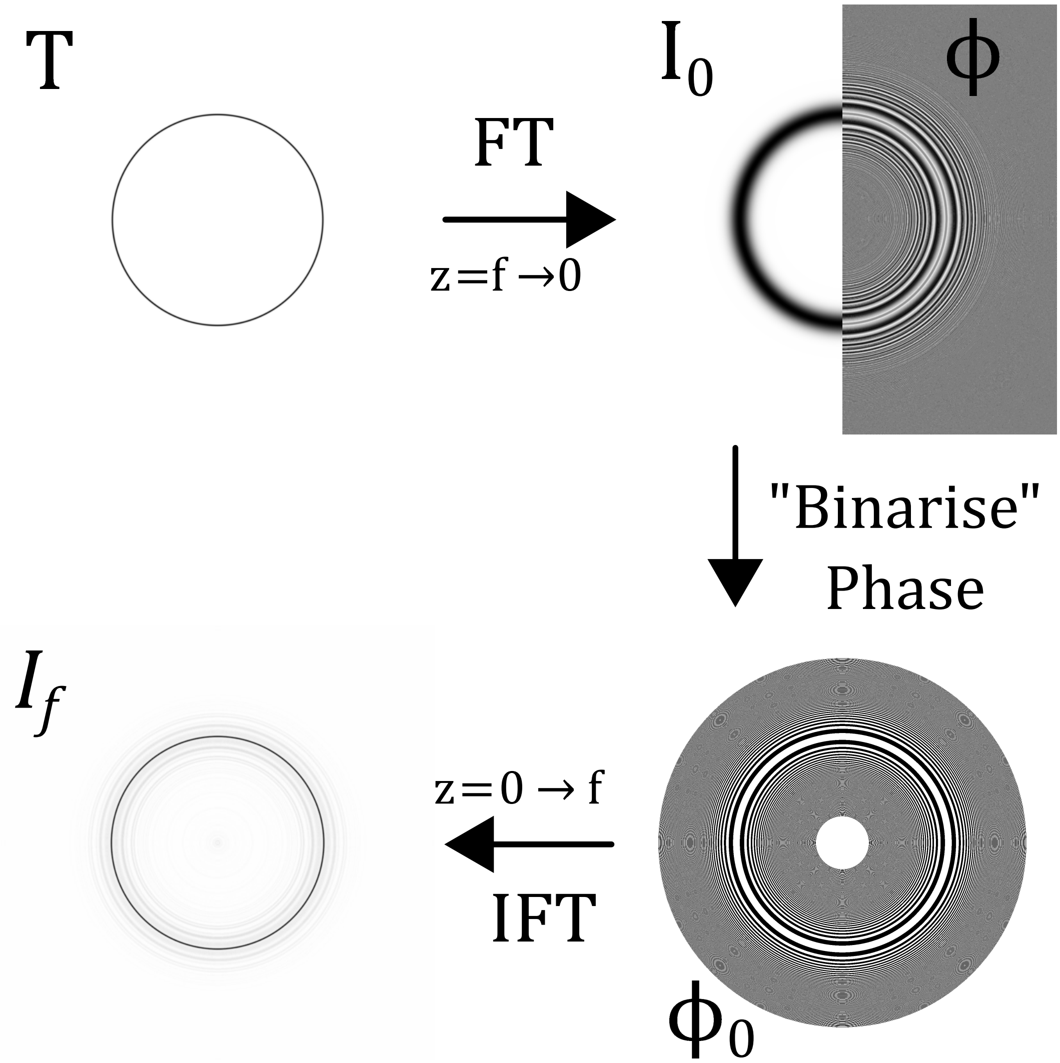

FIGURE 5.2: Principle of generating a Fresnel Zone through simulation - showing the propagation steps and the binarisation. A target field, T is designed, then propagated backwards to the “FZP plane” where the ideal illumination (intensity), I_{-f}, and phase, ϕ_{-f}, are found. This phase is then rounded to the nearest π, forming a binary grating, ϕ_0. This phase, along with a Gaussian illumination, is then then propagated forwards to the target (focal) plane to produce I_0, where performance is evaluated against T.

trap [61], despite not having amplitude shaping of the incident field nor directional information included in the "blazing" of the hologram, i.e. the stepping of the phase-gradient. Allowing for some amplitude freedom and increasing the phase depth (more phase-steps) would allow for better reproduction of the target intensity [61].

Given the limitations in fabrication of the FZP, it is best to consider the effects of changing the input light upon the kinoform, rather than the kinoform itself, given one of the technological attractions to the FZP is its simplicity and cost to manufacture; we wish not to overcomplicate things. In essence, a hybrid system where some other method of light shaping compliments the FZP's focusing perfomance is of interest. We discuss these considerations in greater length in chapter 6.

5.2.2 Experimental Performance

A FZP was manufactured (figure 5.3a) to the specifications given in Henderson et al. [61], which we have now characterised. A full breakdown of the results are published in reference [62]. The essence of the experimental realisation is described below, with attention to the lessons learned from this batch of FZPs. More comprehensive analysis can be found in chapter 6 of the thesis of Henderson [65].

The FZPs themselves are 2 mm in diameter, where 24 of these sit with 2 mm spacing on a 6 × 4 grid. The patterns are etched onto a piece of fused silica substrate (by HOLO/OR) by a combination of photolithography and dry plasma etching. To test performance, the FZP was illuminated with a collimated, 1 mm waist, 1070 nm wavelength beam. The light at the focal plane is then collected by a 10× magnification lens and projected onto a CMOS camera (Cinogy CMOS1201). An image of the ring-trap potential (intensity) is shown in figure 5.3b, for $r = 100\,\mu\text{m}, w_0 = 5\,\mu\text{m}, f = 7\,\text{mm}$, alongside the residuals after subtracting a ring with the same parameters, to highlight the non-contributing light.

The rings were reproduced without noticeable ellipticity, and generally with a similar design radii. The ring width was, however, generally larger than the design. This we attribute to the FZPs being nearly diffraction limited at the tested focal lengths. This design mismatch decreases with focal distance, which is an important factor for our next generation FZPs discussed in chapter 6. Light usage efficiency, that is the amount of light diffracted into

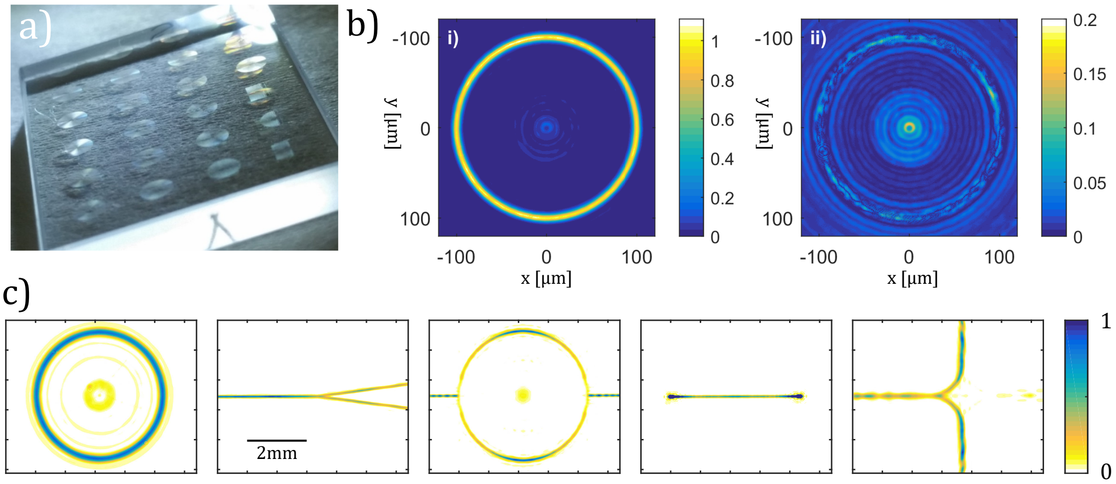

FIGURE 5.3: Experimental realisation of a Fresnel zone plate. a) 24 FZPs etched on sapphire, each 2 mm in diameter. b) $r = 100\,\mu\text{m}$, $w = 5\,\mu\text{m}$, $f = 7\,\text{mm}$ ring trap, showing i) the intensity at the focal plane, ii) residuals from fit with design. c) Examples of other holograms made, plotted with the same transverse scale. Note the irregularities in intensity from the non-cylindrical patterns. Figure adapted from [62]).

the target pattern versus elsewhere, averaged around 30% out of a theoretical maximum of 50% (due to the presence of a virtual focus). This would be greatly improved by being able to *blaze* the zones, or by using a non-binary, i.e. multi-level FZP manufacture technique, which we are pursuing for our next generation of FZPs.

To characterise roughness in the trap, we quantify the error in the brightest 10% of the potential using the root-mean-square (RMS) figure-of-merit [212]. RMS error between design target and realised trap averaged between 3 to 5% - a figure which serves as a worst case as it does not differentiate between errors in the imaging system and the actual target, despite best efforts to minimise these. This figure of error is compatible with atom-guiding [206, 212, 213].

We look now to generating another generation of FZPs, learning from the performance of our FZP designs. One improvement would be the use of an error-correction method, similar to the function of the feedback algorithm for NCSLMs [50, 212]. We detail our "High Numerical Aperture FZP" design in the following chapter - where local changes to the illumination of the FZP make corresponding local changes to the trapping potential.

Chapter 6

High NA Fresnel Zone Plate Simulations

We are able to make Fresnel zone plates (FZPs) with mm scale focal lengths that are effective phase-based light manipulators, recreating target fields with minimal error over the portion of the trapping potential we are most interested in [62]. We have, however, neglected the importance of the incident beam, drawing attention to the fact that illumination with a Gaussian beam, or indeed overfilling the FZP, is not the exact field intensity that the FZP requires in order for it to be able to *exactly* re-create its chosen target. Indeed, as has been shown, targets that divert from cylindrical symmetry, or have sharp features such a line end or 90 degree joins, do not perform well [61].

Our experimental realisation of FZP generated trapping potentials (see [62] and section 5.2.2) led us to realise that smaller focal lengths will allow for finer detail and thus tighter-waisted ring trap potentials. We shall refer to these as high numerical aperture, or "High NA", FZPs given their focusing abilities. There is also another motivation for high NA plates: as the field propagates there is a distance over which the potential remains ring-like in shape as it has not diffracted sufficiently in order to interfere with other parts of the field. This identical-looking geometry, alongside a cylindrical symmetry, allows us to effect change to our incident beam intensity to transform into local changes to the field at the focal plane. Simply put, we can change our "input ring" in such a way that the same change will be reflected at the focus of the plate. This includes both intensity and phase changes. One can therefore imagine doing on-the-fly corrections to intensity errors from the imaging system, for example, using the location of atoms in the ring as a sensor for the light field focused by the FZP..

Here we present various simulations using the Fourier transform method detailed in section 5 for the high numerical aperture plates. In this regime the input requirements are substantially different to those for our previous experimental plates, as the primary goal here is to be able to affect the intensity at the focal plane with simple changes to the input intensity at the FZP. This is done without having to use complex non-linear intensity maps, such as those found in CGH techniques (see section 5.1.3).

6.1 High NA FZP generation and input requirement.

If we want local changes in the input intensity to be reflected by corresponding changes in the trapping potential at the focus of the FZP, then our requirements for the input intensity need to be more stringent. Of particular importance is the spatial distribution of intensity, i.e. its shape.

An illustration of the process is seen in figure 6.1 a), where we generate a high NA FZP with a focal length, f, of 1 mm, a ring radius $r_0 = 500\,\mu\text{m}$, ring width $w_0 = 5\,\mu\text{m}$. The other important aspect in this "hybrid" picture is that the FZP is joined by some other beam-shaping device, such as an SLM. This device is necessary in order to generate the FZP illumination, I_0, required for the target recreation at the focal plane. The details of how this can be achieved experimentally is not important for this work, but a variety of methods to map arbitrary phase and intensity over long distances exist - see section 5.1.3 and references [50, 201, 202, 214]. For our simulation, we assume this input illumination is possible to create, and are more concerned with the manipulation of I_0 using an FZP.

6.1.1 Simulation details

Our simulation is performed on a 2D Cartesian grid, where we have full access to the third axis for beam propagation . The patterns (rings) that we are interested in however are circularly symmetric, so henceforth we will use the conversion to cylindrical polar coordinates in the typical sense, $r = \sqrt{x^2 + y^2}$ and $\theta = \arctan(x, y)$. We will also use x, y to denote the 2D transverse beam direction, and z as the propagation, or axial, direction, along which the beam propagates. The simulation is performed using Wolfram Mathematica with a 4 mega-pixel grid (i.e. a 2048×2048 pixel array).

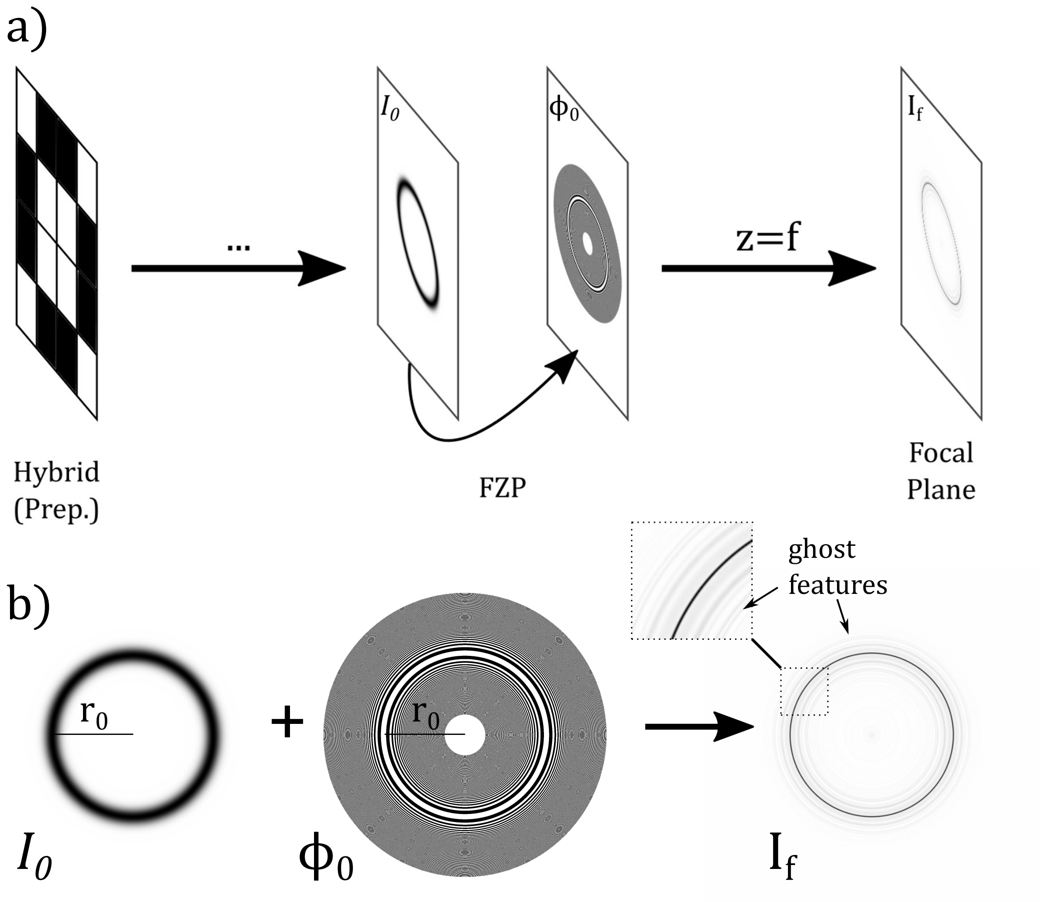

FIGURE 6.1: Hybrid approach to address 1:1 mapping in the "High NA" FZP regime. a) Depiction of experimental process - a "hybrid device" generates the required illumination, I_0, with a flat phase which is applied to the FZP (which imparts spatial phase ϕ_0). Upon propagation to the focal plane generates the potential, I_f, is generated. b) Enlarged images of the simulation. Note the black/white Fresnel zones denote a change of π in phase.

Distinct to the method previously discussed in section 5.2.2, we no longer apply a *general* 1 mm Gaussian beam to all patterns when evaluating performance (the last step on figure 5.2). The intensity we now use is the absolute value squared of the field at the FZP plane, I_0, exactly as generated at the same time as we make the binary ϕ_0 pattern. *Both* of these are then propagated forwards to the focal plane when we evaluate performance.

The target recreations by the high-NA FZP are generally faithful and well performing in simulation. The main ill-effect of the binarisation procedure is the generation of additional rings "ghosting" in the background, seen in figure 6.1 b). A zoomed-in cut of the same ring along the radial direction is shown

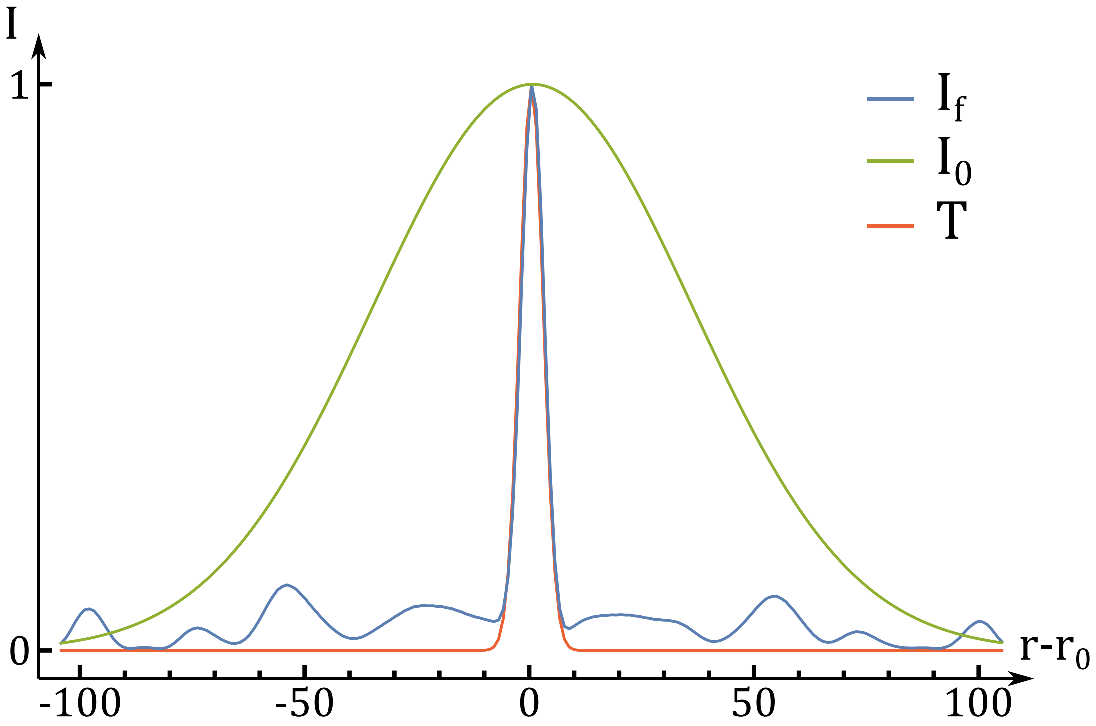

FIGURE 6.2: Zoom in on the ring feature at $r = r_0$ from figure 6.1, showing the radial intensity profile of I_f. The x-axis is centred on r_0 for a ring with radius $r_0 = 500\,\mu\mathrm{m}$. The illumination on the FZP is shown as the broad Gaussian (in green) and is focused down to the profile shown (in blue). The FZP was designed with the target profile shown in red.

in figure 6.2, centred on the ring radius $r = r_0$, showing the biggest ghost features, close to the ring radius. The illumination's ring waist (e^{-2} intensity radius) is around 70 µm and is focused by a factor of 14 to $w_0 = 5\,\mu\mathrm{m}$ at the focal (target) plane. The height of the ghost features here are less than 10% of the peak intensity, which sits at the ring radius. For atom trapping, this is of little concern, as trapping is dominated by the brightest parts of the trap, although we must keep a keen eye on these features so that they do not end up more intense than the geometry we desire.

6.1.2 Input intensity and field overlap

The main difference (and requirement) of the high NA FZP regime compared to "regular" long focal length FZPs is the shape of I_0. In order to affect some 1:1 correspondence in intensity variation some similarity to the target geometry is necessary in the input intensity. In the near-distance, i.e. for plates with high NA, the electric field does not cover enough distance in order to diffract greatly, hence we see some similarity in the shape I_0 to our target pattern.

In the example of the Gaussian ring geometry, for large propagation distances the field begins to interfere constructively in the centre of the pattern, into a large "spike" in intensity. A wide Gaussian illumination will complement this due to cylindrical symmetry, but one can imagine that complicated, non-circular structures will look very different, as evidenced by the poor reconstruction of linear targets in figure 5.3. This indicates proper illumination of higher frequencies becomes more important for faithful target reproduction of more complicated patterns.

For the ring traps, let us consider the high NA regime. Picture two Gaussian spots some distance (e.g. $2r_0$) apart with spot size w_0 (equivalent to the ring width). These spots will expand as per Gaussian optics,

$$w(z) = w_0\sqrt{1+\left(\frac{z}{z_\mathrm{R}}\right)^2}, \tag{6.1}$$

where z_R, the Rayleigh length, is defined in the usual way $z_\mathrm{R} = \pi w_0^2/\lambda$. At the point $w(z_\mathrm{ol}) = r_0$ one finds the "overlap" criterion;

$$z_\mathrm{ol} = z_\mathrm{R}\sqrt{\frac{r_0^2}{w_0^2} - 1}, \tag{6.2}$$

which is the point where the waists of the two spots touch. This is an overly simplistic model, and overlap of the two spot waists begins to occur from the wings of the gaussians well before, but allows some insight into the regime's theoretical size. For a "typical" high-NA ring ($r_0 = 500\,\mu\mathrm{m}$, $w_0 = 5\,\mu\mathrm{m}$, $\lambda = 1.07\,\mu\mathrm{m}$) this distance is around 7.4 mm, but we observe loss of the ring-structure at distances before this. In section 6.2 below, we establish a lower bound on the high NA regime.

6.2 Width of the Central Fresnel Zone

One area of concern, and of interest to the performance of the high NA FZPs, is the width of the largest, or *central*, zone. Set by the radius of curvature of the electric field at $z = 0$ where the FZP is, the central zone is nominally the largest zone, covering the majority of the input intensity. Away from this the field intensity drops but the number of zones increases. There is a trade-off between the amount of information that can be redistributed over these zones. For local intensity mapping we want to have a lot of *phase* information about the particular area of interest stored over the local intensity area - that is to say more zones where the input intensity is highest. One example where this is not exemplified is where the central zone is wider than the radius of the field incident upon it. This effectively pushes the higher frequency components to the fringes of the illumination, which we know are important for traps with fewer artefacts and ghost features. This is less important in multi-stepped (i.e. higher bit depth) FZPs, which intrinsically add more detail in the phase information.

If we want to know over what distance the high NA regime is applicable then the central zone is a good place to look. Too large a central zone and effectively the zone plate does little to no focusing. This would effectively put a lower limit to the range, with z_{ol} from equation 6.2 as the upper limit.

6.2.1 Calculating zone width as a function of propagation distance

The zone width, w_{zone}, for the ring patterns can be approximated in the following way, described in the thesis of Henderson [65]. Let us design a ring pattern at the origin with a radius, r_0 and ring of $1/e^2$ width of w_0. Given the ring design has a Gaussian profile, taking a slice through the ring shows us two Gaussian cross sections at $\pm r_0$. These will expand as per the usual rule for Gaussian beams, found in equation 6.1. At a position z the ring cross sections will then have a new width, w. For small distances, these widths do not intersect and thus one begins to define the realm where intensity could potentially be mapped $1:1$ from input field to target field. The central zone is defined as the portion of the beam at propagation distance z where the curvature lags one half wavelength behind the crest of the beam (in the z-direction). We show this in figure 6.3. Assuming that the beam is far from the Rayleigh length, we can use Pythagoras to approximate w_{zone} as

$$w_{\mathrm{zone}} = \sqrt{z^2 - \left(z - \frac{\lambda}{2}\right)^2} = \sqrt{z\lambda - \frac{\lambda^2}{4}}, \tag{6.3}$$

and dividing the two together to express the zone width as a function of the

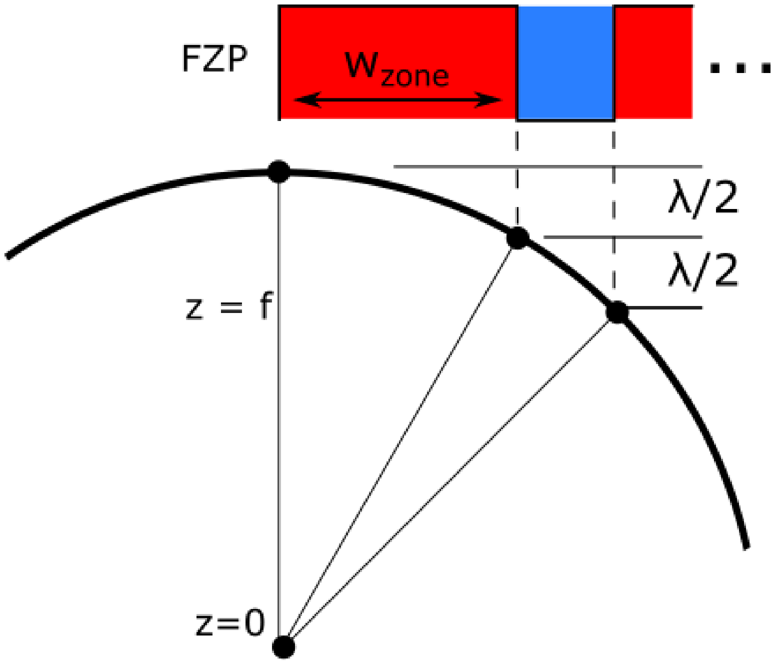

FIGURE 6.3: The width of the central zone (w_{zone}) is calculated this way. We pick some distance $z = f$ from the focus (i.e. the focal plane of the FZP) and find the point where the beam curvature is $\lambda/2$ from the centre of the Gaussian in the propagation direction, z. w_{zone} is then the transverse distance from this point. Successive zones can also be calculated this way. in 6.7 we replace the propagation distance f with the radius of curvature for a Gaussian beam.

incoming beam, and implementing the given assumptions, $z \gg z_{\text{R}}$ and $z \gg \lambda$,

$$\frac{w_{\text{zone}}}{w} = \frac{\sqrt{z\lambda - \frac{\lambda^2}{4}}}{w_0\sqrt{1 + \left(\frac{z}{z_{\text{R}}}\right)^2}} \tag{6.4}$$

$$\approx \frac{\sqrt{\lambda z}}{w_0 \frac{z}{z_{\text{R}}}} = \frac{\pi w_0}{\sqrt{\lambda z}}, \tag{6.5}$$

which is effectively valid for long focal length FZPs. We see that longer focal lengths will make this value small, meaning more zones are illuminated within the waist of the beam. Equation 6.5 may be oversimplified for FZPs which have the ultra-short focal lengths in question for local intensity mapping and we would like to know how quickly the assumption $z \gg z_{\text{R}}$ breaks down.

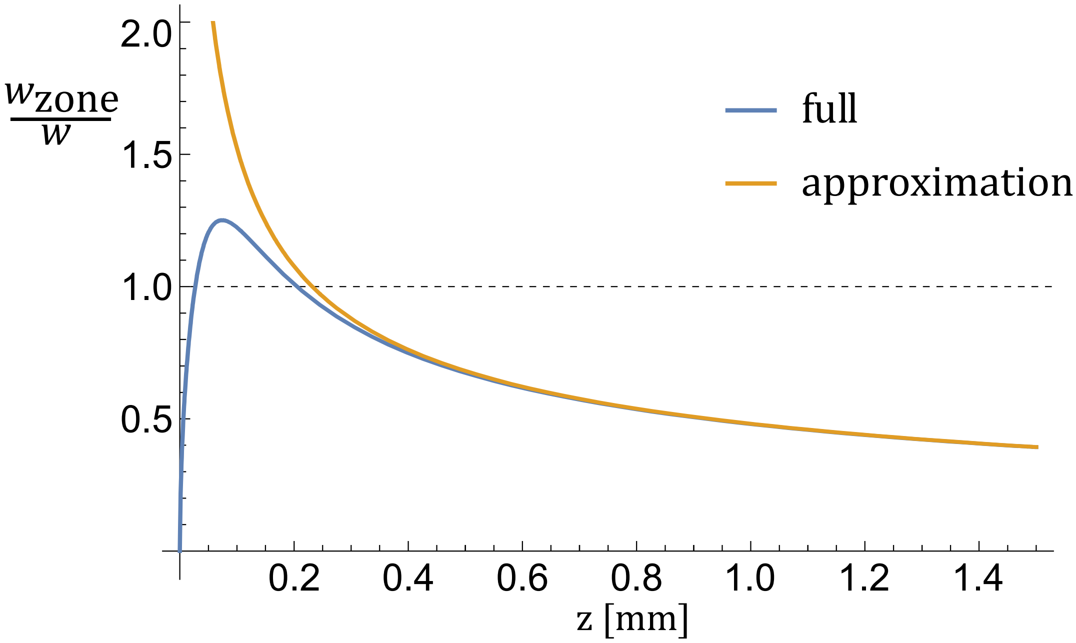

FIGURE 6.4: The ratio of the central zone to the width of a Gaussian beam of the same width. We plot both the full (equation 6.4) and approximate (equation 6.5) versions. To first order (i.e. $f \gg \lambda$) the full shortened approximation holds. As it turns out in section 6.2.2 the full version is incorrect, as it assumes spherical wavefronts.

Figure 6.4 shows a plot of the full and approximation cases, equations 6.4 and 6.5 respectively, for a 1064 nm beam with a waist of $w_0 = 5\,\mu\text{m}$. First to note is the vertical scale; the zone width becomes larger than the beam width for short propagation distances. In the case of the approximation the zone width then carries on to infinity as $z \to 0$, whereas dropping the $z \gg z_{\text{R}}$ assumption we see the zone size return to nothing as the beam narrows. For a 5 µm waist ring there is a 1% difference between the two models at a propagation distance around 440 µm. We see that the full simulation here is actually invalid when we include the radius of curvature of the field, as below in section 6.2.2.

6.2.2 Radius Of Curvature

The above calculation assumes the beam's radius of curvature is the same as its propagation distance, i.e. that the beam has spherical wavefronts. The beam's radius of curvature, $R(z)$ is given in the usual way,

$$R(z) = z\left(1 + \left(\frac{z_R}{z}\right)^2\right), \tag{6.6}$$

which shows that for long propagation distances, equation 6.6 reduces to $R \approx z$, and thus the spherical front approximation is appropriate. Close to the Rayleigh length, however, this is no longer true, and at the focus the curvature is effectively infinite as the wavefront is flat. Again, being careful in our domain of small focal distances we wish to investigate if this knowledge affects the design of our plates.

We will proceed as we did before for equation 6.3, but replace our expression for z with $R(z)$. The zone width expression then becomes

$$\begin{aligned} w_{\text{zone}} &= \sqrt{R(z)^2 - \left(R(z) - \frac{\lambda}{2}\right)^2} \\ &= \sqrt{z\lambda + \frac{z_R^2\lambda}{z} - \frac{\lambda^2}{4}} \\ &= \sqrt{\frac{\pi^2 w_0^2}{\lambda z} + z\lambda - \frac{\lambda^2}{4}}, \end{aligned} \tag{6.7}$$

which is the same form as equation 6.4 but with an additional $1/z$ term within the root. If we then divide through by the beam waist again we obtain

$$\begin{aligned} \frac{w_{\text{zone}}}{w} &= \frac{\sqrt{z\lambda + \frac{z_R^2\lambda}{z} - \frac{\lambda^2}{4}}}{w_0\sqrt{1 + \left(\frac{z}{z_R}\right)^2}} \\ &= \frac{\sqrt{z\lambda\left(1 + \frac{z_R^2\lambda}{z}\right) - \frac{\lambda^2}{4}}}{w_0\sqrt{1 + \left(\frac{z}{z_R}\right)^2}}, \end{aligned} \tag{6.8}$$

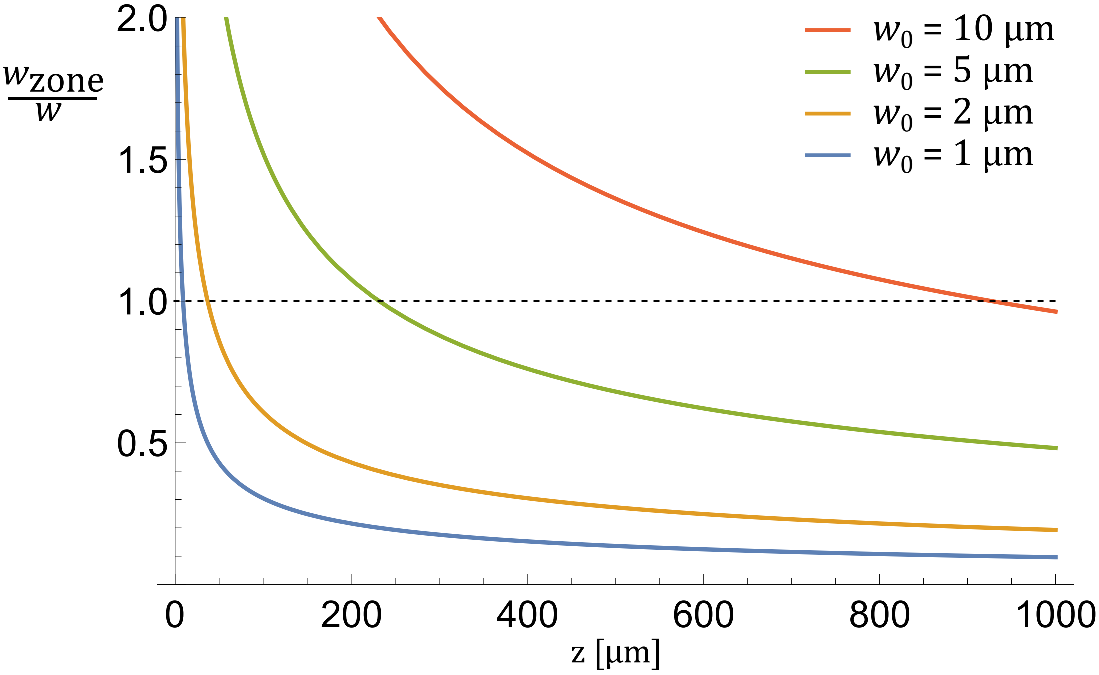

FIGURE 6.5: Ratio of beam waist to central zone width for rings of various width, w_0, calculated with equation 6.6 which includes the Gaussian beam radius of curvature. Where the ratio $w_{\text{zone}}/w = 1$ the FZP does little to no focusing, and we can set this as a lower bound on our high NA regime. We denote this as z_{LZ} in equation 6.10.

where we again neglect the λ^2 term as we assume $\lambda \ll z$, in which case we can reduce further;

$$\begin{aligned} &\approx \frac{\sqrt{z\lambda}}{w_0} \frac{\sqrt{1+\left(\frac{z_R}{z}\right)^2}}{\sqrt{1+\left(\frac{z}{z_R}\right)^2}} \\ &= \frac{\sqrt{z\lambda}}{w_0} \frac{z_R}{z} \\ &= \frac{\pi w_0}{\sqrt{\lambda z}}, \end{aligned} \tag{6.9}$$

where we do, in fact, return the same form as equation 6.5. The assumption that we must be far from the Rayleigh range for this method to work, therefore, is not necessary. For equation 6.9 to be valid we only require that length-scales in z (i.e. the design focal length f) and w_0 be order of magnitude greater than the wavelength. We plot this for various ring widths in figure 6.5.

We find that the central zone is larger than the beam waist for propagation distances less than z_{LZ}, given by setting equation 6.9 to 1, where

$$z_{LZ} = \frac{\pi^2 w_0^2}{\lambda}, \tag{6.10}$$

which for a $w_0 = 5\,\mu\text{m}$ ring is $232\,\mu\text{m}$.

With this calculation we establish the "working area" in which we deem our "High NA FZP" to work. We see that at extremely short focal distances ($z \ll z_{LZ}$) the illuminating intensity is moreorless 1:1 with the target - which is reflected in figure 6.5 as the ratio of widths $w_{\text{zone}}/w > 1$ for small z. As the focal length grows toward infinity, then further zones fall within in illuminating area. The upper limit on the regime is where the local intensity mapping fails - usually because the intensity requirement at the FZP is no longer the ring shape useful for these applications and instead is a high peak centred on $r = 0$. Some explanations for the appearence of this have been offered for this already, which we have discussed previously in the overlap calculation in section 6.1.2, as well as in the work of Henderson et al. [62, 65], as light constructively interferes at $r = 0$. Breakdown occurs somewhere before $f = z_{\text{ol}}$ (as in equation 6.1) where individual components of the Gaussian ring begin to add constructively in the centre region. Calculating z_{ol} for the waists in the figure 6.5, $w_0 = 1, 2, 5, 10$, gives $z_{\text{ol}} = 1.5, 2.9, 7.3,$ and 14.7mm respectively.

6.3 Performance of high-NA FZPs

Having established a working area, we are now interested in the performance of the high NA plates. We choose to measure this by the RMS error, defined as $\epsilon_{RMS} = \sqrt{\frac{1}{N}\Sigma\left(\Delta I\right)^2}$, where ΔI denotes the difference in intensities from the final ring pattern and the target ring. The target ring, T in figure 5.2, is scaled by the final intensity so that the non-Gaussian features dominate the residuals. We report the RMS error along a cut in the radial direction, from centre to edge of the simulation error, as the pattern is relatively equal in error around the azimuth. These are plotted in figure 6.6 for a $10\,\mu\text{m}$ and $5\,\mu\text{m}$ width ring.

The thinner ring has an error we expect for a simulated FZP of 1-2%, however the wider ring is interestingly poor in performance, with up to 5% RMS error compared to the target. This may be in part to features aliasing from the

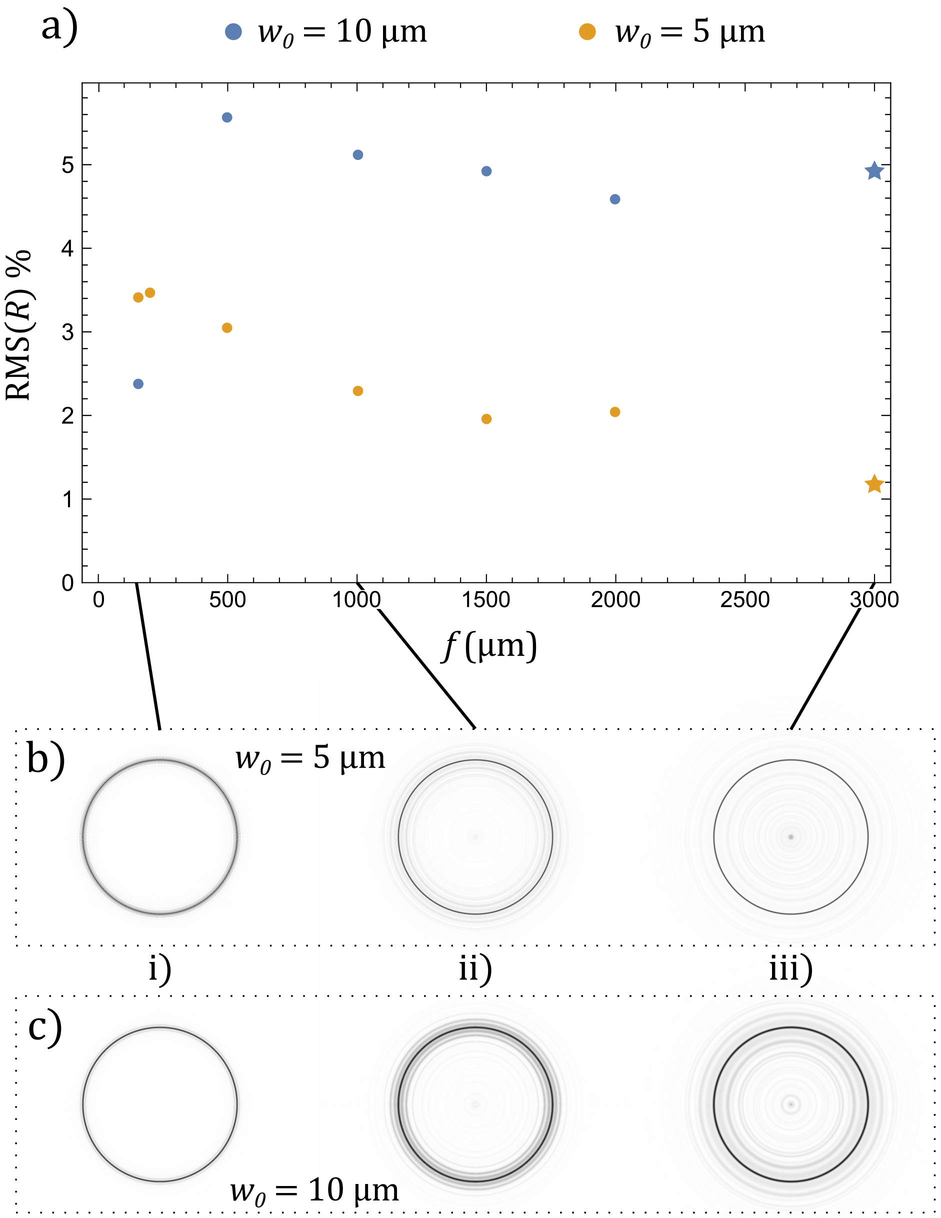

FIGURE 6.6: Simulation of the performance of a $r_0 = 500$ µm, $w_0 = 5$ µm and $w_0 = 10$ µm ring for various focal lengths. a) RMS error along the radial direction. b–c), snapshots of the rings at focal lengths of i) 150 µm, ii) 1000 µm and iii) 3000 µm, for $w_0 = 5$ µm and $w_0 = 10$ µm respectively. The starred RMS values at 3000 µm exclude the central peak which obscures the Gaussian fit and dominate the error.

grid dimension (1 px = 1 µm). Simulations with a finer grid spacing may help discern if this is true.

The plates with longer focal lengths begin to exhibit a spike in the centre of the ring, which can be seen in figure 6.6 b) in the centre of the rings, growing brighter with increasing focal length, f. The starred points on figure 6.6 omit this central peak (around 50 px from the centre) when calculating the RMS error as they would otherwise dominate the error. This is known [61], and we theorise it is due to non-diffracted light. The disappearance at shorter focal lengths indicates our overlap picture may be accurate, as there has not been enough distance for substantial mixing of the features from different locations of the FZP. There is some difference between the two ring widths as well, as sharper features performing better over plotted values. There is some concern that the centre-peaking occurs quicker for thin rings than for wider ones.

6.4 Local Intensity Mapping

To demonstrate local intensity mapping, we will try simulating the application of illuminating “spots” of varying size and shape to a FZP and observe their evolution at the focal plane. The intention here is that illuminating local structures of the FZP that follow the outline of the zones will illuminate the corresponding features of the intended intensity pattern. Put another way, if we add a feature around the ring in the input intensity, this should have the corresponding feature at the focus. This would allow portions of the ring to be illuminated by themselves or we could design input beams which fix resultant intensity imbalances around the ring, or spots / blemishes in the pattern simply by locating their position. This ’on-the-fly’ error correction is a powerful tool in our hybrid arrangement, combining the high resolution of the FZP with the dynamic abilities of a spatial light modulator shaping the intensity illuminating the FZP.

6.4.1 Input beam azimuthal slices

In this section we are interested in adding intensity around the ring, i.e. azimuthal intensity changes. We want to consider how the FZP will focus such a feature, with particular attention to any distortions in the azimuthal direction. We will apply a local illumination in the shape of a “ring segment”, i.e. an annular section of of the ring-illumination. The simplest way to this is to “chop” the input intensity into a section of the full ring, apply it to the FZP and verify performance by propagating it to the designed focal length.

We choose the ring section to have a Gaussian profile around the azimuth, which will prevent the effects of diffraction from sharp intensity features, such as those assocaited with a conventional "cake-wedge" slice. We show a Gaussian slice propagation in figure 6.7. The focusing ability of the plate is evident, as shown by the radial widths of the features pre and post propagation.

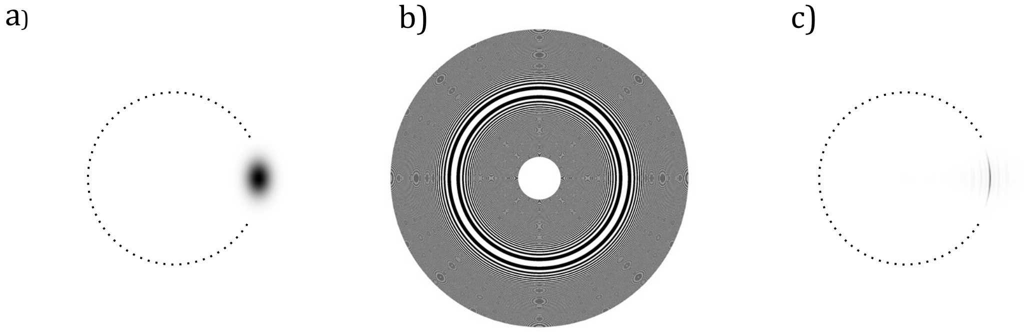

FIGURE 6.7: a) Local intensity feature, applied to a ring trap FZP with $r_0 = 500\,\mu\mathrm{m}$ (dotted line) - a small portion of the ring illumination is used, localised by modulating azimuthally with a Gaussian profile. b) The ring FZP. c) the resulting intensity distribution upon propagation to the focus. Note the ring shape persists and the main effect of the FZP is to cause radial compression of the beam spot incident on the FZP.

Around the azimuth we fit a Gaussian to both the slice width and the illumination width to compare. A comparison is found in figure 6.8. For a range of propagation distances in the high NA regime these widths are essentially the same, hence the illuminated angular range does not change over propagation distances in the high NA regime. This we expect as the FZP does not have any information in the azimuthal direction for the ring pattern owing to its cylindrical geometry. One concern could have been that the lack of confinement, i.e. no zones, would allow the beam to freely expand in that direction, but this seems to be minimal over the focal distances we are concerned with.

6.4.2 Radial Gaussian Spots

Out of interest we now apply small Gaussian "spots" to the FZP, with the intention of highlighting the areas of the zone plate that correspond to particular features of the output. We will do this for particular points along a radius of

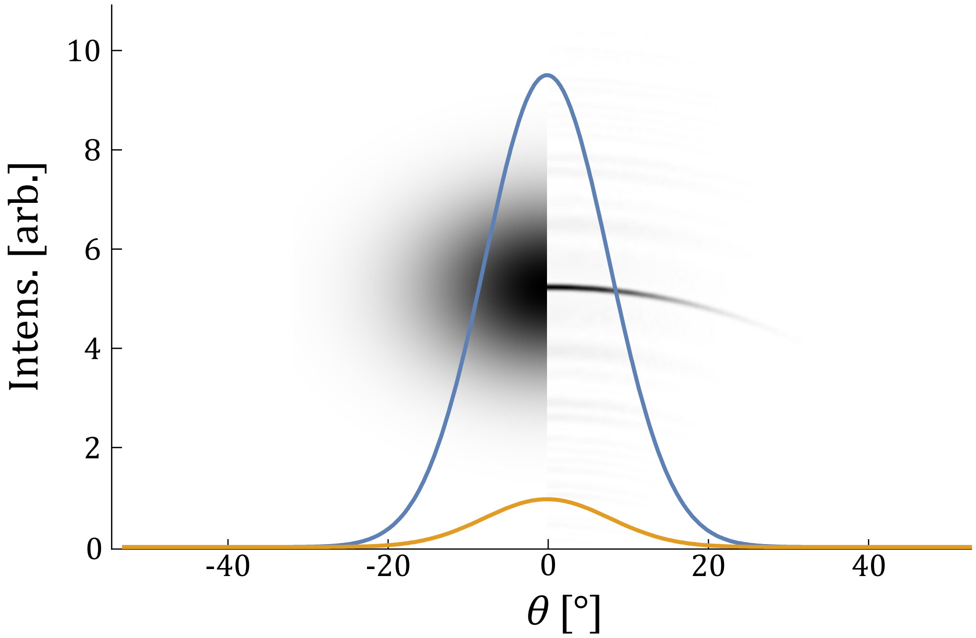

FIGURE 6.8: Intensity plotted over the azimuthal direction, with the simulation in the background for comparison. The Gaussian slice does not change in width, each having an angular width of 15°, over the propagation distance, so spatial features can be preserved in the azimuthal direction. The intensity around the ring (azimuthally)is fitted with a Gaussian both before and after propagation through the plate and they are found to have a ratio of waists approximate to 1, showing that light does not spread around the ring.

the ring, given the zones are cylindrically symmetric. We are interested here in the correlations between the particular "frequency" components of the phase, i.e. the particular zones, and what part of the intensity it illuminates. High NA plates should demonstrate a pixel-to-pixel correspondence, whereas for the longer focal length plates the intensity will either smear out, or be localised on other parts of the plate.

Figure 6.9 shows one such radial grid of spots, for the long focal length ($f = 7\,\mathrm{mm}$, left) and high NA ($f = 1\,\mathrm{mm}$, right) plates, both FZPs generated from the same target ring pattern ($r_0 = 500\,\mu\mathrm{m}$, $w_0 = 5\,\mu\mathrm{m}$, $f = 1\,\mathrm{mm}$). Sections a-k) show a 50 mm Gaussian spot used to illuminate a spot on the FZP at 93 µm increments from the ring centre, shown in the centre column. The dashed line on the left and right denote the position of this illuminating light pre-propagation, as a guide to the eye. Of note in figure 6.9 a), in the long f case the ring is visible in its entirety, whereas in the high NA case no FZP zone is illuminated at all. In the high NA case it is evident in sections c-j) that light has been significantly deflected into the ring, showing how the FZP effectively redirects light into the area of interest. This however illustrates the ghost ring structure more visibly as there is a visible second focus in both cases. A more careful examination of the particular zones or "spatial frequencies" illuminated might explain the position of this.

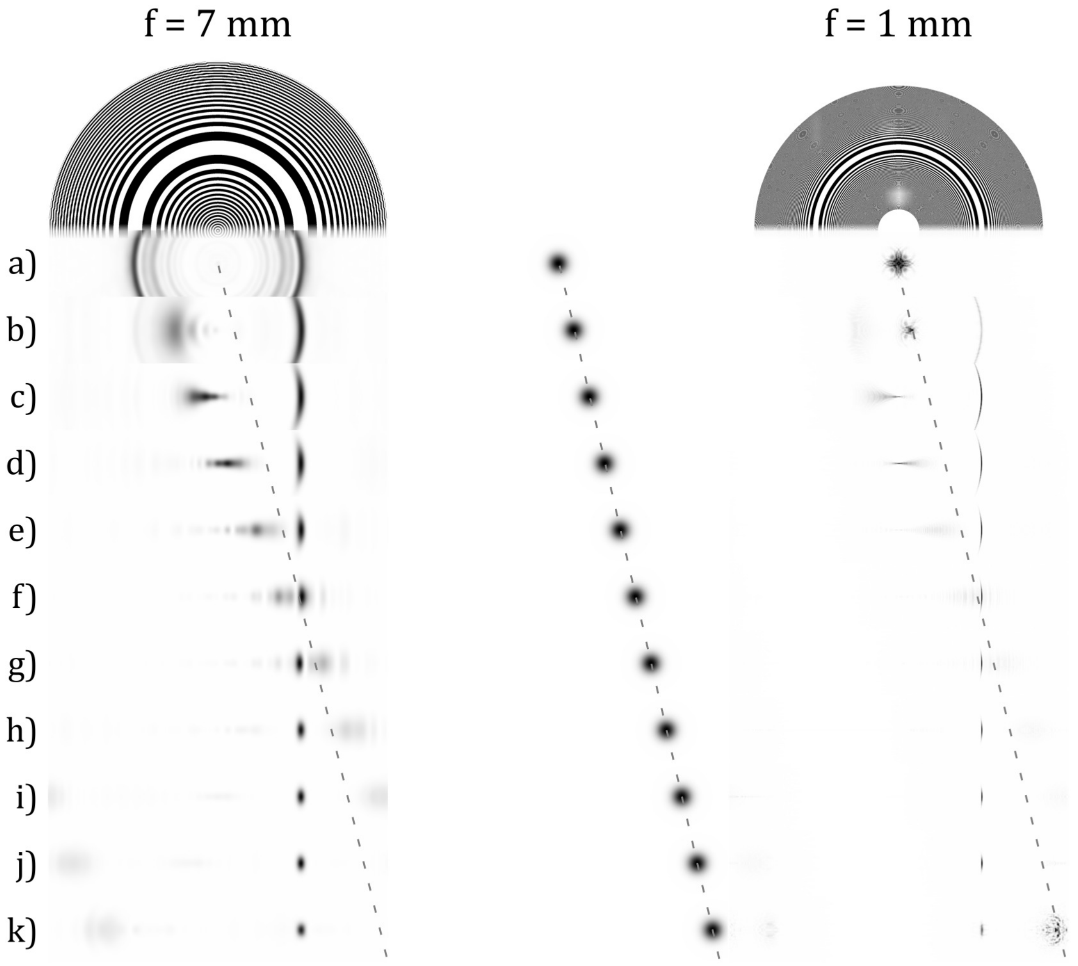

FIGURE 6.9: Two FZPs illuminated by a Gaussian laser beam with beam waist of 50 µm waist beam at different locations along the radial direction, showing the effect of "imperfect" illumination. The two FZPs have the same target ring pattern ($r_0 = 500\,\mu\text{m}$, $w_0 = 5\,\mu\text{m}$, $f = 1\,\text{mm}$), but the right ($f = 1\text{mm}$) plate is an example of our high-NA regime. In the centre the position of the illuminating intensity is shown - equivalently denoted by the dashed lines. The long f plate (left, $f = 7\text{mm}$) has most of its amplitude information stored in the centre - evident by section a), compared to the high NA plate, where it is centred on the ring radius, section f).

6.5 Double Ring trap

As discussed in section 5.1.2 there is a keen interest in trapping atoms in blue detuned beams instead of the more conventional red detuned traps. Blue traps are favourable for trapping scenarios as atoms are attracted to intensity *minima* where atom-light scatter is substantially lower. This scaling allows us to use beams detuned by comparatively smaller amounts (a few nm instead of 100 nm) in the blue.

In the focal plane of the FZP, the electric field for a double ring has the following form in the radial direction;

$$E_{DR} \propto (r - r_0)\exp(-\frac{(r-r_0)^2}{w_0}), \tag{6.11}$$

note the azimuthal symmetry. This is illustrated in figure 6.10 as the dotted (orange) line, alongside an equivalent Gaussian ring profile (blue). The main feature of this field is that the field has a zero crossing at the centre of the Gaussian (due to the radially increasing term). This forces the intensity to also be zero at this point - effectively splitting the ring into two. We then require a method of introducing a zero-crossing in the field with our hybrid technique.

The obvious choice to generate a double ring FZP is to draw the target with the required field and propagate as has been done before. However, in our hybrid regime there is another way to achieve this. By introducing a phase discontinuity of π at the centre of the Gaussian we can force a zero crossing in electric field without also being forced to produce an intensity zero on the input intensity, illustrated in figure 6.10 as the dashed (green) curve. This reduces the complexity of the input requirement on the hybrid device, as we need only apply this change in phase to the input requirement for the Gaussian ring (e.g. with an SLM).

Below we show both the hybrid-generated pattern and the "full" simulation for comparison.

6.5.1 Hybrid (phase-slip) arrangement

To produce a double ring from a field originally intended to make a single ring we need to apply some field to the input intensity that introduces a zero-crossing. Looking at equation 6.11 it is apparent that this is the field of a Gaussian ring, radius r_0, multiplied by that of a linear gradient whose zero-crossing

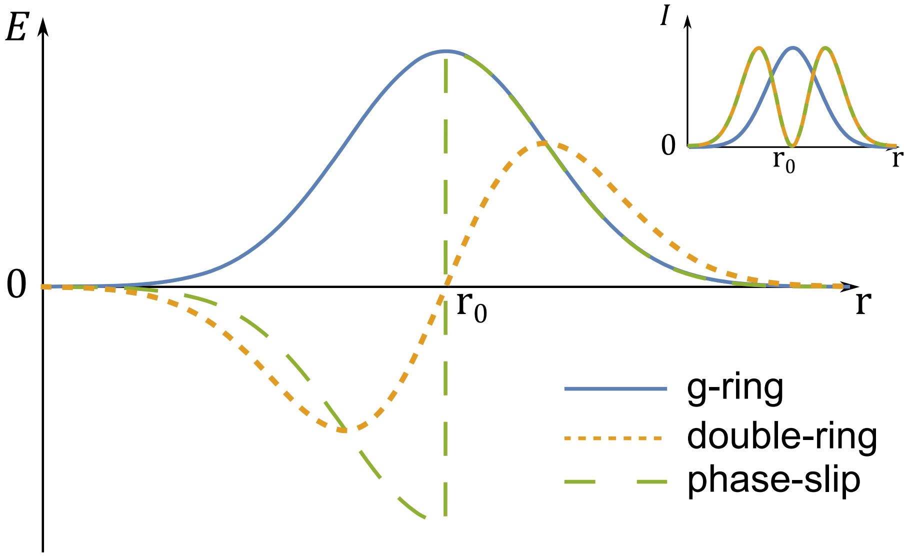

FIGURE 6.10: Real part of the input electric field at the FZP which is then propagated forward to the focal plane. The standard Gaussian ring (blue, solid) is shown alongside the double-ring (orange, dotted) and phase-slip hybrid (green, dashed) fields, which both will generate a double-ring trap, useful for blue-detuned trapping. The corresponding intensities are illustrated in the inset. The phase-slip case is of interest as the same FZP that generates the Gaussian ring can be used to generate a double ring if a hybrid system is used to apply this phase discontinuity at the ring radius, r_0.

is at the ring radius, $E_{lin} = E_0(\vec{r} - r_0)$. The phase associated with this gradient manifests as a phase slip of π at the zero crossing. We can therefore generate a double ring by adding the argument (phase) of the linear field, E_{lin}, to the single-ring input field in our hybrid set-up.

We generate a FZP for a $r_0 = 500\,\mu\text{m}$, $w_0 = 5\,\mu\text{m}$, $f = 1000\,\mu\text{m}$ Gaussian ring trap, as in section 6.1, along with the associated intensity in the high NA regime. We then add the argument of the field E_{lin}. This is then propagated forward, and the resultant field compared with the expected target. The result of this is shown in figure 6.11, in which we see a gap opening up in the ring pattern at r_0.

Figure 6.11 shows the phase-slip field after propagation (I at $z = f$), focusing on a ring segment. The blue and green lines show the intensity and phase respectively of field cut along the horizontal. The background colour shows the phase, whose saturation is modulated by the intensity. Of note is the π-shift in phase between the two rings, this is Figure 6.12 shows the propagation of the same FZP, cut in the radial direction, for the input intensity, a), the

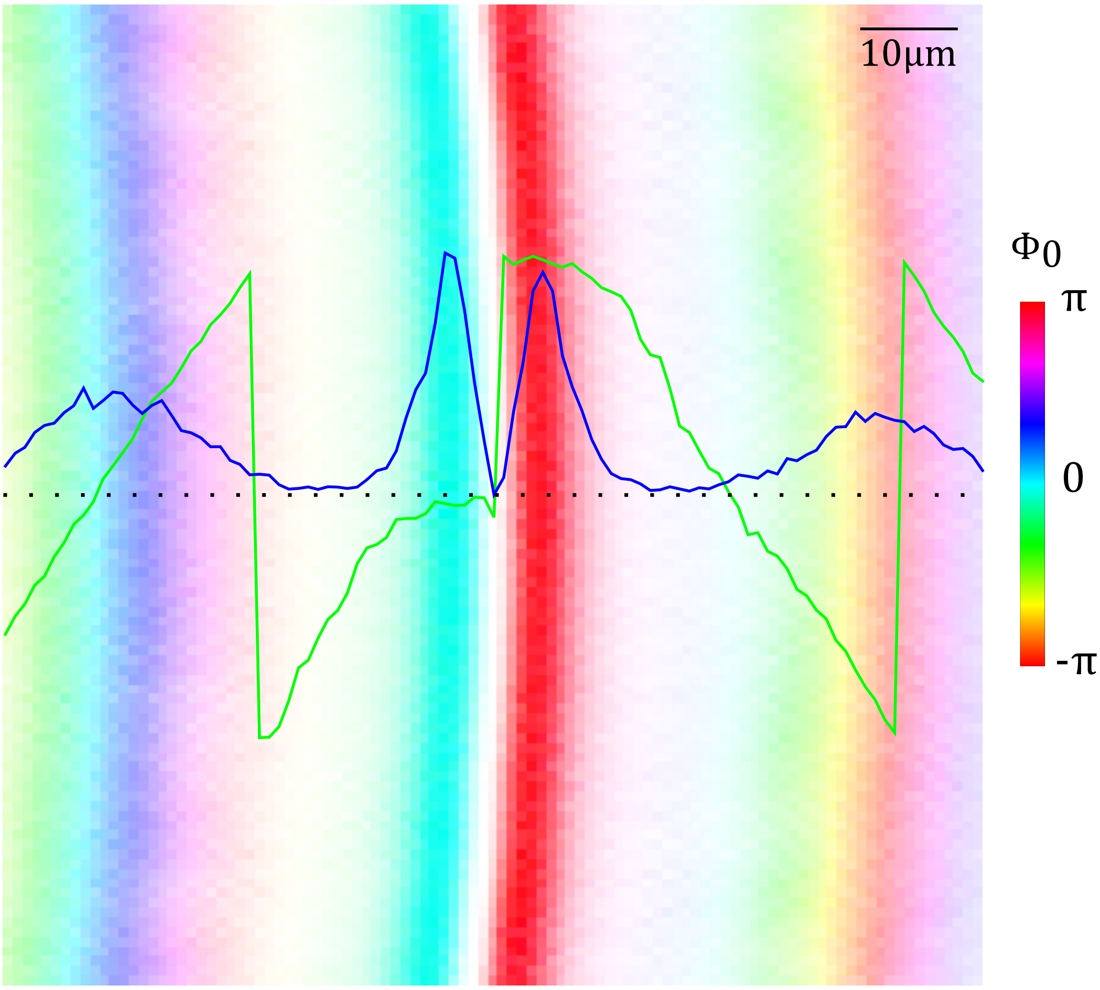

FIGURE 6.11: Double Gaussian ring trap for blue-detuned trapping, generated by applying a phase discontinuity to the input intensity of a single ring FZP of radius $r_0 = 500\,\mu m$, waist $w_0 = 5\,\mu m$, and focal length $f = 1000\,\mu m$. The image focuses on the ring radius, r_0. The blue and green lines show the intensity and the phase of the field respectively along the horizontal line through the centre of the image (i.e. $x = 0$). The background shows a portion of the full 2D simulation, where the false-colour denotes the phase, the saturation of which scales with the intensity of the field.

single-ring (unperturbed) propagation, b), and with the phase-slip applied, c).

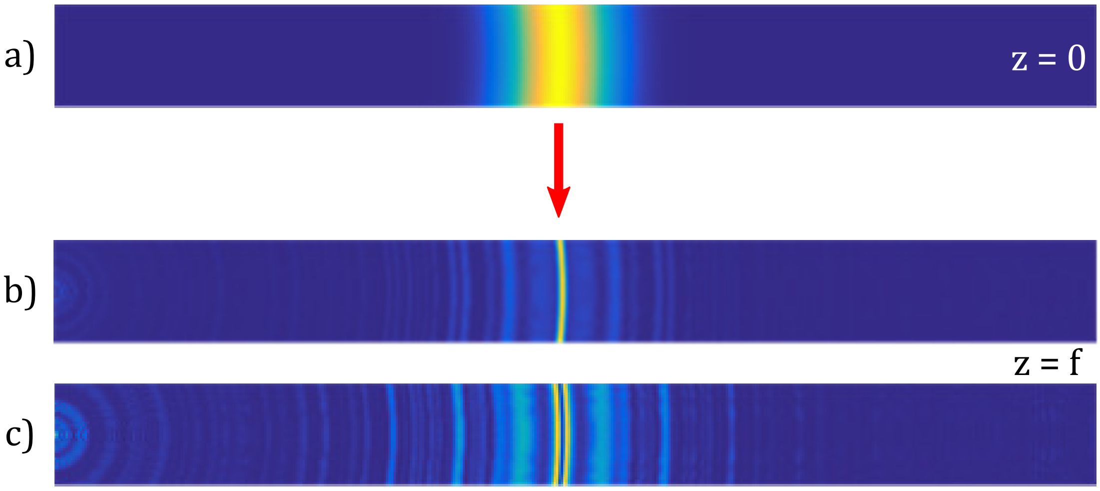

FIGURE 6.12: Radial slice (left is R=0) of the intensity at the FZP ($z = 0$), a), and at the focus, $z = f$ for the single-ring and double ring, b) and c) respectively. The double-ring here is generated by applying a phase slip at the ring radius. With the phase-slip added the ring centre becomes dark, but the noise also increases - most likely due to the incorrect illumination of the FZP, emphasising the lower frequency features.

Note that the design criteria and the resulting trap characteristics of the blue trap are not necessarily similar. We take equation 6.11 for a ring with Gaussian width as above (5 µm, seen in figure 6.11) and square it to find the expression for intensity. The trap frequency, ω_r, scales as the square root of the second derivative of the intensity. For single and double ring traps of equal power and waist, the trapping frequency of the dark trap is $\sqrt{e} \approx 1.65$ times larger than that of the single ring [65].

One of the potential use cases for this method of generation is a single FZP used to generate both red and blue ring traps. Applying the phase slip on the hybrid device would allow the same FZP to generate both geometries without being swapped. Experimental considerations would need to be taken into account regarding the frequency of the beams and how those are generated, but we are confident with careful engineering this could be possible.

6.5.2 Comparison with full simulation

Here we simulate a double ring in full, as detailed in chapter 6, using the dotted (orange) curve from figure 6.10. We generate a double ring in figure 6.13 using the same ring parameters as in section 6.5.1 but applied to equation 6.11.

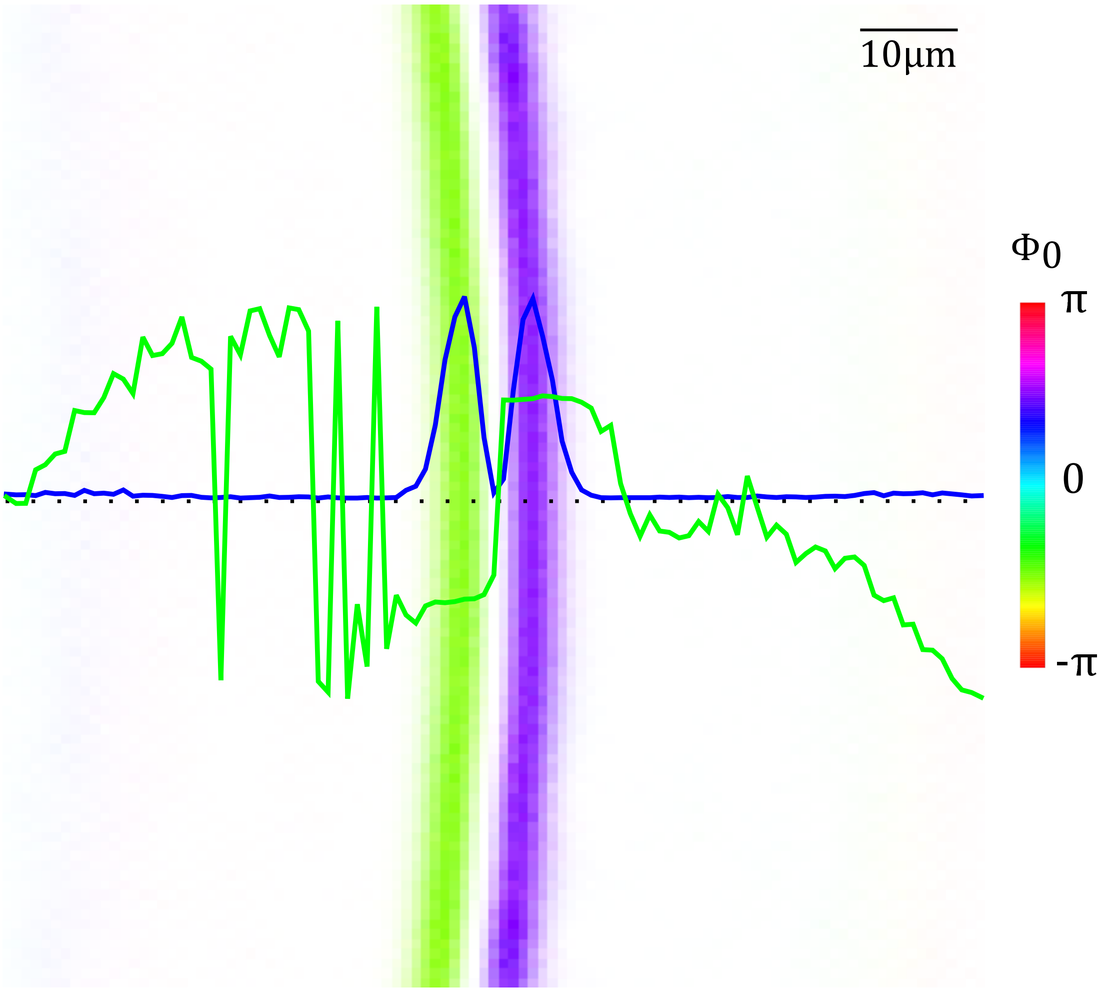

FIGURE 6.13: A double ring trap generated using equation 6.11 to inform the design of a specific FZP design. The design specifications are identical to those of figure 6.11. The image is centred on the ring radius, r_0. The blue and green lines show the intensity and the phase of the field respectively. The false-colour background shows the phase, the saturation scaled with the intensity of the field.

In this way we have generated a tailor made FZP for a double ring pattern. Again we note the phase slip is π over $r = r_0$. The phase over the rings here is much flatter and does not have a slowly varying envelope like figure 6.11. Ghost features are also not present; there are virtually no parasitic ring features for this FZP design.

We measure the light usage efficiency, η, by comparing the intensity in an area $3w_{ring}$ from the ring radius with the intensity found in the rest of the simulation. The full double ring simulation above has n efficiency of $\eta = 0.41$, whereas the phase-slip method the efficiency is $\eta = 0.28$. For comparison the efficiency of a single ring of the same design specification is $\eta = 0.41$, the same as for the full simulation. Note, the best efficiency achievable with a binary FZP is $\eta = 0.5$ due to the presence of a virtual focus [62, 194], as light equally diverges from the FZP phase boundaries as it does converge.

6.5.3 Hybrid simulation with intensity modulation

We also can simulate a hybrid system where we have control over intensity - where we apply both the radial *intensity* and phase of E_{linear} to the FZP. This method is essentially similar to simulating the double ring pattern exactly, i.e. starting with a radial electric field of the shape of equation 6.11, when the two fields are summed together, as can be seen in figure 6.14. The phase profile looks more like the full simulation of 6.13, with flat phases across the widths of the individual rings and a lack of noticeable ghost features around the ring radii. The light usage efficiency of this method is $\eta = 0.40$, an increase of 70% on the phase-slip method. This supports our theory that the ghost features are formed by incorrect illumination of the FZP.

The full simulation and the hybrid with intensity modulation yield the same field at the FZP - the dotted (orange) curve in figure 6.10. The hybrid solution however means that the same FZP could be used to generate a single and a double ring trap with careful manipulation of the trapping light frequency and spatial intensity, with a single π phase step at the ring radius. Whilst the phase slip is enough to generate the required zero-crossing, added intensity shaping is highly beneficial to reduce errors in the final trapping potential. Preference will be dependent on the nature of the hybrid generation, as amplitude modulation inherently results in power loss versus phase-only modulation.

One factor not investigated here is how the two methods will differ in terms of propagation. There is discussion around 3D trapping geometries for blue beams, such as bottle beams [215, 216], where confinement in the propagation axis is also present. We can make some assumptions about the propagation here - in the 'perfect' illumination case the electric field already has the radial intensity component added, which adds a zero in electric field to the beam beforehand, which propagates down into the high NA FZP as seen above, however in the hybrid approach it is uncertain *how* the zero in field will appear. This emergence of the null, and more importantly how it propagates, will inform whether or not the trap can be useful as a 3D trap.

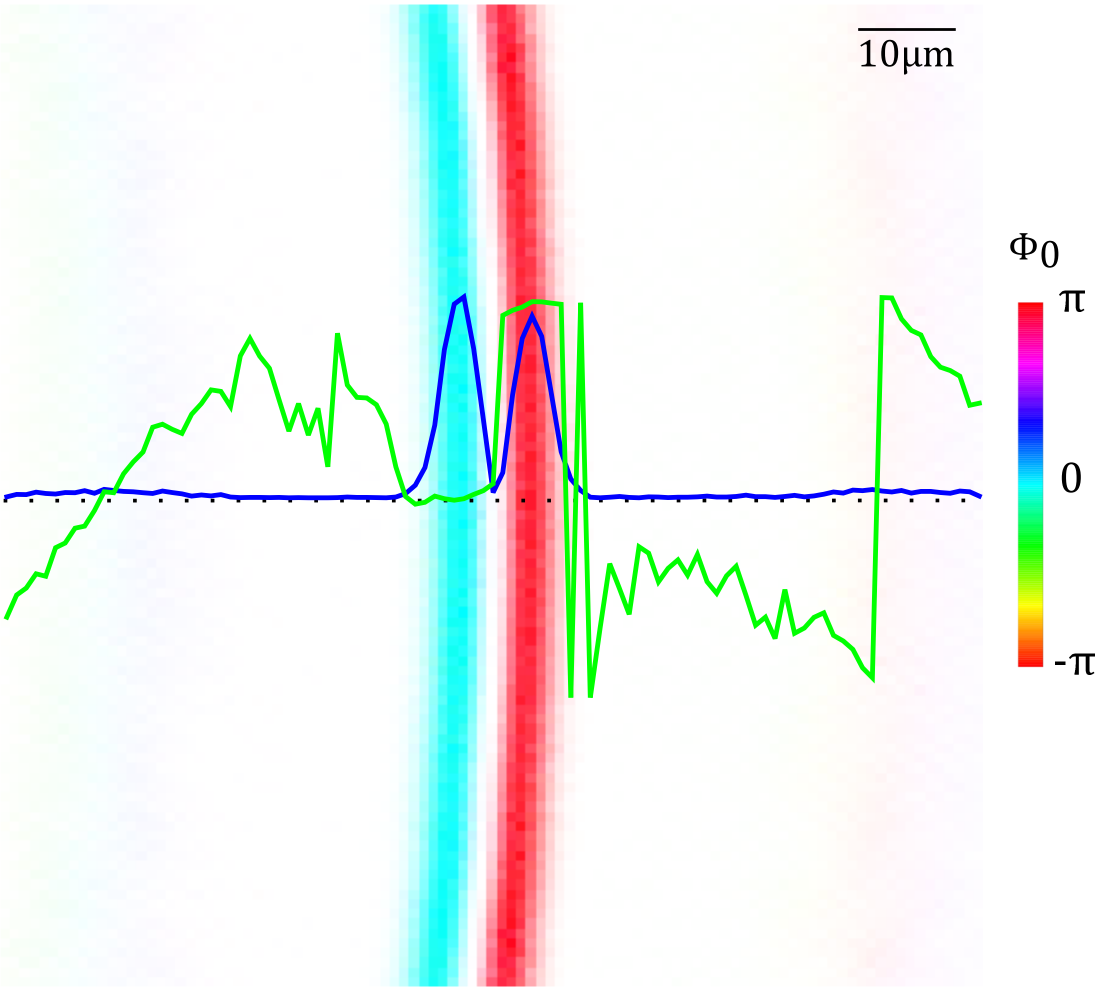

FIGURE 6.14: Hybrid solution with both intensity and phase of radial intensity applied by the hybrid device. The ring design is identical to the previous two figures. Blue and green lines overlaid denote the radial intensity and phase profile along the horizontal.

6.5.4 Ring Lattice

We can apply the hybrid generation method above to the azimuthal direction in order to produce a ring lattice. These are effectively 1D lattices in a circular loop, presenting an experimental way to generate structures with periodic boundary conditions [217]. They are of particular interest to investigations into magnetic flux [218], and atomtronics simulations [219, 220]. Ring lattices may be generated by interfering Laguerre-Gauss modes [192], routinely achieved with SLMs. Here we suggest our hybrid FZP technique can be used to generate ring lattices.

In figure 6.15 we show the simulation of one such ring lattice. Much like the double-ring above the ring lattice can be produced in several ways: a full simulation, the phase-slip or the full-hybrid approach. The full intensity illumination is shown in a), the full simulation FZP is shown in b). Both of these will generate the ring lattice pattern, c), when a) is used to illuminate a single ring FZP (e.g. ϕ_0 in figure 6.1 b), or when b) is illuminated with a single ring intensity (e.g. I_0 in figure 6.1 b).

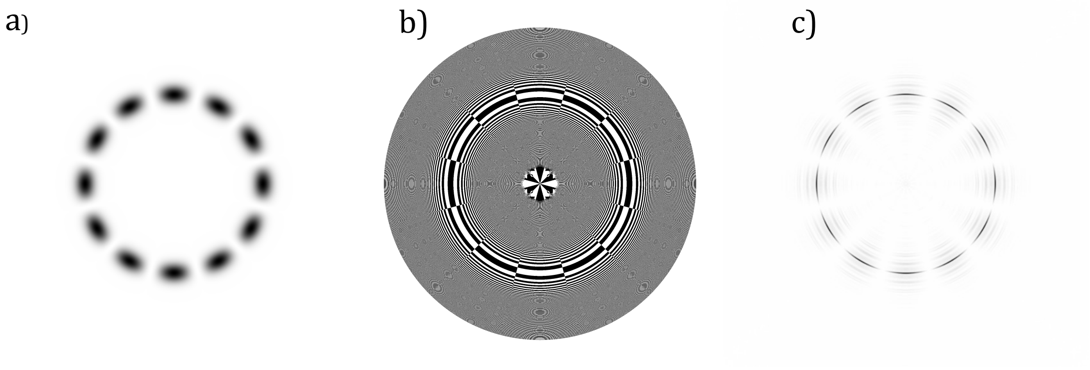

FIGURE 6.15: Image of the ring lattice with hybrid generation. a) The illumination intensity. b) Full simulation FZP for ring lattice. Notice the phase-slips around the azimuth which correspond to intensity nulls. c) intensity at the focal plane. The lattice can be generated purely by illuminating figure 6.1 b) with the illumination, a), or akin to the phase-slip method by illuminating the FZP here, b), with a single ring.

For the hybrid approach we can replace the linear radial term in equation 6.11 with an azimuthal sine wave. A sinusoidal winding around the azimuth will break the ring into segments, the number of which is $2n$ where n is the number of 2π windings, where the sinusoid generates zero-crossings in the field. The associated jump in the phase is evident in the full simulation FZP in b). The FZP phase in b) is the product of the FZP field and sin modulation - the full simulation - which would produce a similar pattern. This example shows that similar to the double-ring example, where hybrid changes in the radial direction perform as expected, hybrid changes around the azimuth also act in the same way as if fully simulated.

6.6 Outlook

These are preliminary studies in the High NA / Hybrid regime. Physical feasibility is yet to be discussed, as hybridisation requires the marriage of multiple devices for one purpose. A SLM / FZP hybrid combination has all the properties required to generate the high NA traps. Further investigations into the propagation in the axial direction (z) would allow us to infer if the beam could focus strongly enough to trap axially in addition to radially. In experiment however, we would like to see this approach used to correct for roughness and imperfections of the resultant ring traps used for guiding matter waves, as this would reduce heating and excitations. The essence of the technique is that we can use the flexible spatial configuration of spatial light modulators with tailored FZPs to bypass meter long focusing setups, instead using the high NA plates to focus what could be, in principle, an input beam with roughly shaped intensity into a diffraction limited smooth beam, with local phase steps at the zone plate transferred into the FZP focal plane.

Chapter 7

Summary and Outlook

7.1 Summary

We shall in turn cover each of the parts of this thesis - the apparatus, interferometry and FZP sections - in turn and give a brief summary.

7.1.1 Apparatus

In this part we described the construction and characterisation of a 2D+ MOT for an apparatus designed to produce BEC. This was worked on between October 2016 and June 2018 by the author.

We first described some atomic physics concepts key to understanding the performance of the MOT: atomic scattering of light, the dipole potential and the magneto-optical effects for atom trapping. The vacuum apparatus itself is a dual-chamber design in order to maintain a low background pressure at the location the BEC will be generated. One novel aspect to this design was the use of fused fibre-splitters to distribute light over the 2D (and test-bed 3D in retro-reflection) MOTs. Overcoming some minor alignment issues, the fibres proved to be sufficient for our purposes. Concerns over the retro-reflected geometry of the 3D MOT when it comes to optical molasses has been expressed - that the shadow of the MOT upon reflection will lead to an unbalanced cooling and hence diminished performance - which we have been unable to verify yet.

The 2D+ MOT is characterised, achieving a flux of $\approx 1 \times 10^8$ atoms s^{-1}. We acknowledge that the full extent of the chamber is not being used, as shown in figure 2.6, where one beam clips the edge of the cell, and where the magnetic field is not ideal for generating a 2D MOT. This can be circumvented with an additional coil in the y-direction, which will extend the region of 0–field in the centre.

The effect of polarisation on the plus beam is an interesting consequence of the geometry we have chosen, where we theorise the retro-reflection of the trapping beams weakens the confinement on that side, leading to the 2D beam having a component of the magnetic field transverse to the atomic velocity. This allows for π transitions to be excited, where the polarisation vector and the magnetic component vector are perfectly aligned. Given the Clebsch-Gordon coefficients mean π transitions cycle slower than σ transitions, this explains why the atomic flux decreases when we use linear polarisation aligned parallel to the magnetic field component.

7.1.2 Sagnac interferometry

In this part we described the elements necessary to construct a Sagnac interferometer using a BEC falling freely under gravity. This was worked on between January 2019 and January 2020 by the author.

In chapter 3 we describe the necessary optics and considerations for the BEC in freefall interferometer. The composite Kapitza-Dirac pulses used allow us to coherently split the condensate into $|\pm 2\hbar k\rangle$ momentum states with high precision. Since the BEC will fall $\approx 2\,\mathrm{mm}$ during interferometry, the local intensity it feels from the Kapitza-Dirac interferometry beam will change as it falls. We calibrate the beam with respect to this by effectively using the split condensate as a beam profiler. Measuring the condensate split fraction as a function of the drop time (for the same pulse length) we can then map the intensity of the beam as a function of position.

The interferometer is sensitive to the axis of gravity. If the beam is misaligned then as the atoms accelerate under gravity a component of the atomic velocity is present in the direction of the splitting beam. This will serve to shift the momentum eigenstate energy levels and make the $|\pm 2\hbar k\rangle$ states no longer degenerate. We account for this by measuring this asymmetry in a crude "tiltmeter". This calibration is not competitive with other quantum tiltmeters based on interferometry, but we estimate a 1 mrad resolution.

In chapter 4 we show some preliminary results on the BEC in freefall interferometer. We show that this configuration scales as the cube of the interferometer time, τ, and report values of phase difference we predict to see for various times and rotation rates. In order to rotate the system we use a piezoelectric stack to launch the table, which we measure with an optical Michelson interferometer. We measure the interference seen when rotating the table and when not, the shots interleaved together over a measurement. Taking the mean and standard error shows no distinguishable change between the rotated and non-rotated shots. More work is needed to ascertain if this is because the contrast of the interferometer is too low, the table rotation rate is not high enough or if some noise source is obscuring the measurement.

7.1.3 High NA Fresnel zone plates

In this part we described a high numerical aperture (high NA) regime for ring traps generated by Fresnel zone plates (FZPs), which allow for local intensity changes on the plate to be reflected at the focal plane. Work began on this project in April 2019 by the author.

In chapter 5 we covered the basic theory behind Fourier-propagation and computational trap design for the FZP. Experimental work has been carried out to characterise the performance of optical dipole traps generated by a variety of FZP patterns, resulting in an average RMS error at the bottom of the trap relevant to storing atoms of roughly 3%.

In chapter 6 we lay the foundation for the high NA regime of FZPs. The key difference in the way we use the FZP in this regime is the way we illuminate the plate - instead of a wide Gaussian beam, we now use the illumination *required* at the plate. In the case of ring trapping this means our illuminating intensity now takes the form of a wider ring of the same mean radius as the ring trap.

In this hybrid regime we are able to address local intensity mapping. Making changes to the ring FZP illumination at the plate are also made at their corresponding position at the focal plane. This technique could be used to correct for roughness in the trap, or to make more exotic traps from the usual ring. In one example we generate a ring lattice by azimuthally changing the light intensity.

Since the illumination must also be generated, for example with an SLM in a hybrid arrangement, it is advantageous to make these changes to the illumination as simple as possible. A phase-slip of π will introduce a zero-crossing the the field, which we can exploit to generate dark ring traps - rings that when used with blue-detuned light can be used as a dark optical trap. These dark rings are of interest because of the inherit lack of spontaneous emission associated with intensity and thereby correspondingly lower atomic heating. We generate a dark ring trap in this phase-slip method and compare with a full dark-ring simulation, commenting on the performance. We note that the hybrid generation is as good in terms of light-usage efficiency as the full simulation when some intensity shaping is also introduced. The merits of each configuration will be dependent on the nature of the hybrid system.

7.2 Outlook

Sagnac interferometry continues to be a challenging subject for atomic physicists. No sensor type currently has a major edge over others, and whilst many authorities on the subject recognise the theoretical advantages that atomic rotation sensing would bring about, in reality that advantage has yet to be seen. The best sensitivity on record with free-space atomic sensors brings it in-line with some of the best commercial fibre-ring and laser gyroscopes available, whilst costing significantly more in price and occupying a much larger volume. Guided interferometry has also yet to demonstrate sensitivities on the same order of magnitude as its free-space cousins, although the groups of Sackett (Virginia, USA) and Boshier (Los Alamos, USA) have experiments that show promising results.

As an outlook for quantum technology, miniaturisation is another key area to be discussed for atom interferometry. Whilst techniques exist to reduce the volume of lasers [221], vacuum apparatus [222] and MOTs [223] the further steps to reduce the volume of the apparatus to produce a BEC presents a challenge - particularly in the sizes of magnetic coils needed for magnetic storage, and the high-power lasers needed to make dipole traps - essential parts to take alkali metals down to BEC temperatures. Chip traps [224] and all optical methods [225] present ways to circumvent these issues.

For our experiment, we would like to bring all three parts of this thesis together and implement a Fresnel trap for rotation sensing in the future. The apparatus described in chapter 2 is being installed into the laboratory, which will reduce dead time and increase optical access - a current barrier to testing our FZP on cold atoms. A second batch of FZPs will be made for testing soon, with some high-NA plates also in consideration. A full documentation of the theory of the high-NA plates is also in progress [226].

Appendix A

Optical Table Layout

The following are included for reference and are the cumulative work of the group at the Strathclyde Experimental Quantum Optics and Photonics group, [63, 64, 66]. Blue and green lines denote $\lambda/2$ and $\lambda/4$ waveplates respectively. Non-polarising beam splitting cubes are denoted in green.

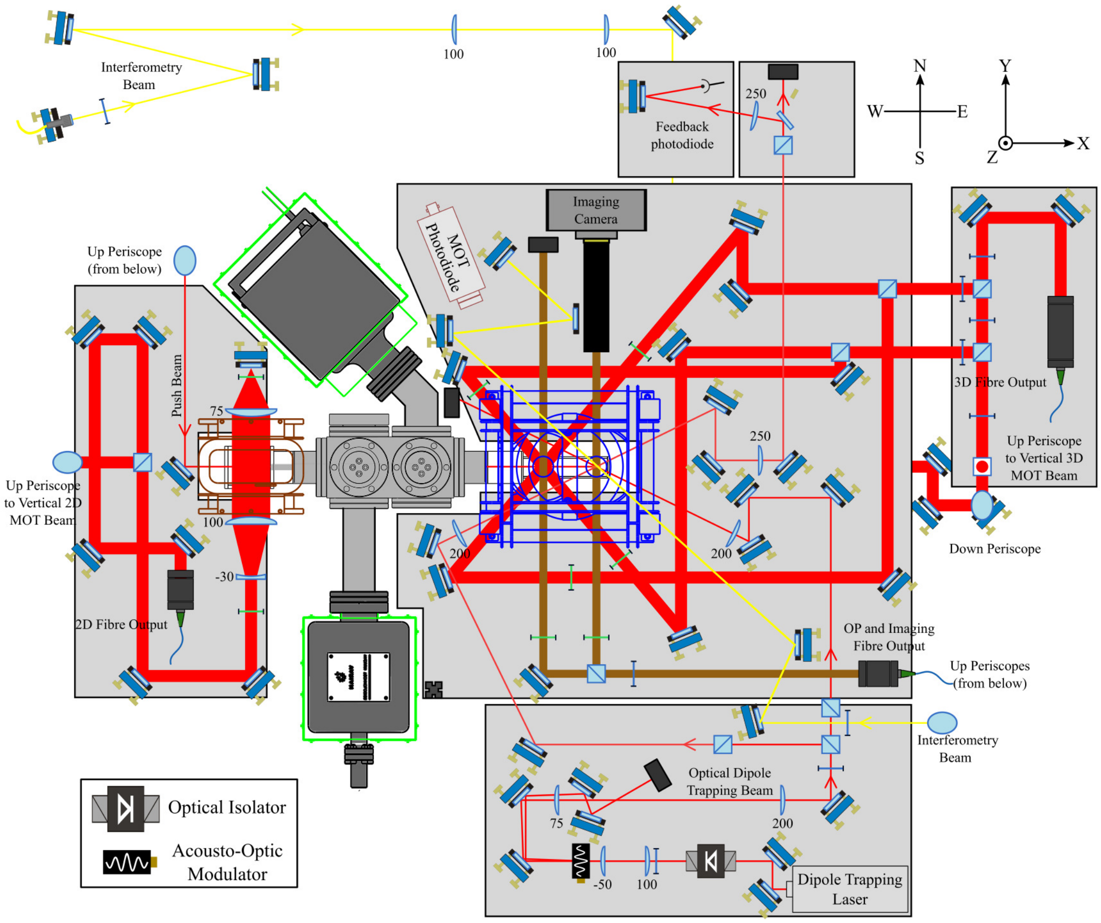

FIGURE A.1: Optics around the vacuum chamber. Figure adapted from page 58 of the thesis of B. Robertson [63]. The yellow interferometry beam denotes the new beam for this work.

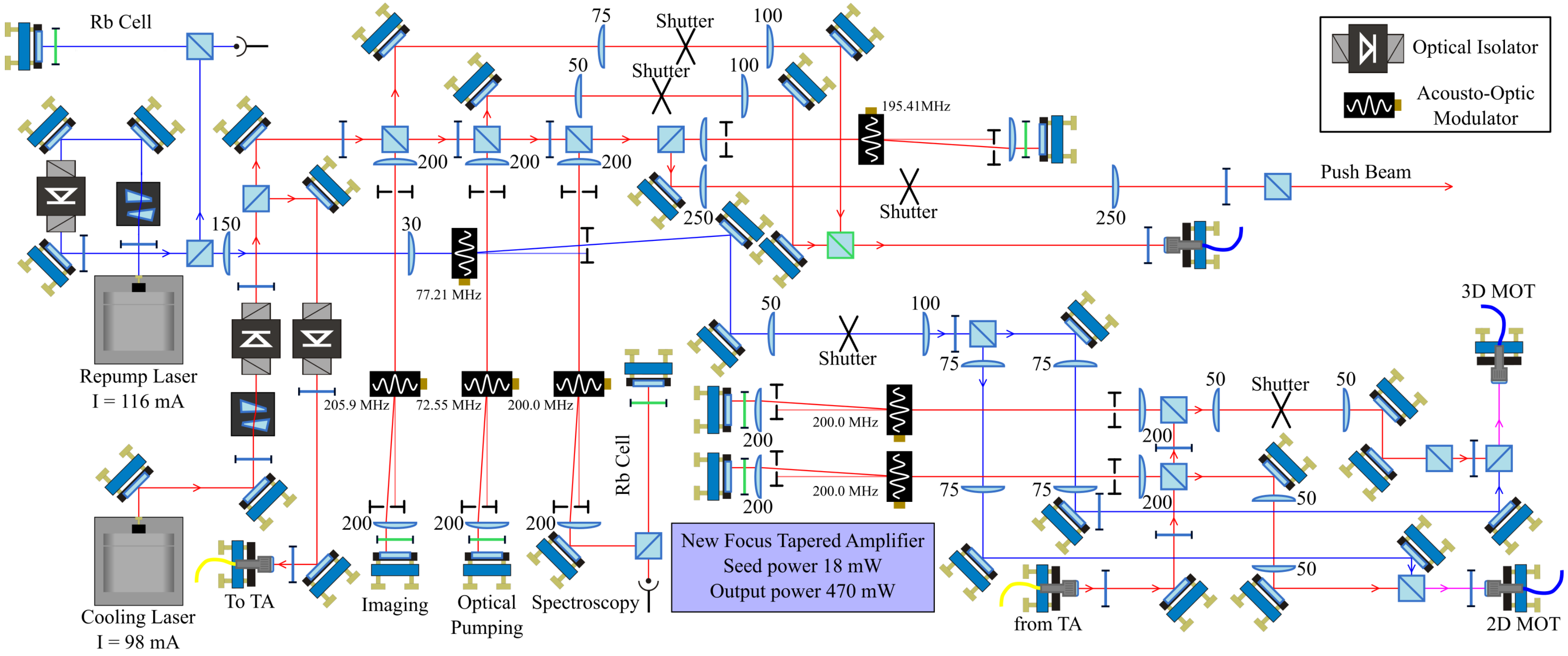

FIGURE A.2: 2D, 3D and repumping optics. Figure adapted from page 56 the thesis of B. Robertson [63].

Bibliography

[1] I. Georgescu and F. Nori, "Quantum technologies: an old new story", Physics World **25**, 16–17 (2012).

[2] A. Acín, I. Bloch, H. Buhrman, T. Calarco, C. Eichler, J. Eisert, D. Esteve, N. Gisin, S. J. Glaser, F. Jelezko, S. Kuhr, M. Lewenstein, M. F. Riedel, P. O. Schmidt, R. Thew, A. Wallraff, I. Walmsley, and F. K. Wilhelm, "The quantum technologies roadmap: a European community view", New Journal of Physics **20**, 080201 (2018).

[3] J. P. Dowling and G. J. Milburn, "Quantum technology: the second quantum revolution", Philosophical Transactions of the Royal Society of London. Series A: Mathematical, Physical and Engineering Sciences **361**, edited by A. G. J. MacFarlane, 1655–1674 (2003).

[4] J. C. Bergquist, S. R. Jefferts, and D. J. Wineland, "Time Measurement at the Millennium", Physics Today **54**, 37–42 (2001).

[5] R. M. Godun, M. B. D'Arcy, G. S. Summy, and K. Burnett, "Prospects for atom interferometry", Contemporary Physics **42**, 77–95 (2001).

[6] K. Bongs, M. Holynski, J. Vovrosh, P. Bouyer, G. Condon, E. Rasel, C. Schubert, W. P. Schleich, and A. Roura, "Taking atom interferometric quantum sensors from the laboratory to real-world applications", Nature Reviews Physics **1**, 731–739 (2019).

[7] Z. Feng, P. Bohleber, S. Ebser, L. Ringena, M. Schmidt, A. Kersting, P. Hopkins, H. Hoffmann, A. Fischer, W. Aeschbach, and M. K. Oberthaler, "Dating glacier ice of the last millennium by quantum technology", Proceedings of the National Academy of Sciences **116**, 8781–8786 (2019).

[8] K. Bongs, V. Boyer, M. A. Cruise, A. Freise, M. Holynski, J. Hughes, A. Kaushik, Y.-H. Lien, A. Niggebaum, M. Perea-Ortiz, P. Petrov, S. Plant, Y. Singh, A. Stabrawa, D. J. Paul, M. Sorel, D. R. S. Cumming, J. H. Marsh, R. W. Bowtell, M. G. Bason, R. P. Beardsley, R. P. Campion, M. J. Brookes, T. Fernholz, T. M. Fromhold, L. Hackermuller, P. Krüger, X. Li, J. O. Maclean,

C. J. Mellor, S. V. Novikov, F. Orucevic, A. W. Rushforth, N. Welch, T. M. Benson, R. D. Wildman, T. Freegarde, M. Himsworth, J. Ruostekoski, P. Smith, A. Tropper, P. F. Griffin, A. S. Arnold, E. Riis, J. E. Hastie, D. Paboeuf, D. C. Parrotta, B. M. Garraway, A. Pasquazi, M. Peccianti, W. Hensinger, E. Potter, A. H. Nizamani, H. Bostock, A. Rodriguez Blanco, G. Sinuco-Leon, I. R. Hill, R. A. Williams, P. Gill, N. Hempler, G. P. A. Malcolm, T. Cross, B. O. Kock, S. Maddox, and P. John, "The UK National Quantum Technologies Hub in sensors and metrology (Keynote Paper)", in Quantum optics, Vol. 9900, edited by J. Stuhler and A. J. Shields, 9 (June 2016), p. 990009.

[9] E. Hecht, *Optics*, 5th (Pearson, 2017), p. 714.

[10] L. Novotny and B. Hecht, *Principles of Nano-Optics* (Cambridge University Press, Cambridge, 2006).

[11] R. Robinett, *Quantum Mechanics* (Oxford University Press, Oxford, 2006).

[12] P. Rodgers, "The double-slit experiment", Physics World **15**, 15–15 (2002).

[13] A. Zeilinger, R. Gähler, C. G. Shull, W. Treimer, and W. Mampe, "Single- and double-slit diffraction of neutrons", Reviews of Modern Physics **60**, 1067–1073 (1988).

[14] A. D. Cronin, J. Schmiedmayer, and D. E. Pritchard, "Optics and interferometry with atoms and molecules", Reviews of Modern Physics **81**, 1051–1129 (2009).

[15] M. Arndt, O. Nairz, J. Vos-Andreae, C. Keller, G. Van Der Zouw, and A. Zellinger, "Wave-particle duality of C60 molecules", Nature **401**, 680–682 (1999).

[16] A. Shayeghi, P. Rieser, G. Richter, U. Sezer, J. H. Rodewald, P. Geyer, T. J. Martinez, and M. Arndt, "Matter-wave interference of a native polypeptide", Nature Communications **11**, 1447 (2020).

[17] S. Chang, "LIGO detects gravitational waves", Physics Today **69**, 14–16 (2016).

[18] R. Weiss, "LIGO and the Discovery of Gravitational Waves, I: Nobel Lecture, December 8, 2017", Annalen der Physik **531**, 1800349 (2018).

[19] R. Anderson, H. R. Bilger, and G. E. Stedman, "'Sagnac' effect: A century of Earth-rotated interferometers", American Journal of Physics **62**, 975–985 (1994).

[20]P. Bouyer, "The centenary of Sagnac effect and its applications: From electromagnetic to matter waves", Gyroscopy and Navigation **5**, 20–26 (2014).

[21]G. Sagnac, "L'éther lumineux démontré par l'effet du vent relatif d'éther dans un interféromètre en rotation uniforme", Comptes Rendus de l'Academie des Sciences **157**, 708–710 (1913).

[22]E. J. Post, "Sagnac Effect", Reviews of Modern Physics **39**, 475–493 (1967).

[23]J. E. Zimmerman and J. E. Mercereau, "Compton Wavelength of Superconducting Electrons", Physical Review Letters **14**, 887–888 (1965).

[24]S. A. Werner, J. L. Staudenmann, and R. Colella, *Effect of Earth's rotation on the quantum mechanical phase of the neutron*, tech. rep. 17 (1979), pp. 1103–1106.

[25]F. Riehle, T. Kisters, A. Witte, J. Helmcke, and C. J. Bordé, *Optical Ramsey spectroscopy in a rotating frame: Sagnac effect in a matter-wave interferometer*, tech. rep. 2 (1991), pp. 177–180.

[26]W. W. Chow, J. Gea-Banacloche, L. M. Pedrotti, V. E. Sanders, W. Schleich, and M. O. Scully, "The ring laser gyro", Reviews of Modern Physics **57**, 61–104 (1985).

[27]H. C. Lefèvre, "The fiber-optic gyroscope: Challenges to become the ultimate rotation-sensing technology", Optical Fiber Technology **19**, 828–832 (2013).

[28]K. U. Schreiber and J.-P. R. Wells, "Invited Review Article: Large ring lasers for rotation sensing", Review of Scientific Instruments **84**, 041101 (2013).

[29]V. M. N. Passaro, A. Cuccovillo, L. Vaiani, M. De Carlo, and C. E. Campanella, "Gyroscope Technology and Applications: A Review in the Industrial Perspective", Sensors **17**, 2284 (2017).

[30]G. E. Stedman, "Ring-laser tests of fundamental physics and geophysics", Reports on Progress in Physics **60**, 615–688 (1997).

[31]P. L. Gould, G. A. Ruff, and D. E. Pritchard, "Diffraction of atoms by light: The near-resonant Kapitza-Dirac effect", Physical Review Letters **56**, 827–830 (1986).

[32]P. Martin, B. Oldaker, A. Miklich, and D. Pritchard, "Bragg scattering of atoms from a standing light wave", Physical Review Letters **60**, 515–518 (1988).

[33]C. Bordé, "Atomic interferometry with internal state labelling", Physics Letters A **140**, 10–12 (1989).

[34]S. Gupta, A. E. Leanhardt, A. D. Cronin, and D. E. Pritchard, "Coherent manipulation of atoms with standing light waves", Comptes Rendus de l'Académie des Sciences - Series IV - Physics **2**, 479–495 (2001).

[35]T. Hensel, S. Loriani, C. Schubert, F. Fitzek, S. Abend, H. Ahlers, J.-N. Siemß, K. Hammerer, E. M. Rasel, and N. Gaaloul, "Inertial sensing with quantum gases: a comparative performance study of condensed versus thermal sources for atom interferometry", The European Physical Journal D **75**, 108 (2021).

[36]H. Müntinga, H. Ahlers, M. Krutzik, A. Wenzlawski, S. Arnold, D. Becker, K. Bongs, H. Dittus, H. Duncker, N. Gaaloul, C. Gherasim, E. Giese, C. Grzeschik, T. W. Hänsch, O. Hellmig, W. Herr, S. Herrmann, E. Kajari, S. Kleinert, C. Lämmerzahl, W. Lewoczko-Adamczyk, J. Malcolm, N. Meyer, R. Nolte, A. Peters, M. Popp, J. Reichel, A. Roura, J. Rudolph, M. Schiemangk, M. Schneider, S. T. Seidel, K. Sengstock, V. Tamma, T. Valenzuela, A. Vogel, R. Walser, T. Wendrich, P. Windpassinger, W. Zeller, T. Van Zoest, W. Ertmer, W. P. Schleich, and E. M. Rasel, "Interferometry with Bose-Einstein condensates in microgravity", Physical Review Letters **110**, 1–5 (2013).

[37]D. Becker, M. D. Lachmann, S. T. Seidel, H. Ahlers, A. N. Dinkelaker, J. Grosse, O. Hellmig, H. Müntinga, V. Schkolnik, T. Wendrich, A. Wenzlawski, B. Weps, R. Corgier, T. Franz, N. Gaaloul, W. Herr, D. Lüdtke, M. Popp, S. Amri, H. Duncker, M. Erbe, A. Kohfeldt, A. Kubelka-Lange, C. Braxmaier, E. Charron, W. Ertmer, M. Krutzik, C. Lämmerzahl, A. Peters, W. P. Schleich, K. Sengstock, R. Walser, A. Wicht, P. Windpassinger, and E. M. Rasel, "Space-borne Bose–Einstein condensation for precision interferometry", Nature **562**, 391–395 (2018).

[38]T. L. Gustavson, P. Bouyer, and M. A. Kasevich, "Precision rotation measurements with an atom interferometer gyroscope", Physical Review Letters **78**, 2046–2049 (1997).

[39]T. L. Gustavson, A. Landragin, and M. A. Kasevich, "Rotation sensing with a dual atom-interferometer Sagnac gyroscope", Classical and Quantum Gravity **17**, 2385–2398 (2000).

[40]I. Dutta, D. Savoie, B. Fang, B. Venon, C. L. Garrido Alzar, R. Geiger, and A. Landragin, "Continuous Cold-Atom Inertial Sensor with 1 nrad/sec Rotation Stability", Physical Review Letters **116**, 1–5 (2016).

[41] S. Wu, E. Su, and M. Prentiss, "Demonstration of an Area-Enclosing Guided-Atom Interferometer for Rotation Sensing", Physical Review Letters **99**, 173201 (2007).

[42] J. A. Sauer, M. D. Barrett, and M. S. Chapman, "Storage ring for neutral atoms", Physical Review Letters **87**, 270401–270401–4 (2001).

[43] A. S. Arnold, C. S. Garvie, and E. Riis, "Large magnetic storage ring for Bose-Einstein condensates", Physical Review A **73**, 041606 (2006).

[44] I. Lesanovsky, T. Schumm, S. Hofferberth, L. M. Andersson, P. Krüger, and J. Schmiedmayer, "Adiabatic radio-frequency potentials for the coherent manipulation of matter waves", Physical Review A **73**, 033619 (2006).

[45] T. Fernholz, R. Gerritsma, P. Krüger, and R. J. Spreeuw, "Dynamically controlled toroidal and ring-shaped magnetic traps", Physical Review A - Atomic, Molecular, and Optical Physics **75**, 1–6 (2007).

[46] S. K. Schnelle, E. D. van Ooijen, M. J. Davis, N. R. Heckenberg, and H. Rubinsztein-Dunlop, "Versatile two-dimensional potentials for ultra-cold atoms", Optics Express **16**, 1405 (2008).

[47] K. Henderson, C. Ryu, C. MacCormick, and M. G. Boshier, "Experimental demonstration of painting arbitrary and dynamic potentials for Bose-Einstein condensates", New Journal of Physics **11**, 043030 (2009).

[48] T. A. Bell, J. A. P. Glidden, L. Humbert, M. W. J. Bromley, S. A. Haine, M. J. Davis, T. W. Neely, M. A. Baker, and H. Rubinsztein-Dunlop, "Bose–Einstein condensation in large time-averaged optical ring potentials", New Journal of Physics **18**, 035003 (2016).

[49] M. Pasienski and B. DeMarco, "A high-accuracy algorithm for designing arbitrary holographic atom traps", Optics Express **16**, 2176 (2008).

[50] G. D. Bruce, J. Mayoh, G. Smirne, L. Torralbo-Campo, and D. Cassettari, "A smooth, holographically generated ring trap for the investigation of superfluidity in ultracold atoms", Physica Scripta **T143**, 014008 (2011).

[51] I. Bloch, T. W. Hansch, and T. Essilinger, "Measurement of the spatial coherence of a trapped Bose gas at the phase transition", Nature **403**, 166–170 (2000).

[52] F. Harris, "On the use of windows for harmonic analysis with the discrete Fourier transform", Proceedings of the IEEE **66**, 51–83 (1978).

[53]M. O. Scully and J. P. Dowling, "Quantum-noise limits to matter-wave interferometry", Physical Review A **48**, 3186–3190 (1993).

[54]A. Lenef, T. D. Hammond, E. T. Smith, M. S. Chapman, R. A. Rubenstein, and D. E. Pritchard, "Rotation Sensing with an Atom Interferometer", Phys. Rev. Lett. **78**, 760–763 (1997).

[55]G. E. Marti, R. Olf, and D. M. Stamper-Kurn, "Collective excitation interferometry with a toroidal Bose-Einstein condensate", Physical Review A - Atomic, Molecular, and Optical Physics **91**, 13602 (2015).

[56]L. Amico, M. Boshier, G. Birkl, A. Minguzzi, C. Miniatura, L. .-. Kwek, D. Aghamalyan, V. Ahufinger, D. Anderson, N. Andrei, A. S. Arnold, M. Baker, T. A. Bell, T. Bland, J. P. Brantut, D. Cassettari, W. J. Chetcuti, F. Chevy, R. Citro, S. De Palo, R. Dumke, M. Edwards, R. Folman, J. Fortagh, S. A. Gardiner, B. M. Garraway, G. Gauthier, A. Günther, T. Haug, C. Hufnagel, M. Keil, W. von Klitzing, P. Ireland, M. Lebrat, W. Li, L. Longchambon, J. Mompart, O. Morsch, P. Naldesi, T. W. Neely, M. Olshanii, E. Orignac, S. Pandey, A. Pérez-Obiol, H. Perrin, L. Piroli, J. Polo, A. L. Pritchard, N. P. Proukakis, C. Rylands, H. Rubinsztein-Dunlop, F. Scazza, S. Stringari, F. Tosto, A. Trombettoni, N. Victorin, D. Wilkowski, K. Xhani, and A. Yakimenko, "State of the art and perspective on Atomtronics", arXiv:2008.04439v4 (2020).

[57]E. R. Moan, R. A. Horne, T. Arpornthip, Z. Luo, A. J. Fallon, S. J. Berl, and C. A. Sackett, "Quantum Rotation Sensing with Dual Sagnac Interferometers in an Atom-Optical Waveguide", Physical Review Letters **124**, 120403 (2020).

[58]K. J. Hughes, B. Deissler, J. H. T. Burke, and C. A. Sackett, "High-fidelity manipulation of a Bose-Einstein condensate using an optical standing wave", Physical Review A **76**, 035601 (2007).

[59]B. Fang, N. Mielec, D. Savoie, M. Altorio, A. Landragin, and R. Geiger, "Improving the phase response of an atom interferometer by means of temporal pulse shaping", New Journal of Physics **20**, 023020 (2018).

[60]J. Saywell, M. Carey, I. Kuprov, and T. Freegarde, "Biselective pulses for large-area atom interferometry", Physical Review A **101**, 063625 (2020).

[61]V. A. Henderson, P. F. Griffin, E. Riis, and A. S. Arnold, "Comparative simulations of Fresnel holography methods for atomic waveguides", New Journal of Physics **18**, 25007 (2016).

[62] V. A. Henderson, M. Y. H. Johnson, Y. B. Kale, P. F. Griffin, E. Riis, and A. S. Arnold, "Optical characterisation of micro-fabricated Fresnel zone plates for atomic waveguides", Optics Express **28**, 9072 (2020).

[63] B. I. Robertson, "High Contrast Measurements with a Bose-Einstein Condensate Atom Interferometer", PhD thesis (University of Strathclyde, 2016).

[64] A. R. Mackellar, "Single-Shot Holographic Readout of an Atom Interferometer", PhD thesis (University of Strathclyde, 2017).

[65] V. A. Henderson, "Exploring Fresnel Holography for Optically Guided Atom Interferometry with Bose-Einstein Condensates University of Strathclyde", PhD thesis (University of Strathclyde, 2018).

[66] A. Dinkelaker, "Smooth Inductively Coupled Ring Trap for Cold Atom Optics", PhD thesis (University of Strathclyde, 2013).

[67] G. D. Bruce, E. Haller, B. Peaudecerf, D. A. Cotta, M. Andia, S. Wu, M. Y. H. Johnson, B. W. Lovett, and S. Kuhr, "Sub-Doppler laser cooling of 40 K with Raman gray molasses on the D2 line", Journal of Physics B: Atomic, Molecular and Optical Physics **50**, 095002 (2017).

[68] W. Ketterle, D. S. Durfee, and D. M. Stamper-Kurn, "Making, probing and understanding Bose-Einstein condensates", in Proceedings of the international school of physics "Enrico Fermi", Vol. 140 (Apr. 1999), pp. 67–176.

[69] W. Ketterle, "Nobel lecture: When atoms behave as waves: Bose-Einstein condensation and the atom laser", Rev. Mod. Phys. **74**, 1131–1151 (2002).

[70] M. Fox, *Quantum optics : an introduction* (Oxford University Press, Oxford New York, 2006).

[71] C. J. Pethick and H. Smith, *Bose–Einstein Condensation in Dilute Gases* (Cambridge University Press, Cambridge, 2008).

[72] H. J. Metcalf and P. van der Straten, *Laser Cooling and Trapping*, Graduate Texts in Contemporary Physics (Springer New York, New York, NY, 1999).

[73] G. Grynberg, A. Aspect, and C. Fabre, *Introduction to Quantum Optics* (Cambridge University Press, 2010).

[74] C. J. Foot, *Atomic Physics (Oxford Master Series in Atomic, Optical and Laser Physics)* (Oxford University Press, 2005).

[75] Y. Castin, H. Wallis, and J. Dalibard, "Limit of Doppler cooling", Journal of the Optical Society of America B **6**, 2046 (1989).

[76] J. Dalibard and C. Cohen-Tannoudji, "Laser cooling below the Doppler limit by polarization gradients: simple theoretical models", J. Opt. Soc. Am. B **6**, 2023–2045 (1989).

[77] P. D. Lett, R. N. Watts, C. I. Westbrook, W. D. Phillips, P. L. Gould, and H. J. Metcalf, "Observation of Atoms Laser Cooled below the Doppler Limit", Phys. Rev. Lett. **61**, 169–172 (1988).

[78] D. Rio Fernandes, F. Sievers, N. Kretzschmar, S. Wu, C. Salomon, and F. Chevy, "Sub-Doppler laser cooling of fermionic 40 K atoms in three-dimensional gray optical molasses", EPL (Europhysics Letters) **100**, 63001 (2012).

[79] F. Sievers, N. Kretzschmar, D. R. Fernandes, D. Suchet, M. Rabinovic, S. Wu, C. V. Parker, L. Khaykovich, C. Salomon, and F. Chevy, "Simultaneous sub-Doppler laser cooling of fermionic Li 6 and K 40 on the D1 line: Theory and experiment", Physical Review A - Atomic, Molecular, and Optical Physics **91**, 1–11 (2015).

[80] J. P. Cotter, J. P. McGilligan, P. F. Griffin, I. M. Rabey, K. Docherty, E. Riis, A. S. Arnold, and E. A. Hinds, "Design and fabrication of diffractive atom chips for laser cooling and trapping", Applied Physics B: Lasers and Optics **122**, 1–6 (2016).

[81] J. P. McGilligan, P. F. Griffin, E. Riis, and A. S. Arnold, "Diffraction-grating characterization for cold-atom experiments", Journal of the Optical Society of America B **33**, 1271 (2016).

[82] E. Imhof, B. K. Stuhl, B. Kasch, B. Kroese, S. E. Olson, and M. B. Squires, "Two-dimensional grating magneto-optical trap", Physical Review A **96**, 033636 (2017).

[83] R. Elvin, G. W. Hoth, M. Wright, B. Lewis, J. P. McGilligan, A. S. Arnold, P. F. Griffin, and E. Riis, "Cold-atom clock based on a diffractive optic", Optics Express **27**, 38359 (2019).

[84] A. Ashkin, "Optical trapping and manipulation of neutral particles using lasers", in Proceedings of the national academy of sciences, Vol. 94, 10 (May 1997), pp. 4853–4860.

[85] R. Grimm, M. Weidemüller, and Y. B. Ovchinnikov, *Optical Dipole Traps for Neutral Atoms*, tech. rep. C (2000), pp. 95–170.

[86] W. Umrath, *Fundamentals of Vacuum Technology* (Leybold Vacuum, 2007).

[87] A. S. Arnold, "Adaptable-radius, time-orbiting magnetic ring trap for Bose-Einstein condensates", Journal of Physics B: Atomic, Molecular and Optical Physics **37**, L29–L33 (2004).

[88] E. Riis, D. S. Weiss, K. A. Moler, and S. Chu, "Atom funnel for the production of a slow, high-density atomic beam", Physical Review Letters **64**, 1658–1661 (1990).

[89] K. Dieckmann, R. J. C. Spreeuw, M. Weidemüller, and J. T. M. Walraven, "Two-dimensional magneto-optical trap as a source of slow atoms", Phys. Rev. A **58**, 3891–3895 (1998).

[90] M. A. Zentile, J. Keaveney, L. Weller, D. J. Whiting, C. S. Adams, and I. G. Hughes, "ElecSus: A program to calculate the electric susceptibility of an atomic ensemble", Computer Physics Communications **189**, 162–174 (2015).

[91] J. Keaveney, C. S. Adams, and I. G. Hughes, "ElecSus: Extension to arbitrary geometry magneto-optics", Computer Physics Communications **224**, 311–324 (2018).

[92] D. Phillips, *Notes on the Rb Maser and the CPT Clock*, (2004) `https://lweb.cfa.harvard.edu/%7B~%7Ddphil/work/rbmaser/masernotes.pdf`.

[93] A. N. Nesemeyanov, *Vapor Pressures of the Chemical Elements* (Elsevier, New York, 1963).

[94] A. Gallagher and E. L. Lewis, "Determination of the vapor pressure of rubidium by optical absorption", Journal of the Optical Society of America **63**, 864 (1973).

[95] J. Ramirez-Serrano, N. Yu, J. M. Kohel, J. R. Kellogg, and L. Maleki, "Multistage two-dimensional magneto-optical trap as a compact cold atom beam source", Optics Letters **31**, 682 (2006).

[96] T. B. Swanson, D. Asgeirsson, J. A. Behr, A. Gorelov, and D. Melconian, "Efficient transfer in a double magneto-optical trap system", Journal of the Optical Society of America B **15**, 2641 (1998).

[97] C. J. Myatt, N. R. Newbury, R. W. Ghrist, S. Loutzenhiser, and C. E. Wieman, "Multiply loaded magneto-optical trap", Optics Letters **21**, 290 (1996).

[98] S. P. Ram, S. R. Mishra, S. K. Tiwari, and S. C. Mehendale, "Note: Investigation of atom transfer using a red-detuned push beam in a double magneto-optical trap setup", Review of Scientific Instruments **82**, 126108 (2011).

[99] E. Dimova, O. Morizot, G. Stern, C. L. Garrido Alzar, A. Fioretti, V. Lorent, D. Comparat, H. Perrin, and P. Pillet, "Continuous transfer and laser guiding between two cold atom traps", Eur. Phys. J. D **42**, 299–308 (2007).

[100] H. Busche, S. W. Ball, and P. Huillery, "A high repetition rate experimental setup for quantum non-linear optics with cold Rydberg atoms", European Physical Journal: Special Topics **225**, 2839–2861 (2016).

[101] J. Catani, P. Maioli, L. De Sarlo, F. Minardi, and M. Inguscio, "Intense slow beams of bosonic potassium isotopes", Physical Review A - Atomic, Molecular, and Optical Physics **73**, 1–9 (2006).

[102] S. Chaudhuri, S. Roy, and C. S. Unnikrishnan, "Realization of an intense cold Rb atomic beam based on a two-dimensional magneto-optical trap: Experiments and comparison with simulations", Physical Review A - Atomic, Molecular, and Optical Physics **74**, 1–11 (2006).

[103] D. S. Weiss, E. Riis, Y. Shevy, P. J. Ungar, and S. Chu, "Optical molasses and multilevel atoms: experiment", Journal of the Optical Society of America B **6**, 2072 (1989).

[104] P. Arora, S. B. Purnapatra, A. Acharya, R. Kumar, and A. Sen Gupta, "Measurement of Temperature of Atomic Cloud Using Time-of-Flight Technique", MAPAN **27**, 31–39 (2012).

[105] E. L. Raab, M. Prentiss, A. Cable, S. Chu, and D. E. Pritchard, "Trapping of Neutral Sodium Atoms with Radiation Pressure", Physical Review Letters **59**, 2631–2634 (1987).

[106] W. D. Phillips, "Nobel Lecture: Laser cooling and trapping of neutral atoms", Reviews of Modern Physics **70**, 721–741 (1998).

[107] B. Gao, "Effects of Zeeman degeneracy on the steady-state properties of an atom interacting with a near-resonant laser field: Analytic results", Physical Review A **48**, 2443–2448 (1993).

[108] M. H. Anderson, J. R. Ensher, M. R. Matthews, C. E. Wieman, and E. A. Cornell, "Observation of Bose-Einstein Condensation in a Dilute Atomic Vapor", Science **269**, 198–201 (1995).

[109] K. B. Davis, M. .-. Mewes, M. R. Andrews, N. J. van Druten, D. S. Durfee, D. M. Kurn, and W. Ketterle, "Bose-Einstein Condensation in a Gas of Sodium Atoms", Physical Review Letters **75**, 3969–3973 (1995).

[110] E. A. Cornell and C. E. Wieman, "Nobel Lecture: Bose-Einstein condensation in a dilute gas, the first 70 years and some recent experiments", Rev. Mod. Phys. **74**, 875–893 (2002).

[111] M. Naraschewski and D. M. Stamper-Kurn, "Analytical description of a trapped semi-ideal Bose gas at finite temperature", Physical Review A **58**, 2423–2426 (1998).

[112] V. Bagnato, D. E. Pritchard, and D. Kleppner, "Bose-Einstein condensation in an external potential", Physical Review A **35**, 4354–4358 (1987).

[113] Y.-J. Lin, A. R. Perry, R. L. Compton, I. B. Spielman, and J. V. Porto, "Rapid production of Rb87 Bose-Einstein condensates in a combined magnetic and optical potential", Physical Review A **79**, 063631 (2009).

[114] D. M. Farkas, K. M. Hudek, E. A. Salim, S. R. Segal, M. B. Squires, and D. Z. Anderson, "A compact, transportable, microchip-based system for high repetition rate production of Bose–Einstein condensates", Applied Physics Letters **96**, 093102 (2010).

[115] J. Rudolph, W. Herr, C. Grzeschik, T. Sternke, A. Grote, M. Popp, D. Becker, H. Müntinga, H. Ahlers, A. Peters, C. Lämmerzahl, K. Sengstock, N. Gaaloul, W. Ertmer, and E. M. Rasel, "A high-flux BEC source for mobile atom interferometers", New Journal of Physics **17**, 065001 (2015).

[116] B. I. Robertson, A. R. Mackellar, J. Halket, A. Gribbon, J. D. Pritchard, A. S. Arnold, E. Riis, and P. F. Griffin, "Detection of applied and ambient forces with a matter-wave magnetic gradiometer", Physical Review A **96**, 1–7 (2017).

[117] K. Kataoka, "Estimation of coupling efficiency of optical fiber by far-field method", Optical Review **17**, 476–480 (2010).

[118] M. Kasevich and S. Chu, "Atomic interferometry using stimulated Raman transitions", Physical Review Letters **67**, 181–184 (1991).

[119] M. Kasevich, D. S. Weiss, E. Riis, K. Moler, S. Kasapi, and S. Chu, *Atomic velocity selection using stimulated Raman transitions*, tech. rep. 18 (1991), pp. 2297–2300.

[120] A. Gauguet, B. Canuel, T. Lévèque, W. Chaibi, and A. Landragin, "Characterization and limits of a cold-atom Sagnac interferometer", Physical Review A **80**, 063604 (2009).

[121] D. Savoie, M. Altorio, B. Fang, L. A. Sidorenkov, R. Geiger, and A. Landragin, "Interleaved atom interferometry for high-sensitivity inertial measurements", Science Advances **4**, eaau7948 (2018).

[122] A. Dunning, R. Gregory, J. Bateman, N. Cooper, M. Himsworth, J. A. Jones, and T. Freegarde, "Composite pulses for interferometry in a thermal cold atom cloud", Physical Review A **90**, 033608 (2014).

[123] J. C. Saywell, I. Kuprov, D. Goodwin, M. Carey, and T. Freegarde, "Optimal control of mirror pulses for cold-atom interferometry", Physical Review A **98**, 023625 (2018).

[124] J. Saywell, M. Carey, M. Belal, I. Kuprov, and T. Freegarde, "Optimal control of Raman pulse sequences for atom interferometry", Journal of Physics B: Atomic, Molecular and Optical Physics **53**, 085006 (2020).

[125] S. M. Dickerson, J. M. Hogan, A. Sugarbaker, D. M. S. Johnson, and M. A. Kasevich, "Multiaxis Inertial Sensing with Long-Time Point Source Atom Interferometry", Physical Review Letters **111**, 083001 (2013).

[126] P. J. Martin, P. L. Gould, B. G. Oldaker, A. H. Miklich, and D. E. Pritchard, "Diffraction of atoms moving through a standing light wave", Physical Review A **36**, 2495–2498 (1987).

[127] H. Müller, S.-W. Chiow, Q. Long, S. Herrmann, and S. Chu, "Atom Interferometry with up to 24-Photon-Momentum-Transfer Beam Splitters", Physical Review Letters **100**, 180405 (2008).

[128] H. Batelaan, "The Kapitza-Dirac effect", Contemporary Physics **41**, 369–381 (2000).

[129] P. L. Kapitza and P. A. M. Dirac, "The reflection of electrons from standing light waves", Mathematical Proceedings of the Cambridge Philosophical Society **29**, 297–300 (1933).

[130] B. Gadway, D. Pertot, R. Reimann, M. G. Cohen, and D. Schneble, "Analysis of Kapitza-Dirac diffraction patterns beyond the Raman-Nath regime", Optics Express **17**, 19173 (2009).

[131] Y. B. Ovchinnikov, J. H. Müller, M. R. Doery, E. J. D. Vredenbregt, K. Helmerson, S. L. Rolston, and W. D. Phillips, "Diffraction of a Released Bose-Einstein Condensate by a Pulsed Standing Light Wave", Physical Review Letters **83**, 284–287 (1999).

[132] H. Müller, S.-W. Chiow, and S. Chu, "Atom-wave diffraction between the Raman-Nath and the Bragg regime: Effective Rabi frequency, losses, and phase shifts", Physical Review A **77**, 023609 (2008).

[133] C. Adams, M. Sigel, and J. Mlynek, "Atom optics", Physics Reports **240**, 143–210 (1994).

[134] M. Kozuma, L. Deng, E. W. Hagley, J. Wen, R. Lutwak, K. Helmerson, S. L. Rolston, and W. D. Phillips, "Coherent Splitting of Bose-Einstein Condensed Atoms with Optically Induced Bragg Diffraction", Physical Review Letters **82**, 871–875 (1999).

[135] S. Gupta, A. E. Leanhardt, A. D. Cronin, and D. E. Pritchard, "Coherent manipulation of atoms with standing light waves", Comptes Rendus de l'Académie des Sciences - Series IV - Physics **2**, 479–495 (2001).

[136] S. Wu, Y.-J. Wang, Q. Diot, and M. Prentiss, "Splitting matter waves using an optimized standing-wave light-pulse sequence", Physical Review A **71**, 043602 (2005).

[137] K. J. Hughes, "Optical manipulation of atomic motion for a compact gravitational sensor with a Bose-Einstein condensate interferometer", PhD thesis (2008), p. 123.

[138] M. Kasevich and S. Chu, "Laser cooling below a photon recoil with three-level atoms", Physical Review Letters **69**, 1741–1744 (1992).

[139] N. Mielec, M. Altorio, R. Sapam, D. Horville, D. Holleville, L. A. Sidorenkov, A. Landragin, and R. Geiger, "Atom interferometry with top-hat laser beams", Applied Physics Letters **113**, 161108 (2018).

[140] V. Schkolnik, B. Leykauf, M. Hauth, C. Freier, and A. Peters, "The effect of wavefront aberrations in atom interferometry", Applied Physics B **120**, 311–316 (2015).

[141] Y. Zhai, C. H. Carson, V. A. Henderson, P. F. Griffin, E. Riis, and A. S. Arnold, "Talbot-enhanced, maximum-visibility imaging of condensate interference", Optica **5**, 80 (2018).

[142] V. Ménoret, P. Vermeulen, N. Le Moigne, S. Bonvalot, P. Bouyer, A. Landragin, and B. Desruelle, "Gravity measurements below 10-9 g with a transportable absolute quantum gravimeter", Scientific Reports **8**, 12300 (2018).

[143] V. Xu, M. Jaffe, C. D. Panda, S. L. Kristensen, L. W. Clark, and H. Müller, "Probing gravity by holding atoms for 20 seconds", Science **366**, 745–749 (2019).

[144] R. Geiger, A. Landragin, S. Merlet, and F. Pereira Dos Santos, "High-accuracy inertial measurements with cold-atom sensors", AVS Quantum Science **2**, 024702 (2020).

[145] A. O'Toole, F. E. Peña Arellano, A. V. Rodionov, M. Shaner, E. Sobacchi, V. Dergachev, R. DeSalvo, M. Asadoor, A. Bhawal, P. Gong, C. Kim, A. Lottarini, Y. Minenkov, and C. Murphy, "Design and initial characterization of a compact, ultra high vacuum compatible, low frequency, tilt accelerometer", Review of Scientific Instruments **85**, 075003 (2014).

[146] B. Canuel, L. Amand, A. Bertoldi, W. Chaibi, R. Geiger, J. Gillot, A. Landragin, M. Merzougui, I. Riou, S. Schmid, and P. Bouyer, "The matter-wave laser interferometer gravitation antenna (MIGA): New perspectives for fundamental physics and geosciences", E3S Web of Conferences **4**, edited by P. Febvre, E. Pozzo di Borgo, and K. Coulié-Castellani, 01004 (2014).

[147] H. Ahlers, H. Müntinga, A. Wenzlawski, M. Krutzik, G. Tackmann, S. Abend, N. Gaaloul, E. Giese, A. Roura, R. Kuhl, C. Lämmerzahl, A. Peters, P. Windpassinger, K. Sengstock, W. P. Schleich, W. Ertmer, and E. M. Rasel, "Double Bragg Interferometry", Physical Review Letters **116**, 173601 (2016).

[148] W.-J. Xu, M.-K. Zhou, M.-M. Zhao, K. Zhang, and Z.-K. Hu, "Quantum tiltmeter with atom interferometry", Physical Review A **96**, 063606 (2017).

[149] T. Lévèque, A. Gauguet, F. Michaud, F. Pereira Dos Santos, and A. Landragin, "Enhancing the Area of a Raman Atom Interferometer Using a Versatile Double-Diffraction Technique", Physical Review Letters **103**, 080405 (2009).

[150] S. J. M. Kuppens, K. L. Corwin, K. W. Miller, T. E. Chupp, and C. E. Wieman, "Loading an optical dipole trap", Physical Review A **62**, 013406 (2000).

[151] P. Cladé, E. De Mirandes, M. Cadoret, S. Guellati-Khélifa, C. Schwob, F. Nez, L. Julien, and F. Biraben, "Determination of the fine structure constant based on bloch oscillations of ultracold atoms in a vertical optical lattice", Physical Review Letters **96**, 2–5 (2006).

[152] L. Morel, Z. Yao, P. Cladé, and S. Guellati-Khélifa, "Determination of the fine-structure constant with an accuracy of 81 parts per trillion", Nature **588**, 61–65 (2020).

[153] D. A. Steck, *Rubidium87 D Line Data*, (2017) `http://steck.us/alkalidata/rubidium87numbers.1.6.pdf`.

[154] I. Dutta, D. Savoie, B. Fang, B. Venon, C. L. Garrido Alzar, R. Geiger, and A. Landragin, "Continuous Cold-Atom Inertial Sensor with 1nRad/s Rotation Stability", Physical Review Letters **116**, 183003 (2016).

[155] C. Antoine, "Rotating matter-wave beam splitters and consequences for atom gyrometers", Physical Review A **76**, 033609 (2007).

[156] F. Claeyssen, R. L. Letty, F. Barillot, and O. Sosnicki, "Amplified Piezoelectric Actuators: Static & Dynamic Applications", Ferroelectrics **351**, 3–14 (2007).

[157] D. S. Durfee, Y. K. Shaham, and M. A. Kasevich, "Long-Term Stability of an Area-Reversible Atom-Interferometer Sagnac Gyroscope", Physical Review Letters **97**, 240801 (2006).

[158] A. O. Jamison, J. N. Kutz, and S. Gupta, "Atomic interactions in precision interferometry using Bose-Einstein condensates", Physical Review A **84**, 043643 (2011).

[159] J. Halket, "In adv. preparation", PhD thesis (2021).

[160] A. Daffurn, R. F. Offer, and A. S. Arnold, "A simple, powerful diode laser system for atomic physics", arXiv:2104.06019v1 (2021).

[161] I. Bloch, J. Dalibard, and S. Nascimbène, "Quantum simulations with ultracold quantum gases", Nature Physics **8**, 267–276 (2012).

[162] S. Chu, J. E. Bjorkholm, A. Ashkin, and A. Cable, "Experimental Observation of Optically Trapped Atoms", Physical Review Letters **57**, 314–317 (1986).

[163] J. D. Miller, R. A. Cline, and D. J. Heinzen, "Far-off-resonance optical trapping of atoms", Physical Review A **47**, R4567–R4570 (1993).

[164] B. T. Seaman, M. Krämer, D. Z. Anderson, and M. J. Holland, "Atomtronics: Ultracold-atom analogs of electronic devices", Physical Review A **75**, 023615 (2007).

[165] L. Amico, G. Birkl, M. Boshier, and L.-C. Kwek, "Focus on atomtronics-enabled quantum technologies", New Journal of Physics **19**, 020201 (2017).

[166] N. Houston, E. Riis, and A. S. Arnold, "Reproducible dynamic dark ring lattices for ultracold atoms", Journal of Physics B: Atomic, Molecular and Optical Physics **41**, 211001 (2008).

[167]C. Ryu, P. W. Blackburn, A. A. Blinova, and M. G. Boshier, "Experimental Realization of Josephson Junctions for an Atom SQUID", Physical Review Letters **111**, 205301 (2013).

[168]C Ryu and M. G. Boshier, "Integrated coherent matter wave circuits", New Journal of Physics **17**, 092002 (2015).

[169]T. A. Bell, G. Gauthier, T. W. Neely, H. Rubinsztein-Dunlop, M. J. Davis, and M. A. Baker, "Phase and micromotion of Bose-Einstein condensates in a time-averaged ring trap", Physical Review A **98**, 013604 (2018).

[170]C. Ryu, K. C. Henderson, and M. G. Boshier, "Creation of matter wave Bessel beams and observation of quantized circulation in a Bose–Einstein condensate", New Journal of Physics **16**, 013046 (2014).

[171]B. M. Garraway and H. Perrin, "Recent developments in trapping and manipulation of atoms with adiabatic potentials", Journal of Physics B: Atomic, Molecular and Optical Physics **49**, 172001 (2016).

[172]Y. Colombe, E. Knyazchyan, O. Morizot, B. Mercier, V. Lorent, and H. Perrin, "Ultracold atoms confined in rf-induced two-dimensional trapping potentials", Europhysics Letters **67**, 593–599 (2004).

[173]T. Schumm, S. Hofferberth, L. M. Andersson, S. Wildermuth, S. Groth, I. Bar-Joseph, J. Schmiedmayer, and P. Krüger, "Matter-wave interferometry in a double well on an atom chip", Nature Physics **1**, 57–62 (2005).

[174]Y. Guo, R. Dubessy, M. d. G. de Herve, A. Kumar, T. Badr, A. Perrin, L. Longchambon, and H. Perrin, "Supersonic Rotation of a Superfluid: A Long-Lived Dynamical Ring", Physical Review Letters **124**, 025301 (2020).

[175]S. Pandey, H. Mas, G. Drougakis, P. Thekkeppatt, V. Bolpasi, G. Vasilakis, K. Poulios, and W. von Klitzing, "Hypersonic Bose–Einstein condensates in accelerator rings", Nature **570**, 205–209 (2019).

[176]N. Friedman, A. Kaplan, and N. Davidson, "Dark Optical Traps for Cold Atoms", in *Advances in atomic, molecular and optical physics*, Vol. 48, C (2002), pp. 99–151.

[177]B. K. Stuhl, B. C. Sawyer, D. Wang, and J. Ye, "Magneto-optical Trap for Polar Molecules", Physical Review Letters **101**, 243002 (2008).

[178]K. N. Jarvis, J. A. Devlin, T. E. Wall, B. E. Sauer, and M. R. Tarbutt, "Blue-Detuned Magneto-Optical Trap", Physical Review Letters **120**, 083201 (2018).

[179] A. S. Arnold, "Extending dark optical trapping geometries", Optics Letters **37**, 2505 (2012).

[180] H. J. Lee, C. S. Adams, M. Kasevich, and S. Chu, "Raman Cooling of Atoms in an Optical Dipole Trap", Physical Review Letters **76**, 2658–2661 (1996).

[181] K. Bongs, S. Burger, S. Dettmer, D. Hellweg, J. Arlt, W. Ertmer, and K. Sengstock, "Waveguide for Bose-Einstein condensates", Physical Review A **63**, 031602 (2001).

[182] M. Berry, M. Jeffrey, and J. Lunney, "Conical diffraction: observations and theory", Proceedings of the Royal Society A: Mathematical, Physical and Engineering Sciences **462**, 1629–1642 (2006).

[183] A. Turpin, V. Shvedov, C. Hnatovsky, Y. V. Loiko, J. Mompart, and W. Krolikowski, "Optical vault: A reconfigurable bottle beam based on conical refraction of light", Optics Express **21**, 26335 (2013).

[184] A. Turpin, Y. V. Loiko, T. K. Kalkandkiev, H. Tomizawa, and J. Mompart, "Super-Gaussian conical refraction beam", Optics Letters **39**, 4349 (2014).

[185] A. Turpin, J. Polo, Y. V. Loiko, J. Küber, F. Schmaltz, T. K. Kalkandjiev, V. Ahufinger, G. Birkl, and J. Mompart, "Blue-detuned optical ring trap for Bose-Einstein condensates based on conical refraction", Optics Express **23**, 1638 (2015).

[186] J. Arlt and M. J. Padgett, "Generation of a beam with a dark focus surrounded by regions of higher intensity: the optical bottle beam", Optics Letters **25**, 191 (2000).

[187] D. Yelin, B. E. Bouma, and G. J. Tearney, "Generating an adjustable three-dimensional dark focus", Optics Letters **29**, 661 (2004).

[188] L. Isenhower, W. Williams, A. Dally, and M. Saffman, "Atom trapping in an interferometrically generated bottle beam trap", Optics Letters **34**, 1159 (2009).

[189] P. Xu, X. He, J. Wang, and M. Zhan, "Trapping a single atom in a blue detuned optical bottle beam trap", Optics Letters **35**, 2164 (2010).

[190] J. L. Chaloupka, Y. Fisher, T. J. Kessler, and D. D. Meyerhofer, "Single-beam, ponderomotive-optical trap for free electrons and neutral atoms", Optics Letters **22**, 1021 (1997).

[191] R. Ozeri, L. Khaykovich, and N. Davidson, “Long spin relaxation times in a single-beam blue-detuned optical trap”, Physical Review A **59**, R1750–R1753 (1999).

[192] S. Franke-Arnold, J. Leach, M. J. Padgett, V. E. Lembessis, D. Ellinas, A. J. Wright, J. M. Girkin, P. Öhberg, and A. S. Arnold, “Optical ferris wheel for ultracold atoms”, Optics Express **15**, 8619 (2007).

[193] J. Lekner, “Polarization of tightly focused laser beams”, Journal of Optics A: Pure and Applied Optics **5**, 6–14 (2003).

[194] C. S. Adams and I. G. Hughes, *Optics f2f* (Oxford University Press, Dec. 2018).

[195] S. B. Viñas, Z. Jaroszewicz, A. Kolodziejczyk, and M. Sypek, “Zone plates with black focal spots”, Applied Optics **31**, 192 (1992).

[196] Dobrek, M. Gajda, M. Lewenstein, K. Sengstock, G. Birkl, and W. Ertmer, “Optical generation of vortices in trapped Bose-Einstein condensates”, Physical Review A - Atomic, Molecular, and Optical Physics **60**, R3381–R3384 (1999).

[197] J. Denschlag, “Generating Solitons by Phase Engineering of a Bose-Einstein Condensate”, Science **287**, 97–101 (2000).

[198] N. Savage, “Digital spatial light modulators”, Nature Photonics **3**, 170–172 (2009).

[199] L. J. Hornbeck, “Digital light processing and MEMS: an overview”, in Leos summer topical meeting (1996).

[200] W. Davis, “Optical MEMS for displays in portable systems”, in *Handbook of mems for wireless and mobile applications* (Elsevier, Aug. 2013), pp. 569–594.

[201] G. Gauthier, I. Lenton, N. McKay Parry, M. Baker, M. J. Davis, H. Rubinsztein-Dunlop, and T. W. Neely, “Direct imaging of a digital-micromirror device for configurable microscopic optical potentials”, Optica **3**, 1136 (2016).

[202] T. W. Clark, R. F. Offer, S. Franke-Arnold, A. S. Arnold, and N. Radwell, “Comparison of beam generation techniques using a phase only spatial light modulator”, Optics Express **24**, 6249 (2016).

[203] R. W. Gerchberg and W. O. Saxton, “A Practical Algorithm for the Determination of Phase from Image and Diffraction Plane Pictures”, Optik **35**, 237–246 (1972).

[204] T. Harte, G. D. Bruce, J. Keeling, and D. Cassettari, “Conjugate gradient minimisation approach to generating holographic traps for ultracold atoms”, Optics Express **22**, 26548 (2014).

[205] D. Bowman, T. L. Harte, V. Chardonnet, C. De Groot, S. J. Denny, G. Le Goc, M. Anderson, P. Ireland, D. Cassettari, and G. D. Bruce, “High-fidelity phase and amplitude control of phase-only computer generated holograms using conjugate gradient minimisation”, Optics Express **25**, 11692 (2017).

[206] A. L. Gaunt and Z. Hadzibabic, “Robust Digital Holography For Ultracold Atom Trapping”, Scientific Reports **2**, 721 (2012).

[207] A. Bernhard, *BBC travel: Places that changed the world*, 2019.

[208] J. Kirz, “Phase zone plates for x rays and the extreme uv”, Journal of the Optical Society of America **64**, 301 (1974).

[209] L. Kipp, M. Skibowski, R. L. Johnson, R. Berndt, R. Adelung, S. Harm, and R. Seemann, “Sharper images by focusing soft X-rays with photon sieves”, Nature **414**, 184–188 (2001).

[210] E. Schonbrun, C. Rinzler, and K. B. Crozier, “Microfabricated water immersion zone plate optical tweezer”, Applied Physics Letters **92**, 071112 (2008).

[211] G. Thalhammer, R. Steiger, S. Bernet, and M. Ritsch-Marte, “Optical macro-tweezers: trapping of highly motile micro-organisms”, Journal of Optics **13**, 044024 (2011).

[212] G. D. Bruce, M. Y. H. Johnson, E. Cormack, D. A. W. Richards, J. Mayoh, and D. Cassettari, “Feedback-enhanced algorithm for aberration correction of holographic atom traps”, Journal of Physics B: Atomic, Molecular and Optical Physics **48**, 115303 (2015).

[213] K. C. Wright, R. B. Blakestad, C. J. Lobb, W. D. Phillips, and G. K. Campbell, “Driving Phase Slips in a Superfluid Atom Circuit with a Rotating Weak Link”, Physical Review Letters **110**, 025302 (2013).

[214] T. A. Haase, D. H. White, D. J. Brown, I. Herrera, and M. D. Hoogerland, “A versatile apparatus for two-dimensional atomtronic quantum simulation”, Review of Scientific Instruments **88**, 113102 (2017).

[215] A. Kaplan, N. Friedman, and N. Davidson, “Optimized single-beam dark optical trap”, Journal of the Optical Society of America B **19**, 1233 (2002).

[216] P. Xu, X. He, J. Wang, and M. Zhan, “Trapping a single atom in a blue detuned optical bottle beam trap”, Optics Letters **35**, 2164 (2010).

[217] L. Amico, A. Osterloh, and F. Cataliotti, "Quantum Many Particle Systems in Ring-Shaped Optical Lattices", Physical Review Letters **95**, 063201 (2005).

[218] M.-X. Huo, W. Nie, D. A. W. Hutchinson, and L. C. Kwek, "A solenoidal synthetic field and the non-Abelian Aharonov-Bohm effects in neutral atoms", Scientific Reports **4**, 5992 (2015).

[219] L. Amico, D. Aghamalyan, F. Auksztol, H. Crepaz, R. Dumke, and L. C. Kwek, "Superfluid qubit systems with ring shaped optical lattices", Scientific Reports **4**, 4298 (2015).

[220] D. Aghamalyan, N. T. Nguyen, F. Auksztol, K. S. Gan, M. M. Valado, P. C. Condylis, L.-C. Kwek, R. Dumke, and L. Amico, "An atomtronic flux qubit: a ring lattice of Bose–Einstein condensates interrupted by three weak links", New Journal of Physics **18**, 075013 (2016).

[221] E. Di Gaetano, S. Watson, E. McBrearty, M. Sorel, and D. J. Paul, "Sub-megahertz linewidth 78024 nm distributed feedback laser for 87 Rb applications", Optics Letters **45**, 3529 (2020).

[222] O. S. Burrow, P. F. Osborn, E. Boughton, F. Mirando, D. P. Burt, P. F. Griffin, A. S. Arnold, and E. Riis, "Centilitre-scale vacuum chamber for compact ultracold quantum technologies", arXiv:2101.07851v1 (2021).

[223] J. P. McGilligan, P. F. Griffin, R. Elvin, S. J. Ingleby, E. Riis, and A. S. Arnold, "Grating chips for quantum technologies", Scientific Reports **7**, 384 (2017).

[224] Y.-J. Wang, D. Z. Anderson, V. M. Bright, E. A. Cornell, Q. Diot, T. Kishimoto, M. Prentiss, R. A. Saravanan, S. R. Segal, and S. Wu, "Atom Michelson Interferometer on a Chip Using a Bose-Einstein Condensate", Physical Review Letters **94**, 090405 (2005).

[225] T. Kinoshita, T. Wenger, and D. S. Weiss, "All-optical Bose-Einstein condensation using a compressible crossed dipole trap", Physical Review A **71**, 011602 (2005).

[226] M. Y. H. Johnson, V. Henderson, A. Pike, P. G. Griffin, E. Riis, and A. Arnold, "In preparation".